ELECTRON ORBITAL ANGULAR MOMENTUM: PREPARATION, APPLICATION AND MEASUREMENT

by

TYLER HARVEY

A DISSERTATION

Presented to the Department of Physics
and the Graduate School of the University of Oregon
in partial fulfillment of the requirements
for the degree of
Doctor of Philosophy

June 2017

DISSERTATION APPROVAL PAGE

Student: Tyler Harvey

Title: Electron Orbital Angular Momentum: Preparation, Application and Measurement

This dissertation has been accepted and approved in partial fulfillment of the requirements for the Doctor of Philosophy degree in the Department of Physics by:

Steven van Enk	Chair
Benjamin J. McMorrran	Advisor
Steve Gregory	Core Member
George Nazin	Institutional Representative

and

Scott L. Pratt	Dean of the Graduate School

Original approval signatures are on file with the University of Oregon Graduate School.

Degree awarded June 2017

DISSERTATION ABSTRACT

Tyler Harvey

Doctor of Philosophy

Department of Physics

June 2017

Title: Electron Orbital Angular Momentum: Preparation, Application and Measurement

The electron microscope is an ideal tool to prepare an electron into a specified quantum state, entangle that state with states in a specimen of interest, and measure the electron final state to indirectly gain information about the specimen. There currently exist excellent technologies to prepare both momentum eigenstates (transmission electron microscopy) and position eigenstates (scanning transmission electron microscopy) in a narrow band of energy eigenstates. Similarly, measurement of the momentum and position final states is straightforward with post-specimen lenses and pixelated detectors. Measurement of final energy eigenstates is possible with magnetic electron energy loss spectrometers. In 2010 and 2011, several groups independently showed that it was straightforward to prepare electrons into orbital angular momentum eigenstates. This disseratation represents my contributions to the toolset we have to control these eigenstates: preparation, application (interaction with specimen states), and measurement. My collaborators and I showed that phase diffraction gratings efficiently produce electron orbital angular momentum eigenstates; that control of orbital angular momentum can be used to probe

chirality and local magnetic fields; and that there are several routes toward efficient measurement.

This dissertation includes previously published and unpublished co-authored material.

CURRICULUM VITAE

NAME OF AUTHOR: Tyler Harvey

GRADUATE AND UNDERGRADUATE SCHOOLS ATTENDED:
University of Oregon, Eugene
Whitman College, Walla Walla

DEGREES AWARDED:
Doctor of Philosophy, Physics, 2017, University of Oregon
Bachelor of Arts, Physics-Environmental Studies, 2010, Whitman College

AREAS OF SPECIAL INTEREST:
Electron Orbital Angular Momentum
Phase-Contrast Scanning Transmission Electron Microscopy
Electron Energy Loss Spectroscopy

PROFESSIONAL EXPERIENCE:

Graduate Research Assistant, University of Oregon, 2013-2017

Graduate Teaching Fellow, Univeristy of Oregon, 2011-2013

GRANTS, AWARDS AND HONORS:

SCGSR Award, DOE Office of Science, 2017

Graduate Teaching Fellowship, UO Science Literacy Program, 2016

Travel Award, APS DAMOP Meeting, 2016

Presidential Scholar Award, Microscopy and Microanalysis Meeting, 2015

Travel Award, APS NW Section Meeting, 2014

Poster Award, Molecular Foundry Annual User Meeting, 2014

Travel Support Award, EIPBN Meeting, 2013

Weiser Senior Teaching Assistant Award, UO Department of Physics, 2013

Graduate Teaching Fellowship, UO Science Literacy Program, 2012

Qualifying Exam Prize, UO Department of Physics, 2012

PUBLICATIONS:

TR Harvey, V Grillo, BJ McMorran. *Phys. Rev. A* **95** 021801 (2017).

BJ McMorran, **TR Harvey**, MPJ Lavery. *New J. Phys.* **19** 023053 (2017).

JJ Chess, SA Montoya, **TR Harvey**, C Ophus, S Couture, V Lomakin, EE Fullerton, BJ McMorran. *Ultramicroscopy* **177** 78 (2017).

TR Harvey, JS Pierce, JJ Chess, BJ McMorran. arXiv:1507.01810.

C Ophus, J Ciston, J Pierce, **TR Harvey**, J Chess, BJ McMorran, C Czarnik, HH Rose, P Ercius. *Nat. Comm.* **7** 10719 (2016).

TR Harvey, JS Pierce, AK Agrawal, P Ercius, M Linck, BJ McMorran. *New J. Phys.* **16** 093039 (2014).

TABLE OF CONTENTS

LIST OF FIGURES

Figure Page

LIST OF TABLES

CHAPTER I

INTRODUCTION

In 1992, a group at Leiden [1] discovered that light beams could carry discrete quanta of orbital angular momentum (OAM). In the years that followed, a wide range of tools to manipulate and measure OAM were developed. These tools were quickly adopted in pursuit of a number of interesting applications of the OAM of light, including microscopy and astronomical imaging [2, 3, 4, 5], communication [6, 7], and manipulation of particles [8, 9, 10].

In 2010 and 2011, three groups independently demonstrated that electrons can similarly be placed in quantized OAM states [11, 12, 13]. In the last seven years, the emerging field of electron OAM has developed a basic toolset to manipulate electron OAM and the beginnings of some exciting applications. Many of these tools and applications have been borrowed from the literature on the OAM of light; a few involve properties specific to electrons with OAM.

The most useful tool borrowed from light optics is the ability to prepare electron OAM states with diffraction gratings [12, 13, 14, 15, 16]. Diffraction gratings remain one of the best ways to produce electron OAM states. However, two new methods to produce electron OAM states look distinctly different than their counterparts for light. Spiral phase plates for light can be made extremely transparent and machined with very good precision; however, even the most electron-transparent materials produce significant undesirable scattering at the thickness required for a maximum phase shift of 2π, and materials are difficult to machine precisely enough on the nanometer scale to produce a good spiral phase plate [11, 17]. Several groups have designed better spiral phase plates that utilize the interaction of electrons with magnetic [18, 19]

and electric [20, 21] fields. Diffraction gratings allow more detailed control of the electron wavefunction [14, 16, 22], but typically produce more than one beam and add some noise due to unwanted scattering processes in the grating material. Magnetic and electric spiral phase plates offer more efficient, lower-noise methods to produce electron OAM states, but are less versatile and are non-trivial to fabricate.

Now that there are multiple good methods to produce electron OAM states, we can begin to apply them to the study of materials and basic physical processes. There have been a wealth of proposals for uses for electron OAM states and few realizations so far [23, 24, 25, 26, 27, 28, 29, 30, 31]. One experiment has demonstrated rotation of nanoparticles on a substrate [32]. Two experiments have demonstrated sensitivity to the chirality of materials [33, 34]. Several experiments have shown that the additional magnetic dipole moment carried by an electron with OAM offers sensitivity to out-of-plane magnetic fields [35, 36, 37, 38]. Much effort has been dedicated to demonstrating magnetic dichroism with incident electron OAM states; no conclusive results have been published.

The slow progress towards applications is in part due to the lack of a crucial tool: the ability to cleanly post-select for electron OAM states. The ability to spatially isolate OAM states, such that the OAM can be quantitatively measured and each individual state can be further manipulated, would make many applications easier to realize. Three classes of OAM measurement tools have been developed so far: reference-wave interference methods [13] self-interferometric methods [39, 40, 41] and phase-flattening methods [42, 43]. Interferometric methods require coherence of the incident beam, and become increasingly less accurate as the number of incident OAM states increases [44]. Phase flattening with a grating is inefficient and not quantitative. None of these methods works particularly well to measure the mess of states that

results from interaction with a real material, and none can be used to post-select for a single OAM state. We therefore need better OAM measurement tools.

This dissertation is composed of three previously published papers and two manuscripts that are in progress. I have chosen to organize them in three chapters corresponding to the three steps necessary to employ an electron to probe a specimen: preparation of the electron in an orbital angular momentum state; interaction of the electron with the specimen; and measurement of the electron final state.

The following manuscripts are included in this work:

Chapter II. Preparation

Tyler R. Harvey, Jordan S. Pierce, Amit K. Agrawal, Peter Ercius, Martin Linck, and Benjamin J. Mcmorran. "Efficient diffractive phase optics for electrons." *New Journal of Physics* **16** 093039 (2014).

Electron diffraction gratings can be used to imprint well-defined phase structure onto an electron beam. For example, diffraction gratings have been used to prepare electron beams with unique phase dislocations, such as electron vortex beams, which hold promise for the development of new imaging and spectroscopy techniques for the study of materials. However, beam intensity loss associated with absorption, scattering, and diffraction by a binary transmission grating drastically reduces the current in the beam, and thus the possible detected signal strength it may generate. Here we describe electron-transparent *phase* gratings that efficiently diffract transmitted electrons. These phase gratings produce electron beams with the high current necessary to generate detectable signal upon interaction with a material. The phase grating design detailed here allows for fabrication of much more complex grating structures with extremely fine features. The diffracted beams produced by these gratings are widely separated and carry the designed phase structure with high fidelity.

In this work, we outline a fabrication method for high-efficiency electron diffraction gratings and present measurements of the performance of a set of simple prototypical gratings in a transmission electron microscope. We present a model for electron diffraction gratings that can be used to optimize the performance of diffractive electron optics. We also present several new holograms that utilize manipulation of the diffraction efficiency to produce new types of electron beams.

Tyler R. Harvey. "Transfer of Orbital Angular Momentum from Photons to Electrons." In preparation.

We explore the interactions of photons and electrons that involve an exchange of orbital angular momentum. We develop formalism to understand 'angular diffraction' of electrons from a superposition of light orbital angular momentum states.

Chapter III. Application

Tyler R. Harvey, Jordan S. Pierce, Jordan J. Chess and Benjamin J. McMorran. "Demonstration of electron helical dichroism as a local probe of chirality." arXiv:1507.01810.

We report observation of electron helical dichroism on a material with chiral structure. In analogy with circular dichroism, a common technique for molecular structural fingerprinting, we use a nanofabricated forked diffraction grating to prepare electron vortex beams with opposite orbital angular momenta incident upon metal nanoparticle clusters and post-select for a zero-orbital angular momentum final state. We observe a difference in the differential scattering probability for orbital

angular momentum transfer from vortices with opposite handedness incident on chiral aluminum nanoparticle clusters at 3.5 ± 0.8 eV. We suggest that the observed electron helical dichroism is due to excitation of surface plasmon vortices. Electron helical dichroism enables chirality measurement with unprecedented spatial resolution over a broad range of energies.

Tyler R. Harvey, Colin Ophus, Fehmi Yasin, Jordan J. Chess, Vincenzo Grillo and Benjamin J. Mcmorran. "Scanning transmission electron microscopic holography with forked diffraction gratings." In preparation.

We offer a model for analysis of electron holograms formed in the scanning transmission electron microscope. We first demonstrate a simple method to extract the specimen transfer function using a straight diffraction grating, and then show a similar method to measure longitudinal magnetic fields with a forked diffraction grating.

Chapter IV. Measurement

Tyler R. Harvey, Vincenzo Grillo and Benjamin J. McMorran. "Stern-Gerlach-like approach to electron orbital angular momentum measurement." *Physical Review A* **95** 021801 (2017).

Many methods now exist to prepare free electrons in orbital angular momentum states, and the predicted applications of these electron states as probes of materials and scattering processes are numerous. The development of electron orbital angular momentum measurement techniques has lagged behind. We show that coupling between electron orbital angular momentum and a spatially varying magnetic field produces an angular momentum-dependent focusing effect. We propose a design for an orbital angular momentum measurement device built on this principle. As the method of measurement is non-interferometric, the device works equally well for

mixed, superposed and pure final orbital angular momentum states. The energy and orbital angular momentum distributions of inelastically scattered electrons may be simultaneously measurable with this technique.

Benjamin J. McMorran, Tyler Harvey and Martin Lavery. "Efficient sorting of free electron orbital angular momentum." *New Journal of Physics* **19** 023053 (2017).

We propose a method for sorting electrons by orbital angular momentum (OAM). Several methods now exist to prepare electron wavefunctions in OAM states, but no technique has been developed for efficient, parallel measurement of pure and mixed electron OAM states. The proposed technique draws inspiration from the recent demonstration of the sorting of OAM through modal transformation. We show that the same transformation can be performed with electrostatic electron optical elements. Specifically, we show that a charged needle and an array of electrodes perform the transformation and phase correction necessary to sort orbital angular momentum states. This device may enable the analysis of the spatial mode distribution of inelastically scattered electrons.

This work was partially supported by the U.S. Department of Energy, Office of Science, Basic Energy Sciences, under Award DE-SC0010466 and by the National Science Foundation under grant No. 1607733.

CHAPTER II

PREPARATION

Notes on Manuscripts

Note on 'Efficient Diffractive Phase Optics for Electrons'

From Tyler R Harvey *et al.*, *New J. Phys.* **16** 093039 (2014).

Benjamin McMorran contributed the project idea. I and Jordan Pierce took the data for the paper. I, Benjamin McMorran and Jordan Pierce wrote the manuscript together. Jordan Pierce and I produced most of the figures. Peter Ercius contributed one. Amit Agrawal and Martin Linck helped Benjamin McMorran with the project idea and experimental design.

Note on 'Transfer of Orbital Angular Momentum from Photons to Electrons'

The second part of the chapter is an unpublished manuscript with no co-authors. The work emerged from a Quantum Optics course taught by Mike Raymer. I appreciated helpful discussions with Mike, Chris Jackson, Jordan Pierce and Galen Gledhill.

Efficient Diffractive Phase Optics for Electrons

Tyler Harvey[1], Jordan Pierce[1], Amit Agrawal[2,3], Peter Ercius[4], Martin Linck[5] and Benjamin J. McMorran[1]

[1] Department of Physics, University of Oregon, Eugene, Oregon

[2] Department of Electrical Engineering, Syracuse University, Syracuse, New York

[3] Center for Nanoscale Science and Technology, National Institute of Standards and Technology, Gaithersburg, Maryland

[4] National Center for Electron Microscopy, Lawrence Berkeley National Laboratory, Berkeley, California

[5] Corrected Electron Optical Systems GmbH, Englerstr. 28, D-69126 Heidelberg, Germany

25 September, 2014

Introduction to Efficient Diffractive Phase Optics

Scanning transmission electron microscopy (STEM) has recently offered a large number of critical insights into the structure and behavior of materials at the atomic scale [45, 46, 47]. As a result of several decades of advancements in electron optics, modern STEM instruments use precisely controlled electric and magnetic fields to prepare Ångstrom-sized 60 to 300 keV electron probe beams with currents on the order of nano-Amperes [48, 49]. The focused probes have an approximately Gaussian intensity distribution and a flat phase profile.

Following the development of atomic-scale STEM, there has been a surge of interest in using shaped probe beams with carefully designed phase structure and non-Gaussian intensity distributions. The interaction of such a shaped probe beam with a material can offer more information than is available through the use of a traditional probe beam [50, 51]. For example, electron vortex beams [52, 53, 54] may soon be employed to accomplish atomic resolution spin imaging [53, 55] with STEM. Holographic diffraction gratings [53, 54, 56, 57] and phase plates – both material [52]

and magnetic [58, 59] – have been successfully used to imprint the helical phase that defines a vortex beam.

Electron probe beams with well-defined phase structure can be produced via diffraction from a nanofabricated holographic diffraction grating placed in the probe-forming aperture of a STEM instrument [50] (see Figure 1). A second aperture lower in the column can be used to isolate one of the diffracted probes and use it to form an image. One can, in general, define the two-dimensional pattern $s(x, y)$ of a holographic diffraction grating by interference of a wavefunction of interest $\Psi(x, y)$ with a reference wave [60]:

$$s(x, y) = |\Psi(x, y) + \Psi_{\text{ref}}(x, y)|^2 \tag{2.1}$$

For example, to produce an electron vortex beam with $m\hbar$ orbital angular momentum in the first diffraction order of a linear grating periodic in the x-direction, one uses the two-dimensional pattern

$$s(x, y) = \left| \frac{1}{\sqrt{2}} \left(e^{im\phi} + e^{ikx} \right) \right|^2 = 1 + \cos(m\phi + kx) \tag{2.2}$$

A physical diffraction grating can imprint this pattern onto a transmitted complex wave, either through a modulation of amplitude or phase. In the case of a phase grating, the optical path length is varied according to the two-dimensional pattern $s(x, y)$, usually by varying the thickness of transparent grating material. We will return to the theory that guides the design of holographic diffraction gratings, and in particular optimal three-dimensional structure, in Section 2.5.

Other methods exist for imprinting a spiral phase dislocation onto electron beams; both material phase plates [52] and magnetic nanowire phase plates [58, 59]

add a spiral phase to an electron passed through them. However, production of pure spiral phase states with integer topological charge m is a significant challenge with these techniques. The topological charge imprinted depends on electron beam energy and is highly sensitive to fabrication errors and fringing fields, respectively. Diffractive electron optics offer the advantage that arbitrary phase structure can be imprinted on the electron beam with high fidelity and independent of beam energy. Furthermore, these devices can simultaneously produce multiple probe beams with complementary phase dislocations for dichroism techniques [50, 61].

There are two common challenges that must be addressed before diffractive electron optics may be widely adopted for use in electron microscopy. First, diffraction gratings must produce sufficiently intense diffracted beams so that information carried by a diffracted probe is measurable. Second, the multiple diffracted probe beams must be sufficiently separated in the specimen plane for use in the study of materials with varied shapes and sizes. For example, several recent diffractive structures used to create electron vortex beams [53, 56, 57] are composed of patterns of slits milled all the way through a relatively thick foil that is opaque to electrons. These structures operate by selectively subtracting beam current through high-angle scattering in the material and transmitting the rest through the slits. Thus, these structures behave as binary amplitude gratings, which can only place a maximum of 10.1 % of the incident electrons into the first diffraction order. This is particularly troublesome for STEM applications, in which beam current must be maximized in order to generate a detectable signal of interest over background noise. These electron amplitude gratings furthermore have small separation between diffracted beams; it is thus difficult to isolate signal generated by a particular beam. An amplitude grating must be sufficiently thick so as to be opaque to electrons. This restricts the smallest lateral

feature size that can be patterned, which consequently limits the diffraction angle. One recent demonstration of electron vortex production employed an amplitude diffraction grating which produced a beam separation of 3 μrad [53], or, equivalently, a real-space separation on the order of 5 nm in the specimen plane of a modern high-resolution STEM instrument.

To address these challenges, in our work developing electron vortex beams [54, 62] we have devoted considerable effort towards developing electron-transparent *phase* grating structures [63] that modulate the phase of the electron wave rather than the amplitude. Here we present a detailed study of these diffractive phase optics for electrons. We discuss the materials and nanofabrication method, performance measurements, and a model for these devices that incorporates the effects of both phase and amplitude modulation. Here we primarily discuss simple straight gratings periodic in one dimension, as shown in Figure 2, in order to elucidate the role of several basic grating structure parameters on diffraction efficiency. Optimization of the nanofabrication process for these simple gratings can then be applied to fabricate diffraction holograms which produce electron beams with non-trivial transverse wavefunctions $\Psi(x, y)$. In Figure 3, we demonstrate four gratings which produce diffracted beams with various different phase dislocations.

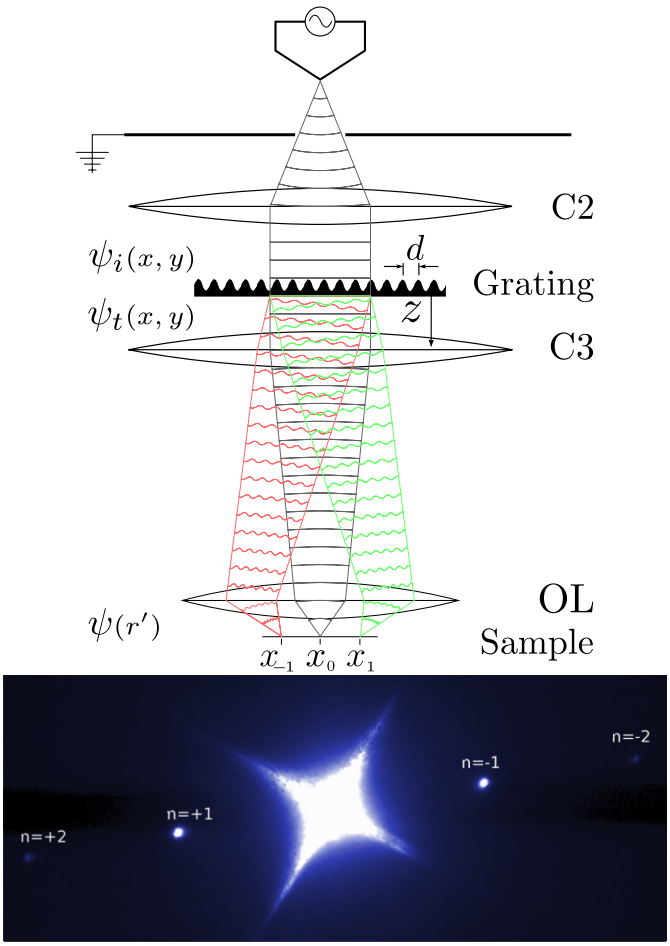

FIGURE 1. Probes prodced by a diffraction grating
(Top image) Layout of the diffraction process in a STEM showing the grating in the condenser aperture producing separated STEM probes at the specimen plane. When placed at the condenser aperture plane, the patterned circular area of the transparent grating has the same beam-defining properties as a regular circular condenser lens aperture. The diffracted beams can either be isolated using a second aperture, or the entire set of beams can be scanned across a local sample feature, providing multiple images of the object each containing unique information.
(Bottom image) TEM image of multiple diffracted STEM probes from a 50 μm-wide fork-dislocation grating at the specimen plane.

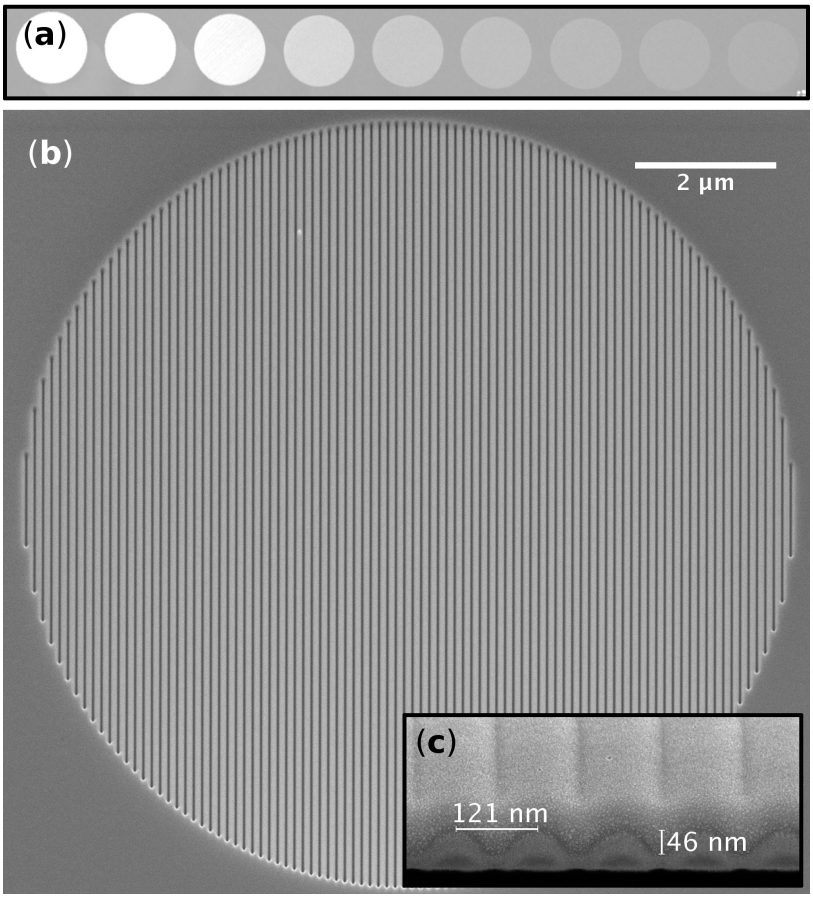

FIGURE 2. An example diffraction grating
Uniform phase gratings for electrons, which serve as a simple prototype to measure performance. In a TEM operated at 300 keV these gratings are nearly transparent – all of these images were recorded in an SEM at 5 keV in order to show contrast. (a) An example of a FIB patterning dose array in which the ion beam dwell time was varied. (b) A smaller, 10 μm diameter grating with 120 nm pitch. (c) A perspective view of a FIB cross section of the phase grating shows the corrugated surface. Approximately 50 nm of Pt was deposited on the corrugated surface only so that the cross section could be prepared and imaged – this Pt coating is not normally included in phase gratings meant for TEM.

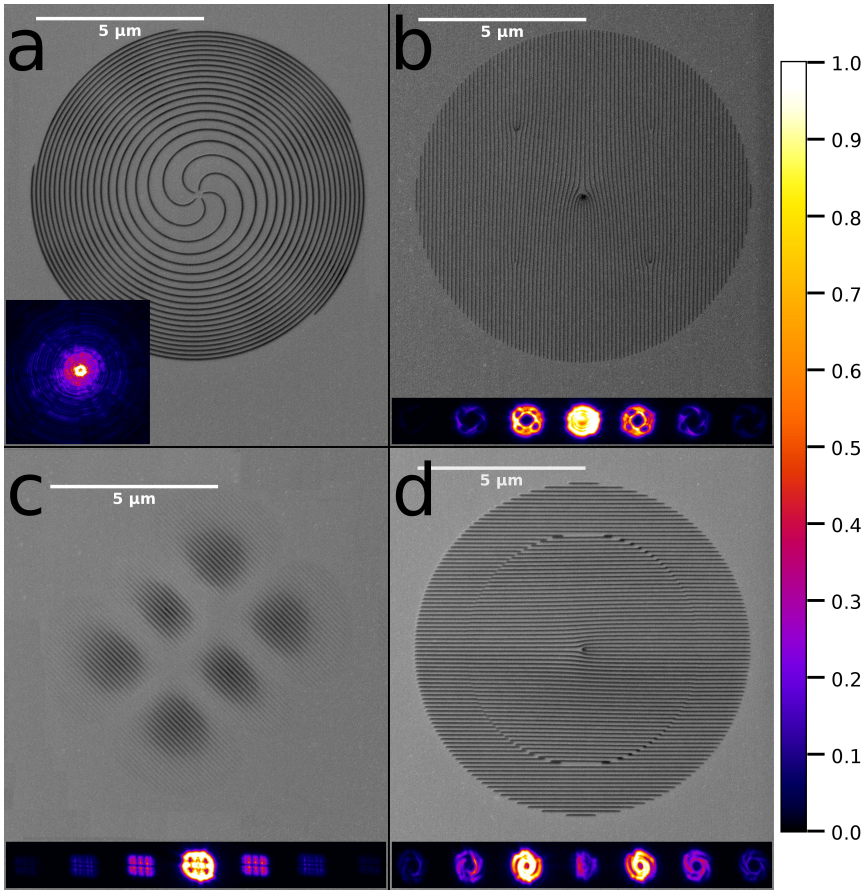

FIGURE 3. More example diffraction gratings

Examples of several phase grating designs that produce beams with non-trivial phase structure, together with the corresponding diffraction patterns. (a) A spiral phase dislocation grating produces beams with $L_z = 5n\hbar$ orbital angular momentum at a defocus $n\Delta f$, where n is the diffraction order number. The diffraction pattern is defocused so that the $n = +1$ order is in focus. (b) Multiple spatially separated fork dislocations produce diffracted beams with a net $\langle L_z \rangle = 0\hbar$ when in focus. (c) A Hermite Gaussian (1, 2) mode pattern. (d) An inner double fork dislocation grating and an outer zero-dislocation grating produces beams that are co-propagating superpositions of vortex beam and spherical wave. Note the suppressed 0-order intensity and enhanced ± 1-order intensities. In all of these examples, the beams have been defocused to reveal the details of their intensity and phase.

Electron Diffractive Phase Optics Design Goals

To be broadly useful for novel electron microscopy techniques, diffractive electron optics should efficiently diffract beam current into a desired diffraction order, and produce diffraction orders that are well-isolated from one another.

Diffraction Efficiency

In emerging STEM techniques using beams with engineered phase dislocations, it is important to maximize current in the probe beam. The efficiency of the diffraction hologram producing the beam thus becomes a primary concern. The diffraction hologram can be designed to generate just one electron probe beam, or simultaneously produce two or more probe beams with complementary phase dislocation properties. For example, a forked grating hologram with a symmetric thickness profile simultaneously produces pairs of electron probe beams with phase dislocations that are equal in magnitude but opposite in sign. It is expected that these two beams with opposite wavefront topologies can be used to provide dichroic image contrast [50, 61]. While in some applications it is desirable to produce only these two beams, in other instances it is desirable to also have a conventional electron probe beam with no phase dislocation to use for a reference signal. In all of these circumstances, the thickness profile of the hologram can be tailored to maximize the current in the electron beam and diffract it into one or more desired beams. It is also possible to form a blazed diffraction hologram that produces only one probe beam with a particular magnitude and/or sign of phase dislocation.

There are several important independent figures of merit for the diffraction efficiency of a holographic grating. Absolute diffraction efficiency $\eta_n^{(i)}$, transmitted diffraction efficiency $\eta_n^{(t)}$, and relative diffraction efficiency $\eta_n^{(n')}$ are each useful for

characterizing total detectable current, total detectable current as a fraction of the theoretical maximum for a given grating design, and detectable current relative to the noise produced by inelastic scattering in the grating, respectively.

The absolute diffraction efficiency is defined as

$$\eta_n^{(i)} \equiv \frac{I_n}{I_{\text{inc}}} \tag{2.3}$$

where I_n is the current in the n^{th} diffraction order, and I_{inc} is the total current incident on the diffraction grating. Potential electron microscopy applications require a maximal beam current in the $+1^{\text{st}}$ diffraction order, in which case $\eta_{+1}^{(i)}$ is the primary figure of merit. For a binary transmission grating, however, the maximum $\eta_{+1}^{(i)}$ is only 10.1 %. We demonstrate phase gratings that have twice this diffraction efficiency. When using blazed gratings, $\eta_{+1}^{(i)}$ can be made even larger at the expense of $\eta_{-1}^{(i)}$.

For material electron diffractive phase optics, some loss of electrons due to inelastic scattering is unavoidable. The total coherently transmitted beam current I_{trans}, equal to the sum of currents in all diffraction orders, is always less than the incident beam current, $I_{\text{trans}} = \sum_n I_n < I_{\text{inc}}$, and this is largely independent of the parameters of the particular groove shape. So to compare just the effects of groove shape and depth on diffraction efficiency independently from the effects of different thicknesses of material, it is then useful to define a *transmitted* diffraction efficiency describing the intensity in a particular diffraction order relative to the integrated intensity of all coherently transmitted electrons:

$$\eta_n^{(t)} \equiv \frac{I_n}{I_{\text{trans}}} \tag{2.4}$$

For STEM EELS with diffracted probes, quantitative analysis of an energy loss spectrum depends not just on the overall current in the beam, but also on the isolation of signal from a single diffracted probe. Adjacent diffraction orders may contribute to background signal. Thus, for such an application, the *relative* diffraction efficiency, defined as the ratio of intensity of the n^{th} order to the n'^{th} order, $\eta_n^{(n')}$, is a key figure of merit

$$\eta_n^{(n')} \equiv \frac{I_n}{I_{n'}}. \tag{2.5}$$

In most of the applications proposed to date for shape probe beams, the probe of interest is in the $n = \pm 1$ order, and the next most intense probe is the $n' = 0$ order. We will explicitly discuss the relative efficiency $\eta_1^{(0)}$ of gratings produced in this work.

Each of these figures of merit for efficiency represents a unique property of the STEM probes produced by a grating; absolute efficiency $\eta_n^{(i)}$ measures total detectable current in the n^{th} diffracted order, transmitted efficiency $\eta_n^{(t)}$ is a good measure of total detectable current as a function of theoretical maximum, and relative efficiency $\eta_n^{(n')}$ affects the signal-to-noise ratio for a measurement involving the n^{th} probe where noise from the n'^{th} is a concern. During review of this manuscript, Grillo et al. reported 25 % efficiency for the first-order diffracted probe of their phase diffraction gratings [64]; we note that this was a *transmitted* efficiency. Using our model developed in Section 2.5, we estimate that the 120 nm thick excess silicon nitride material supporting the grating structure incoherently scattered roughly 80 % of the incident intensity; after accounting for this intensity loss, we calculate that the *absolute* efficiency of this grating was approximately $\eta_1^{(i)} = 5$ %.

As we shall see in Section 2.5, the diffraction efficiency of a grating is a function of the shape and depth of grooves, the projected mean inner potential of the grating

material, and the electron beam energy. The theoretical maximum efficiency of a sinusoidal pure phase grating is 33.9 % [65]. For electron sinusoidal phase gratings made of silicon nitride (Si_3N_4), our model predicts that a physical groove depth of about 33 nm achieves this maximum. Utilizing high resolution FIB milling we have consistently fabricated gratings with $\eta_1^{(i)} > 20$ %.

Diffraction Order Separation

A diffractive optical element in a STEM application produces in general multiple probe beams, and there must be sufficient angular separation between them such that the signal they each generate can be isolated. To meet this design goal and provide large free space diffraction angles, electron diffractive optical elements should be fabricated with as small a feature size as possible without sacrificing pattern fidelity.

For electrons of de Broglie wavelength λ transmitted through a grating-like diffraction hologram with pitch d, where typically $\lambda \ll d$, the angular separation $\Delta\theta$ between diffracted beams is

$$\Delta\theta = \frac{\lambda}{d}. \tag{2.6}$$

In the specimen plane of a STEM, the real-space physical separation Δx between diffracted probe spot centers at the specimen plane is

$$\Delta x = \frac{z\Delta\theta}{M} = \frac{z\lambda}{Md} \tag{2.7}$$

where M is the magnification of the lower probe-forming STEM optics (*not* the image magnification) and z is the physical distance between the diffraction hologram and the specimen plane. Alternatively, in terms of the effective camera length L of the

lower probe-forming optics, the spot separation is

$$\Delta x = \frac{L\lambda}{d}. \tag{2.8}$$

In the TEAM 1 instrument at the National Center for Electron Microscopy, a grating with pitch $d = 83$ nm installed in the second condenser lens aperture produces diffracted 300 keV ($\lambda = 1.97$ pm) probe beams separated by $\Delta x = 43$ nm in the specimen plane (See Figure 1).

We note that it is easier to achieve larger angular separation between diffraction orders using diffractive phase optics. A distinct advantage of phase gratings over amplitude gratings is that they can be fabricated with much finer feature sizes, and so can produce much wider separation between diffracted beams. Free-standing amplitude-type gratings must be sufficiently robust to support the mass of the relatively thick, electron-opaque material; this condition limits the minimum lateral feature size of such a structure. Amplitude-blocking diffractive optics demonstrated to date [53, 56, 57] have a minimum periodic feature size on the order of 1 μm. On the other hand, phase gratings can be much thinner than amplitude gratings, and can be fabricated on an electron-transparent supportive membrane [63]. In [54] we demonstrated phase gratings with 75 nm period, and have since fabricated gratings with periodic feature sizes down to 20 nm [66].

Nanofabricated Diffractive Electron Optics

To achieve our stated design goals for efficient electron diffractive optics, we explored a diverse array of nanofabrication techniques for imprinting the phase grating onto electron-transparent materials. High-quality gratings may be produced with

high-resolution focused ion beam (FIB) milling, electron beam-induced deposition (EBID), and electron beam lithography (EBL); the choice of technique places some limitations on the structure of the gratings produced but is primarily a question of practical considerations. In this work, we consider prototypical electron diffractive optics produced by focused ion beam (FIB) milling, as FIB instruments are present in many TEM labs and can be used safely to produce an electron diffraction grating with minimal training. Some specific considerations for nanofabrication of gratings with FIB are detailed in the Appendix.

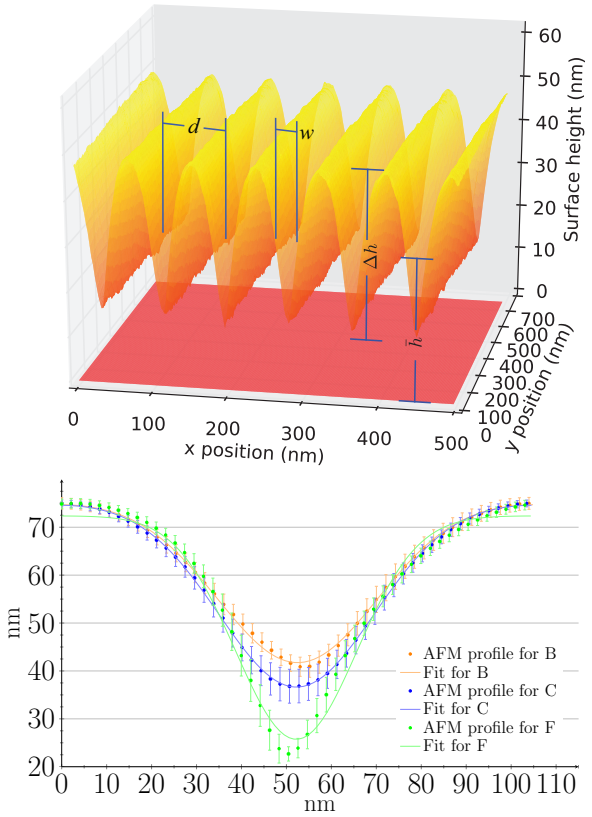

FIGURE 4. AFM profiles of diffraction gratings
(top) Two-dimensional AFM surface profile of an 80 nm pitch grating with a trench depth of 30.6 nm. The grating was milled by focused ion beam on a 50 nm thick silicon nitride membrane. The average membrane thickness $\bar{h}$, groove depth Δh, groove spacing, or pitch, d, and relative groove width w are labeled for reference. (bottom) One-dimensional AFM profiles of several 100 nm pitch gratings. The error bars represent variation in the measured groove depth over the area of the grating. The solid lines represent a best fit Gaussian-shaped groove used in our model of phase gratings.

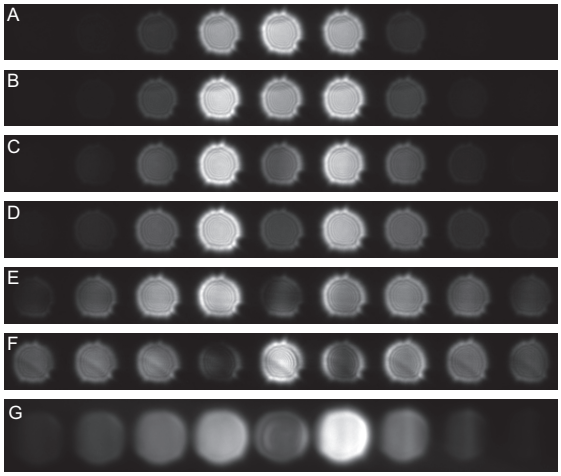

FIGURE 5. TEM images of diffracted beams
TEM diffraction images for gratings A - F. The diffracted beams are intentionally defocused in order to examine the uniform phase and amplitude in each beam. The grooves for each grating in the figure are successively deeper from top to bottom (associated AFM profiles are in Figure 4). (A-E) The 0^{th} order can be suppressed by deepening the grooves; here, $\eta_1^{(0)}$ can increase well beyond unity. (B) At this depth, the transmitted efficiencies of the -1, 0 and +1 orders, $\eta_{-1}^{(t)}$, $\eta_0^{(t)}$ and $\eta_{+1}^{(t)}$ are greater than 25 %. (E) With sufficiently deep trenches, we achieve $\eta_{\pm 1}^{(0)} > 5$ – that is, both positive and negative first-order beams are five times more intense than the zeroth order. (F) 0^{th} order intensity will increase again if the grooves are too deep. (G) Asymmetric grooves forming a blazed grating result in an asymmetric diffraction pattern, and a first-order diffracted beam with $\eta_1^{(t)} = 36.5$ %, and $\eta_1^{(i)} = 27.6$ %.

To compare the measured diffraction efficiencies of our holographic phase gratings to theoretical limits, we developed a model for mixed phase/amplitude gratings for electrons. The structure of the grating is a thin membrane with a modulated thickness $h(x, y)$. Figure 4 shows the thickness patterns of several fabricated grating measured with atomic force microscopy (AFM). The transmission function describing the effects of this structure on transmitted electron wavefunctions is

$$t(x,y) \quad = e^{-\alpha h(x,y)} \cdot e^{iCV_0 h(x,y)} = e^{i\tilde{k}h(x,y)} \tag{2.9}$$

where $\tilde{k} = CV_0 + i\alpha$ is the effective complex wavenumber of the electron within the material. The amplitude decay coefficient α describes the effects of inelastic and high angle scattering, and V_0 is the mean inner potential of the grating material. C depends only on the energy of the beam [67]. If such a grating is illuminated by an incident electron wave ψ_i, then the transmitted electron wavefunction immediately behind the grating is

$$\psi_t(x,y) \quad = \psi_i(x,y)e^{i\tilde{k}h(x,y)}. \tag{2.10}$$

The far field diffracted wave can be computed with the Fraunhofer approximation as shown in the Appendix (2.28).

In the case of simple linear phase gratings with uniform periodicity in only one direction, x, the modulated thickness of the material can be described as an array of grooves,

$$h(x,y) \quad = \bar{h} + \textstyle\sum_{n=-\infty}^{\infty} g(x-nd,y) - b \tag{2.11}$$

where $\bar{h}$ is the average thickness of the material grating, d is the pitch, or center-to-center groove spacing, and $g(x,y)$ describes the profile of the grooves. The offset b cancels any residual constant from the infinite sum. These parameters, as well as the groove depth Δh and width w, are shown in Figure 4. If the incoming wave ψ_i is a normally-incident plane wave (2.23), the diffracted wave amplitude from this linear grating may be written as

$$|\psi(\mathbf{r}')| = \frac{(2\pi)^2}{\lambda z'\sqrt{V}} e^{-\alpha\bar{h}} \sum_{n=-\infty}^{\infty} |c_n| \delta\left(\frac{kx'}{z'} - \frac{2\pi n}{d}\right) \delta\left(\frac{ky'}{z'}\right) \tag{2.12}$$

where λ is the de Broglie wavelength and V is a plane wave normalization factor. The relative amplitude of the nth diffraction order, c_n, depends upon the specific groove profile $g(x, y)$. A general form for computing c_n from any arbitrary periodic structure is described in detail in (2.38-2.40). The transmitted diffraction efficiency $\eta_n^{(t)}$ defined in (2.4) is calculated as

$$\eta_n^{(t)} = |c_n|^2. \tag{2.13}$$

Note that the absolute diffraction efficiency $\eta_n^{(i)}$, defined in (2.3) as a fraction of the *incident* beam, is less than (2.13) due to high-angle scattering

$$\eta_n^{(i)} = e^{-2\alpha\bar{h}}|c_n|^2. \tag{2.14}$$

where $\bar{h}$ is the average thickness of the grating over the back surface, as illustrated in Figure 4.

Cross sections (Figure 2) and AFM profiles (Figure 4) of the surface of our gratings indicate that individual grooves have a somewhat Gaussian shape. Earlier findings suggest that single-pixel-wide FIB-milled trenches have a remarkably Gaussian profile [68], so we model our gratings as a periodic sum of Gaussian grooves. The profile of an individual groove is

$$g(x) = \frac{A}{\sqrt{2\pi}\sigma} e^{-\frac{x^2}{2\sigma^2}} \tag{2.15}$$

with amplitude A, characteristic width σ; the profile of the entire grating is described by the periodic sum in (2.11) with this grating shape $g(x)$. The groove depth Δh and groove width w are related to the parameters A, σ, and b in (2.51-2.52) and (2.55).

Groove width is defined as the full width of the groove at half the maximum depth as a fraction of the pitch d.

With structure parameters describing the groove shape (depth Δh and width w) and material properties (absorption coefficient α and mean inner potential V_0), we can calculate the expected relative diffraction amplitudes c_n for a grating according to (2.38). We can thus reliably model the diffraction efficiency with a small number of measured parameters. While the diffracted wave could also be computed without any model numerically, the analytical calculation of c_n as a function of model parameters allows us to build an intuitive map of diffraction efficiency as a function of groove shape.

We parameterized the average groove shape of every grating in all of our fabrication arrays using the Gaussian groove model to determine the width w and depth Δh. In Figure 6, we used these average groove dimensions to categorize each grating (location in figure) and express the measured electron diffraction efficiency as a color value. These measured values compare well to the theoretical diffraction efficiency calculated using our model (background color).

The variations in efficiency between gratings with nearly identical trench depth and width, seen most clearly in Figure 7, are primarily due to gallium implantation from the FIB. We have observed up to 10 atomic % gallium concentrations in milled areas of our diffraction gratings with energy-dispersive X-ray spectroscopy (EDX) composition analysis. We do not account for any modification of the mean inner potential V_0 of the material in the mill process. We expect that the lower-than-expected first-order transmitted efficiency $\eta_{\pm 1}^{(t)}$ and higher-than-expected zeroth-order transmitted efficiency $\eta_0^{(t)}$ observed for gratings with a trench depth $\Delta h = 20 \pm 5$ nm are also due to gallium implantation. However, as gallium concentration is not easy

	Predicted	Measured
$\eta_1^{(i)} \equiv I_1/I_{\text{inc}}$	0.136 ± 0.005	0.17 ± 0.04
$\eta_1^{(t)} \equiv I_1/I_{\text{tran}}$	0.33 ± 0.01	0.34 ± 0.07
$\eta_1^{(0)} \equiv I_1/I_0$	5 ± 3	3.8 ± 0.8

TABLE 1. Comparison of predicted and measured efficiencies
Comparison of predicted and measured efficiencies for a grating with a width $w = 0.411 \pm 0.003$, trench depth $\Delta h = 35.7 \pm 0.5$ nm, and an average thickness $\bar{h} = 57.2 \pm 0.3$ nm.

to measure, and as this variation in efficiency is specific to only small range of gratings fabricated with FIB and does not affect our prediction for peak efficiency, we have chosen not to include extra parameters in our model to characterize this additional variation. We can use this simple model, which we have shown to predict efficiency with reasonable accuracy, to make prescriptions for the fabrication of highly efficient gratings.

The analysis summarized by Figure 6 provides a map that we used to explore a space of many interdependent parameters used for the nanofabrication process. We see in Figure 6 that any grating fabricated with a depth Δh between 27 nm and 40 nm and a full width at half max $w > 0.40$ will produce first-order diffracted beams with transmitted efficiency $\eta_1^{(t)} > 30$ %. The most efficient grating we fabricated indeed lies within this range. Table 1 offers a comparision of predicted and measured efficiencies for this grating. The predictions of the Gaussian groove model compare well with the diffraction efficiencies we measured from actual gratings.

This model provides a useful tool in the future design and fabrication of nanoscale electron phase gratings. For example, Figure 3 shows how the diffraction efficiency of the holograms can be manipulated to produce several different types of electron beams with engineered phase and intensity.

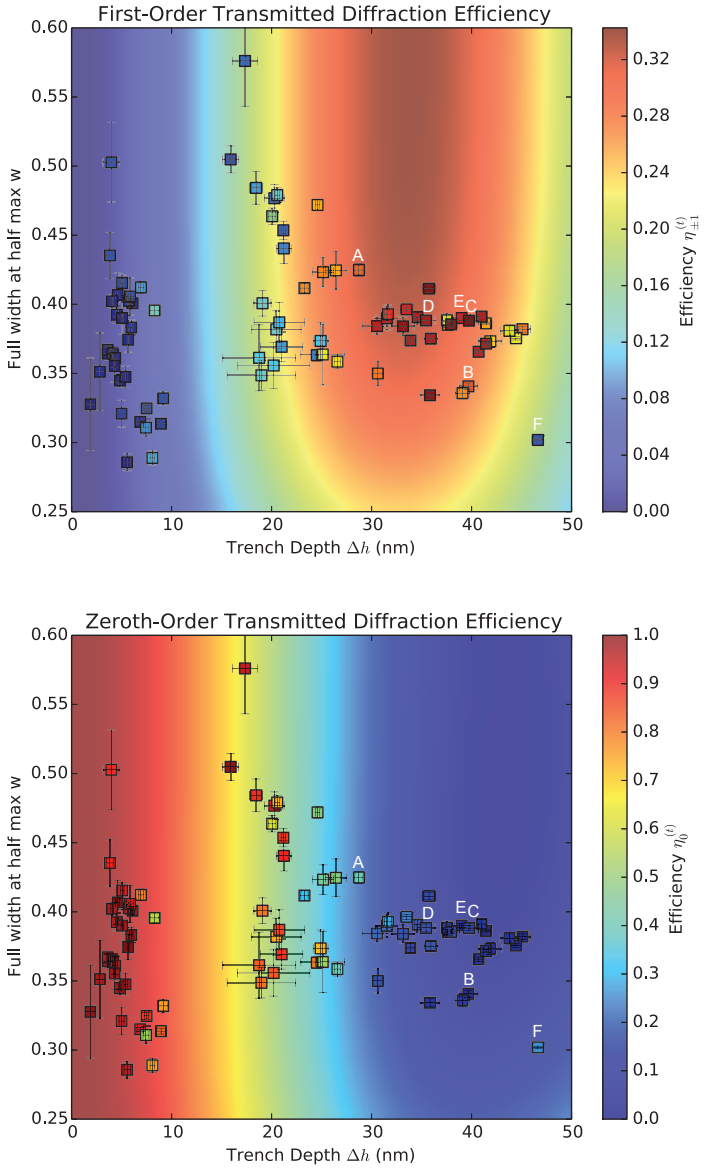

FIGURE 6. Parameter space map for optimizing diffraction efficiency Parameter space map showing the predicted (background color) and measured (squares) first-order (top) and zeroth-order (bottom) transmitted diffraction efficiencies for electron phase gratings as a function of the depth Δh and width w of grooves. Each square data point represents a phase grating fabricated in a silicon nitride membrane using a unique combination of FIB milling parameters. Each square's position describes the associated grating's groove depth (horizontal axis) and width (vertical axis) measured by AFM scans, and the square color is the diffraction efficiency of the respective order measured by TEM diffraction. The labeled data points correspond to the gratings that produced the diffraction patterns in Figure 5. The background color map represents a model that assumes symmetric grooves with uniform Gaussian-shaped depth cross sections and plane wave illumination. Both measured and predicted efficiencies in each plot share the same color scale denoted by the right-hand bar.

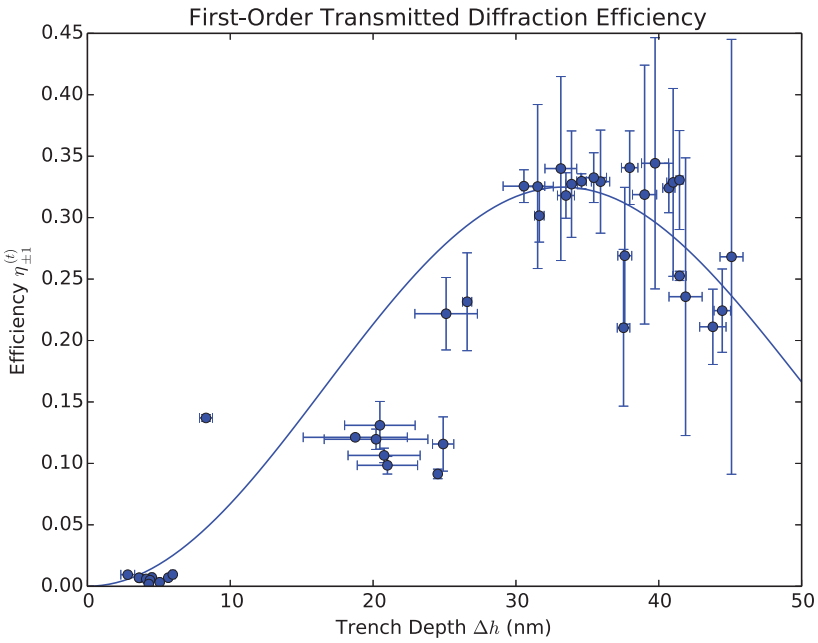

FIGURE 7. Measured efficiencies vs. trench depth
Measured transmitted diffraction efficiency of electron phase gratings as a function of groove depth Δh. The grooves of each grating plotted here all have the same width $w = 0.375 \pm 0.025$ relative to the center-to-center groove spacing. The solid line is a theoretical model that assumes Gaussian-shaped grooves, using only previously measured parameters.

Conclusion

Here we described our studying and optimizing the efficiency of electron diffractive phase optics for use in high resolution electron microscopy. We described a process for fabricating spatially coherent nanoscale material phase gratings, and characterized the performance of simple prototypical phase gratings in a TEM. We developed a theoretical model for optimizing the design of the gratings for particular uses. We demonstrated diffractive phase gratings with 80 nm periodic feature sizes covering areas 50 μm in diameter, and demonstrated grating periods down to 20 nm. We demonstrated phase gratings that produce equally intense -1^{st}, 0^{th}, and +1^{st} diffraction order beams with 25 % of the transmitted beam current each, gratings with suppressed 0^{th} order beams (intensities in the 1^{st} order up to 5 times greater) and blazed gratings that place 27 % of the incident beam current into the +1^{st} diffraction order. When installed in a TEM operated at 300 keV, these gratings are capable of providing multiple Ångstrom-scale electron probes with precisely manufactured phase dislocations. We demonstrate example nano fabricated holograms in which this diffraction efficiency is controlled in order to efficiently convert an incident electron beam into various engineered electron beams. This technology now makes possible shaped STEM probe techniques designed to produce more information about magnetically ordered, superconductor, semiconductor and biomolecular materials.

Diffraction Intensity Measurement

To determine the intensity of one diffraction order, we first measured noise in the image; we calculated the average background intensity I_b in a part of the micrograph where no signal intensity was present. We then subtracted this background intensity from the entire image, then set to zero all pixels which had an intensity less than this. Finally, to measure the intensity of the nth diffraction order, we centered a circular measurement region with a diameter equal to the spacing between orders over the nth diffraction spot. We then measured the total integrated intensity inside the circle.

We performed this measurement on an FEI 80-300 Titan TEM at 300 keV in Low-Angle Diffraction at a camera length of 104 m. We used a gun lens strength of 6 and a spot size of 8, a 150 um C2 aperture to limit the extent of the incoming wave, and an illuminated area of 104 μm. We then limited the outgoing wave with a 10 um objective aperture. The incident, transmitted and relative diffraction efficiencies of the beams formed by the grating are independent of aperture size and shape when absolute efficiency is measured as a function of incident intensity after the aperture [69]. We used a defocus of $-21.37 \cdot 10^{-6}$ so that the spots did not saturate the detector but were still well spaced.

Nanofabrication Considerations

To meet our stated design goals for efficient electron diffractive optics, we explored a large number of nanofabrication techniques for imprinting the phase grating onto electron-transparent materials. We have found a combination of grating material, charge alleviation layer, and patterning technique that provides good results, and discuss each of these separately in the following sections.

Grating Material

While there are many electron-transparent materials that can be used for this purpose, we choose to use silicon nitride membranes because of its mechanical robustness, thermal stability under electron illumination, and availability. We used silicon nitride membranes from several manufacturers, ranging in thicknesses from 15 nm to 100 nm thick, suspended over windows from 80 um across to 2 mm. Low-stress 30 nm to 100 nm-thick silicon nitride membranes purchased from SPI Supplies, Inc. performed best under long-term mill processing. We note that in general, a membrane thickness on the order of twice the final mill depth minimizes beam amplitude loss due to high-angle inelastic scattering while maintaining mechanical stability. In particular, we found that while 30 nm and 50 nm thick membranes block roughly 20 % and 50 % of the incident beam intensity, respectively, these standard thickness membranes routinely provide the greatest absolute diffraction efficiency for a 300 keV beam.

Nanofabrication Optimization

We have applied several nanofabrication techniques for patterning electron diffractive optics, including high-resolution focused ion beam (FIB) milling, electron beam-induced deposition (EBID), and electron beam lithography (EBL). We will concentrate our description here on the FIB-milling technique, since FIBs are present in many TEM labs and this maskless fabrication technique provides a quick method for making electron gratings. In particular, we used an FEI Helios NanoLab FIB to mill all gratings described in this work.

Modern FIB instruments offer many different parameters that can be used for milling the electron diffraction hologram pattern. The ion beam dwell time,

number of passes, milling scan direction, beam current, ion beam convergence angle, addressable pixel spacing, total ion dose, and pattern complexity all play a large and interconnected role in the quality of the final grating. An in-depth discussion and review of these effects is provided in [68]. We performed a systematic exploration of this complex parameter space in order to find the best combination for manufacturing efficient gratings for electrons.

We created a series of arrays of linear diffraction gratings in which we systematically varied total ion dose, dwell time, number of passes, patterning order, and beginning membrane thickness. These dose-arrays were placed in a field emission TEM operated at 300 keV. Low angle electron diffraction patterns were recorded under identical illumination conditions for each grating. Examples of these diffraction patterns are shown in Figure 5. The diffraction spots were defocused in order to examine the uniformity of the intensity of each beam – darker areas indicate an unwanted variation in groove width and depth across the grating area. We then measured the surface topology of each grating using an atomic force microscope (AFM) with a small diameter tip (Figure 4).

Many FIBs provide the ability to mill a pattern using a bitmap image or by direct programmable control of the beam path. We find that when using the bitmap patterning method, the pixel spacing of the magnified bitmap image should be an integer multiple of the minimum pixels spacing [68] of the FIB in order to avoid artifacts in the final structure due to nonuniform ion dosing. The scan direction of the beam should be chosen such that the slow scan axis is perpendicular to the grooves. While we have made decent gratings using both raster and serpentine scans during milling, we find best results when using a "vector scan" technique [68]; taking full programmable control of the beam path such that one complete groove can be

milled before moving on to the next element. For most purposes, we found that 10 passes, reversing the milling order each time, resulted in the highest quality gratings. However, when milling patterns covering large areas, settling and movement of the silicon nitride membrane reduces the quality of the pattern – in these cases it is best to reduce the number of passes. We find that ion beam currents below 10 pA produce the finest features, but larger currents on the order of 20 pA to 50 pA are necessary to complete a pattern larger than 20 μm diameter without major thermal drift over the course of the mill. For the pattern milled in Figure 2, the ion beam current was set to 10 pA and the number of passes was 80 with a pixel size of 3.3 nm.

Charge Alleviation Layer

The nitride gratings must be coated with a thin conductive layer to alleviate charging. We have experimented with using sputtered Ni, Ti, Cr, and Au, thermally evaporated C, and Pt from ion beam induced deposition (IBID). We find that 15 nm of amorphous carbon sufficiently minimizes charging and causes little absorption in the transmitted beam. However, when the carbon-coated grating is placed in an upper condenser lens of a TEM and exposed to a beam over the course of several weeks, the carbon can migrate into the grating trenches and decrease the absolute diffraction efficiency. A 5 nm to 10 nm layer of Au deposited on a 1 nm Cr adhesion layer leads to a slightly lower absolute diffraction efficiency $\eta_1^{(i)}$, due to absorption and scattering, but the diffraction efficiency of such gratings remain stable for weeks under exposed conditions in the beam path of the TEM. We find that Pt deposited by IBID contains significant amounts of carbon which can migrate under electron beam exposure, but the grating diffraction efficiency can be renewed by regular plasma cleaning. In all cases where a metal film is used, enhanced electron scattering decreases the absolute

diffraction efficiency $\eta_1^{(i)}$ and contributes to an unwanted background signal. However, a diffractive structure composed of silicon nitride grooves capped with a metal layer, produced either with FIB or IBID, modulates both the amplitude and phase of transmitted electrons. Such a mixed amplitude-phase grating can almost entirely suppress the 0^{th} (undiffracted) order (see Figure 5(d) and Figure 5(e)).

Hologram Uniformity, Spatial Coherence and Quality of Imprinted Phase

Spatial variations in the width and depth of grooves across the grating affect the amplitude uniformity inside each diffracted beam. These spatially dependent errors of FIB-milled gratings are primarily due to secondary dynamic processes such as redeposition, charging, heating, and membrane relaxation associated with the incidence of ions on the substrate surface. Large-area patterns with very fine pitch typically take several hours to mill, and changes in substrate tension or temperature can cause the substrate to drift at speeds on the order of nanometers per minute, which noticeably impacts the spatial coherence of the resulting structure. However, with an appropriate choice of a moderate ion beam current, a fewer number of patterning passes, and the application of a conductive layer to the membrane to prevent local charging, we have successfully produced spatially coherent gratings with 10^3 grooves over areas several tens of microns in diameter. We are in the process of developing a quantitative measure of spatial coherence.

Derivation of Diffraction Efficiency

The diffractive electron optical elements described in this work are thin membranes with a modulated thickness $h(x, y)$. As the both the de Broglie wavelength of electrons and the maximum thickness of an electron-transparent membrane in a

transmission electron microscope are necessarily small relative to the grating period, the thin grating condition under which wave interference due to propagation inside the grating material is negligible [65]

$$\lambda h << d^2 \tag{2.16}$$

is necessarily satisfied. Therefore, if an electron diffractive grating is illuminated by an incident electron wave ψ_i, then the transmitted electron wavefunction immediately behind the grating is

$$\psi_t(x,y) \quad = \psi_i(x,y)t(x,y). \tag{2.17}$$

where $t(x,y)$ is the transmission function describing the effects of a thin grating structure on transmitted electron wavefunctions. We note that if $\psi_i(x,y,z)$ is a normally plane wave, then $\psi_t(x,y) \propto t(x,y)$. We can express the transmission function as

$$t(x,y) \quad = e^{-\alpha h(x,y)} \cdot e^{iCV_0 h(x,y)} = e^{i\tilde{k}h(x,y)} \tag{2.18}$$

where $\tilde{k} = CV_0 + i\alpha$ is the effective complex wavenumber of the electron within the material. The amplitude decay coefficient α describes the effects of inelastic and high angle scattering, and V_0 is the mean inner potential of the grating material. C depends only on the energy of the beam [67]:

$$C = \frac{2\pi}{\lambda V_a} \frac{eV_a + m_e c^2}{eV_a + 2m_e c^2} \tag{2.19}$$

where V_a is the accelerating voltage for the electron.

We can describe any surface $h(x, y)$ periodic in the x-direction as a Fourier series with period d:

$$h(x,y) = \frac{a_0}{2} + \sum_{m=1}^{\infty} \left[a_m \cos(k_m x) + b_m \sin(k_m x)\right] \tag{2.20}$$

where $k_m = \frac{2\pi m}{d}$ and the coefficients are defined by

$$a_m = \tfrac{2}{d} \textstyle\int_{x_0}^{x_0+d} h(x,y)\cos(k_m x)\mathrm{d}x \tag{2.21}$$

$$b_m = \tfrac{2}{d} \textstyle\int_{x_0}^{x_0+d} h(x,y)\sin(k)mx)\mathrm{d}x \tag{2.22}$$

If an electron plane wave normalized in a finite-size box with volume V,

$$\psi_k = \frac{1}{\sqrt{V}} e^{ikz} \tag{2.23}$$

is normally incident on a grating with a surface described by $h(x, y)$, so that $\psi_i(x, y) = \psi_k$, we see from (2.17) that if we place the back of the grating at $z = 0$, as shown in Figure 1, the wavefunction $\psi_t(x, y)$ at $z = 0$ is proportional to the transmission function $t(x, y)$ of the grating,

$$\psi_t(x,y) = \frac{1}{\sqrt{V}} t(x,y) \tag{2.24}$$

Let's examine how this wave propagates.

Far from the grating, the outgoing electron wavefunction behind a grating can be described by the Fraunhofer formula [70],

$$\psi(\mathbf{r}') = \tfrac{1}{i\lambda z'} e^{ikz'} \textstyle\int \psi_t(x,y) e^{-i(xq_{x'}+yq_{y'})}\mathrm{d}x\ \mathrm{d}y \tag{2.25}$$

If we define the two-dimensional Fourier transform of a function $f(x, y)$ as

$$\tilde{f}(q_{x'}, q_{y'}) = \frac{1}{(2\pi)^2} \int f(x, y) e^{-i(xq_{x'} + yq_{y'})} \mathrm{d}x \ \mathrm{d}y \tag{2.26}$$

we can then rewrite $\psi(\mathbf{r}')$ simply in terms of the Fourier transformation of the transmission function

$$\psi(\mathbf{r}') = \tfrac{(2\pi)^2}{i\lambda z'} e^{ikz'} \tilde{\psi}_t(q_{x'}, q_{y'}) \tag{2.27}$$

$$\psi(\mathbf{r}') = \tfrac{(2\pi)^2}{i\lambda z' \sqrt{V}} e^{ikz'} \tilde{t}(q_{x'}, q_{y'}) \tag{2.28}$$

at coordinates (x', y', z'), where the spatial frequencies $q_{x'}$ and $q_{y'}$ are given by

$$q_{x'} = \frac{kx'}{z'} \qquad q_{y'} = \frac{ky'}{z'} \tag{2.29}$$

Equation (2.28) can be easily modified to take into account the shape of a finite-size aperture which limits the incident intensity; the diffraction efficiencies we will calculate, however, are unaffected by aperture shape and size [69].

Let's then rewrite $t(x, y)$ so that we can compute the Fourier transform easily. In terms of the Fourier series expansion of $h(x, y)$, we have

$$t(x, y) = \exp\left(i\tilde{k} \left[\tfrac{a_0}{2} + \textstyle\sum_{m=1}^{\infty} a_m \cos(k_m x) + b_m \sin(k_m x) \right] \right) \tag{2.30}$$

$$= e^{i\tilde{k} a_0/2} \textstyle\prod_{m=1}^{\infty} e^{i\tilde{k} a_m \cos(k_m x)} e^{i\tilde{k} b_m \sin(k_m x)} \tag{2.31}$$

Using the Jacobi-Anger expansion,

$$e^{iz\cos\theta} = \sum_{\ell=-\infty}^{\infty} i^{\ell} \mathrm{J}_{\ell}(z) e^{i\ell\theta} \qquad e^{iz\sin\theta} = \sum_{\ell=-\infty}^{\infty} \mathrm{J}_{\ell}(z) e^{i\ell\theta} \tag{2.32}$$

we can rewrite $t(x,y)$ simply in the plane wave basis.

$$t(x,y) \quad = e^{i\tilde{k}a_0/2}\prod_{m=1}^{\infty}\sum_{\ell=-\infty,\ell'=-\infty}^{\infty} i^{\ell}\mathrm{J}_{\ell}(\tilde{k}a_m)\mathrm{J}_{\ell'}(\tilde{k}b_m)e^{i(\ell+\ell')k_m x} \tag{2.33}$$

If we now change the variables in our double sum, defining $j = \ell + \ell'$ so that our plane wave term depends only on one index, j, we have

$$t(x,y) \quad = e^{i\tilde{k}a_0/2}\prod_{m=1}^{\infty}\sum_{j=-\infty}^{\infty}\sum_{\ell=-\infty}^{\infty} i^{\ell}\mathrm{J}_{\ell}(\tilde{k}a_m)\mathrm{J}_{j-\ell}(\tilde{k}b_m)e^{ijm\frac{2\pi x}{d}} \tag{2.34}$$

$$t(x,y) \qquad\qquad = e^{i\tilde{k}a_0/2}\prod_{m=1}^{\infty}\sum_{j=-\infty}^{\infty}\gamma_j(\tilde{k},a_m,b_m)e^{ijm\frac{2\pi x}{d}} \tag{2.35}$$

where we've defined a coefficient

$$\gamma_j(\tilde{k},a_m,b_m) \quad = \sum_{\ell=-\infty}^{\infty} i^{\ell}\mathrm{J}_{\ell}(\tilde{k}a_m)\mathrm{J}_{j-\ell}(\tilde{k}b_m) \tag{2.36}$$

We now have $t(x,y)$ written in terms of plane waves, but not as a linear superposition of plane waves. We can write the transmission function more simply if we perform the product. As the product of two plane waves with wave vectors $\mathbf{k_1}$ and $\mathbf{k_2}$ is another plane wave whose wave vector is the sum of the first two, we can rewrite a product of a sum of plane waves as a sum of plane waves whose coefficients are products over all terms whose total wave vector is constant. If we first define the vectors

$$\mathbf{M} \equiv \begin{pmatrix} 1 \\ 2 \\ \vdots \\ m \\ \vdots \end{pmatrix}, \qquad \mathbf{J} \equiv \begin{pmatrix} j_1 \\ j_2 \\ \vdots \\ j_m \\ \vdots \end{pmatrix} \tag{2.37}$$

$$t(x,y) \quad = e^{i\tilde{k}a_0/2} \sum_{n=-\infty}^{\infty} c_n e^{ik_n x} \tag{2.38}$$

$$c_n \quad = \sum_{s_n} \prod_{m=1}^{\infty} \gamma_{j_m}(\tilde{k}, a_m, b_m) \tag{2.39}$$

$$s_n \quad = \{\mathbf{J} : \mathbf{J} \cdot \mathbf{M} = n\} \tag{2.40}$$

The calculation of c_n can be considered as a discrete path integral in momentum j and a time m to a final position

$$q_f = \sum_{m=1}^{\infty} j_m m = n$$

Each set s_n describes one path which terminates at q_f; c_n is calculated as the sum of products of the coefficient $\gamma_{j_m,m}$ over all such paths.

We see that only those paths which include a finite number of steps at non-zero j_m or rapidly oscillate in j as m approaches infinity can possibly terminate at finite q_f. Fortunately, the contribution of oscillatory paths to the integral is negligible, as, for any physically realistic grating surface $h(x,y)$, $a_m, b_m << 1$ and thus $\gamma_{j_m,m} < 1$ for $m >> 1$ and $|j_m| > 0$. Thus, we can approximate c_n by choosing a cutoff m_c based on parameters of the model $h(x,y)$ for the product.

Now that we have written $t(x,y)$ in the plane wave basis, we can quickly calculate the diffracted wavefunction far behind the grating. Plugging $t(x,y)$ from (2.38) into our calculation of the diffracted wavefunction, (2.28), we have

$$\psi(\mathbf{r'}) \quad = \tfrac{1}{i\lambda z'\sqrt{V}} e^{ikz'} \int e^{i\tilde{k}a_0/2} \sum_{n=-\infty}^{\infty} c_n e^{ik_n x} e^{-i(xq_{x'}+yq_{y'})} \mathrm{d}x \; \mathrm{d}y \tag{2.41}$$

$$\psi(\mathbf{r'}) \quad = \tfrac{(2\pi)^2}{i\lambda z'\sqrt{V}} e^{i(kz'+\tilde{k}a_0/2)} \sum_{n=-\infty}^{\infty} c_n \delta\left(q_{x'} - k_n\right) \delta\left(q_{y'}\right) \tag{2.42}$$

at coordinates (x', y', z'), where the spatial frequencies $q_{x'}$ and $q_{y'}$ are given by

$$q_{x'} = \frac{kx'}{z'} \qquad q_{y'} = \frac{ky'}{z'} \tag{2.43}$$

The amplitude of $\psi(\mathbf{r}')$ in (2.42) produces (2.12):

$$|\psi(\mathbf{r}')| = \frac{(2\pi)^2}{\lambda z' \sqrt{V}} e^{-\alpha \bar{h}} \sum_{n=-\infty}^{\infty} |c_n| \delta\left(\frac{kx'}{z'} - \frac{2\pi n}{d}\right) \delta\left(\frac{ky'}{z'}\right) \tag{2.44}$$

As noted in (2.11) and (2.15), we model our nanofabricated gratings as an array of Gaussian-shaped trenches. In general, for a grating with pitch d and characteristic width σ, the surface thickness $h(x, y)$ of a FIB-milled grating can be described as the periodic sum of Gaussians,

$$h(x,y) \;\; = \bar{h} + \textstyle\sum_{n=-\infty}^{\infty} \left(\frac{A}{\sqrt{2\pi}\sigma} e^{-\frac{(x/d-n)^2}{2\sigma^2}} \right) - b \tag{2.45}$$

where $\bar{h}$ is the average grating height. The normalization A and offset b depend only on trench depth Δh and characteristic width σ. The Fourier coefficients of this model for $h(x, y)$ are

$$a_0 \;\; = \bar{h} + A - b \tag{2.46}$$

$$a_m \;\; = 2Ae^{-\frac{1}{2}(2\pi\sigma m)^2} \tag{2.47}$$

Therefore, written as a Fourier series, the height profile is

$$h(x,y) \;\; = A\left(1 + 2\textstyle\sum_{m=1}^{\infty} e^{-\frac{1}{2}(2\pi\sigma m)^2} \cos\left(k_m x\right)\right) + \bar{h} - b \tag{2.48}$$

where $k_m = 2\pi m/d$ as usual.

We note that as the coefficients a_m in our model are Gaussian in m, they fall off quickly and the diffraction from such a model can be calculated with good precision by cutting off c_n at $m_c = \frac{\beta}{\sigma}$, where β is an $O(1)$ number.

In order to quickly numerically compute $h(x, y)$, we note that the Fourier series can be written in terms of the third Jacobi Theta function, ϑ_3 [71]. This function is defined as

$$\vartheta_3(z, \tau) = 1 + 2\sum_{m=1}^{\infty} \left(e^{i\pi\tau}\right)^{m^2} \cos(2\pi m z) \tag{2.49}$$

Thus, we see that we can rewrite $h(x, y)$ as

$$h(x, y) \quad = A\vartheta_3\left(\tfrac{x}{d}, 2\pi i\sigma^2\right) + \bar{h} - b \tag{2.50}$$

Now, we can easily set the normalization and offset A and b in terms of Δh and $\bar{h}$. We choose Δh to be positive always by convention; A and b may change sign depending on groove shape. Profiles with narrow trenches have $A < 0$; FIB-milled gratings have a narrow-trench profile. Profiles with wide trenches, or, equivalently, narrow peaks have $A > 0$; deposited structures on a flat substrate have a narrow-peak profile. Let's define A and b for the case that $A < 0$.

$$A \quad = -\tfrac{\Delta h}{\vartheta_l - \vartheta_r} \tag{2.51}$$

$$b \qquad = A \tag{2.52}$$

where we've used the shorthand

$$\vartheta_l \quad = \vartheta_3(0, 2\pi i\sigma^2) \tag{2.53}$$

$$\vartheta_r \quad = \vartheta_3\left(\tfrac{1}{2}, 2\pi i\sigma^2\right) \tag{2.54}$$

As the scaled full-width at half-maximum of a groove w is more intuitively meaningful, we use w in the main paper. In terms of the characteristic width σ, we see that

$$w \approx 2\sqrt{2\ln 2}\sigma \tag{2.55}$$

This approximately linear relationship breaks down as w approaches 0.5; at this point, the surface is only better-approximated as a single sinusoid with $w = 0.5$ as the characterstic width σ increases. To represent the very wide trenches of a low-density line array produced by electron beam lithography or ion beam induced-deposition, we need only to flip the physical interpretation of the model: we actually want very narrow peaks, so we may flip the sign of Δh and fit the peaks with a small value of σ.

If we furthermore want to calculate $\bar{h}$ from a known maximum grating thickness h_{max}, trench depth Δh and characteristic width σ, we see that

$$\bar{h} = h_{max} - \Delta h \frac{1 - \vartheta_r}{\vartheta_l - \vartheta_r} \tag{2.56}$$

To calculate diffraction coefficicents c_n in this model, we choose a cutoff

$$m_c = \frac{0.5}{\sigma} \tag{2.57}$$

With this cutoff, we can calculate c_n to 10^{-5} precision for any physically reasonable width or height.

Hologram Pattern Design

We can now speak more clearly about how to physically implement a particular thickness modulation $h(x, y)$ to produce a desired diffracted wavefunction.

Let's show that we can produce a wavefront with an azimuthal phase which has been encoded in $h(x, y)$ by interference with a reference plane wave. First, let's define the grating thickness $h(x, y)$ in terms of the peak-to-trench height Δh and the minimum thickness h_0:

$$h(x,y) = \Delta h \left| \frac{1}{2}\left(e^{im\phi} + e^{ik_d x}\right)\right|^2 + h_0 \tag{2.58}$$

$$h(x,y) = \Delta h \frac{1}{2}\left(1 + \cos(m\phi + k_d x)\right) + h_0 \tag{2.59}$$

We can now calculate the transmission function $t(x, y)$ of the grating and therefore the final diffracted wavefunction $\psi(\mathbf{r}')$. If we plug $h(x, y)$ into (2.18), we see

$$t(x,y) = e^{i\tilde{k}(\Delta h \frac{1}{2}(1+\cos(m\phi+k_d x))+h_0)} \tag{2.60}$$

$$t(x,y) = e^{i\tilde{k}(\Delta h/2+h_0)} e^{i\tilde{k}(\Delta h/2\cos(m\phi+k_d x))} \tag{2.61}$$

Let's calculate the Fourier transformation of $t(x, y)$ so that we can use it in (2.28).

$$\tilde{t}(q_{x'}, q_{y'}) = \frac{1}{(2\pi)^2}\int t(x,y) e^{-i(xq_{x'}+yq_{y'})}\mathrm{d}x\ \mathrm{d}y \tag{2.62}$$

$$\tilde{t}(q_{x'}, q_{y'}) = \frac{1}{(2\pi)^2}\int e^{i\tilde{k}(\Delta h/2+h_0)} e^{i\tilde{k}(\Delta h/2\cos(m\phi+k_d x))} e^{-i(xq_{x'}+yq_{y'})}\mathrm{d}x\ \mathrm{d}y \tag{2.63}$$

$$\tilde{t}(q_{x'}, q_{y'}) = e^{i\tilde{k}(\Delta h/2+h_0)}\frac{1}{(2\pi)^2}\int e^{i\tilde{k}(\Delta h/2\cos(m\phi+k_d x))} e^{-i(xq_{x'}+yq_{y'})}\mathrm{d}x\ \mathrm{d}y \tag{2.64}$$

$$\tilde{t}(q_{x'}, q_{y'}) = Ae^{i\gamma}\frac{1}{(2\pi)^2}\int e^{i\tilde{k}(\Delta h/2\cos(m\phi+k_d x))} e^{-i(xq_{x'}+yq_{y'})}\mathrm{d}x\ \mathrm{d}y \tag{2.65}$$

For simplicity, we've called the overall global phase and amplitude term $Ae^{i\gamma}$. This term won't affect the shape of the diffracted wavefunction.

Using the Jacobi-Anger expansion,

$$e^{iz\cos\theta} = \sum_{\ell=-\infty}^{\infty} i^{\ell} \mathrm{J}_{\ell}(z) e^{i\ell\theta} \tag{2.66}$$

we can rewrite the position-dependent term in the transmission function:

$$e^{i\tilde{k}(\Delta h/2\cos(m\phi+k_d x))} = \sum_{\ell=-\infty}^{\infty} i^{\ell} \mathrm{J}_{\ell}(\tilde{k}\Delta h/2) e^{i\ell(m\phi+k_d x)} \tag{2.67}$$

We can now apply the convolution theorem to separately transform the azimuthal phase and the linear phase; we'll see that the Fourier transformation of the azimuthal phase is trivial in cylindrical coordinates. Let's define

$$t_r(x,y) = \sum_{\ell=-\infty}^{\infty} i^{\ell} \mathrm{J}_{\ell}(\tilde{k}\Delta h/2) e^{i\ell(m\phi+k_d x)} \tag{2.68}$$

$$f(x,y) = e^{i\ell m\phi} \tag{2.69}$$

$$g(x,y) = e^{i\ell k_d x} \tag{2.70}$$

$$t_r(x,y) = \sum_{\ell=-\infty}^{\infty} i^{\ell} \mathrm{J}_{\ell}(\tilde{k}\Delta h/2) f(x,y) g(x,y) \tag{2.71}$$

With the convolution theorem, we see

$$\tilde{t}_r(x,y) = \sum_{\ell=-\infty}^{\infty} i^{\ell} \mathrm{J}_{\ell}(\tilde{k}\Delta h/2) \tilde{f} * \tilde{g} \tag{2.72}$$

Let's evaluate $\tilde{f}$ and $\tilde{g}$. For $\tilde{f}$, we see

$$\tilde{f} = \frac{1}{(2\pi)^2} \int e^{i\ell m\phi} e^{-i(xq_{x'}+yq_{y'})} \mathrm{d}x \ \mathrm{d}y \tag{2.73}$$

$$\tilde{f} = \frac{1}{(2\pi)^2} \int e^{i\ell m\phi} e^{-i(\mathbf{q}_{\mathbf{r}'}\cdot\mathbf{r})} \mathrm{d}\phi \ r\mathrm{d}r \tag{2.74}$$

$$\tilde{f} = \frac{1}{(2\pi)^2} \int e^{i\ell m\phi} e^{-i(q_{\mathbf{r}'} r\cos(\phi-\phi_q)} \mathrm{d}\phi \ r\mathrm{d}r \tag{2.75}$$

Using the Jacobi-Anger expansion again, we see

$$\tilde{f} = \frac{1}{(2\pi)^2} \sum_{n=-\infty}^{\infty} i^n \int e^{i\ell m\phi} \mathrm{J}_n(-q_{\mathbf{r}} r) e^{in(\phi-\phi_q)} \mathrm{d}\phi \ r\mathrm{d}r \tag{2.76}$$

As

$$\int_0^{2\pi} e^{iN\phi} \mathrm{d}\phi = \frac{1}{iN}(e^{2\pi iN} - e^0) = 0 \tag{2.77}$$

for integer, non-zero N, and as

$$\int_0^{2\pi} e^0 \mathrm{d}\phi = 2\pi \tag{2.78}$$

we see that

$$\int_0^{2\pi} e^{iN\phi} \mathrm{d}\phi = 2\pi\delta_{N,0} \tag{2.79}$$

We can therefore evaluate the ϕ integral to calculate $\tilde{f}$.

$$\tilde{f} = \frac{1}{2\pi} \sum_{n=-\infty}^{\infty} i^n \delta_{\ell m+n,0} e^{-in\phi_q} \int_0^{\infty} \mathrm{J}_n(-q_{\mathbf{r}} r) r\mathrm{d}r \tag{2.80}$$

$$\tilde{f} = \frac{1}{2\pi} i^{-\ell m} e^{i\ell m\phi_q} \tilde{f}_r(k_r) \tag{2.81}$$

In practice, we use an aperture or a radial profile in the hologram to affect the radial distribution of the hologram, and therefore the diffracted wavefunction, so we can

leave $\tilde{f}_r(k_r)$ as an unknown function of a real radial distribution. Let's now evaluate the more trivial $\tilde{g}$, which produces a more familiar δ-function.

$$\tilde{g} = \frac{1}{(2\pi)^2} \int e^{i\ell k_d x} e^{-i(xq_{x'} + yq_{y'})} \mathrm{d}x \ \mathrm{d}y \tag{2.82}$$

$$\tilde{g} = \delta(q_{x'} - \ell k_d) \tag{2.83}$$

Therefore, putting the two pieces together, we can evaluate $\tilde{t}_r$ and thus $\tilde{t}$. From (2.65) and (2.72), we see

$$\tilde{t}(q_{x'}, q_{y'}) = Ae^{i\gamma} \tilde{t}_r \tag{2.84}$$

$$\tilde{t}(q_{x'}, q_{y'}) = Ae^{i\gamma} \sum_{\ell=-\infty}^{\infty} i^{\ell} \mathrm{J}_{\ell}(\tilde{k}\Delta h/2) \tilde{f} * \tilde{g} \tag{2.85}$$

$$\tilde{t}(q_{x'}, q_{y'}) = Ae^{i\gamma} \sum_{\ell=-\infty}^{\infty} i^{\ell-\ell m} \mathrm{J}_{\ell}(\tilde{k}\Delta h/2) \left(\frac{1}{2\pi} e^{i\ell m \phi_q} \tilde{f}_r(k_r) * \delta(q_{x'} - \ell k_d) \right) \tag{2.86}$$

$$\tag{2.87}$$

Inserting this transmission function into (2.28), we have

$$\psi(\mathbf{r'}) \propto e^{ikz'} \tilde{t}(q_{x'}, q_{y'}) \tag{2.88}$$

$$\psi(\mathbf{r'}) \propto e^{ikz'} \sum_{\ell=-\infty}^{\infty} i^{\ell} \mathrm{J}_{\ell}(\tilde{k}\Delta h/2) \left(e^{i\ell m \phi_q} \tilde{f}_r(k_r) * \delta(q_{x'} - \ell k_d) \right) \tag{2.89}$$

$$\tag{2.90}$$

We now see, exactly as we'd hope, that a holographic grating defined by (2.58) produces diffraction orders with $m\ell\hbar$ orbital angular momentum in the ℓ diffraction order.

Transfer of Orbital Angular Momentum from Photons to Electrons

Tyler Harvey

23rd June 2017

Introduction to Electron-Photon Interactions

I am interested in interactions that cause orbital angular momentum transfer from a laser to a free electron state. As both electron OAM and interaction between lasers and free electrons are both fairly new fields, there are many open questions here. I will focus on one basic question and one practical question:

- What does a single scattering event between a photon and an electron look like in a cylindrically symmetric basis?
- Can this interaction be employed to prepare an electron in an OAM state?

Let's first explore the first question, as we must before we can think about the second.

Scattering in a Cylindrically Symmetric Basis

Setup

Let's calculate the transition amplitude corresponding to photon absorption or emission from a single electron, as shown in Figure 8.

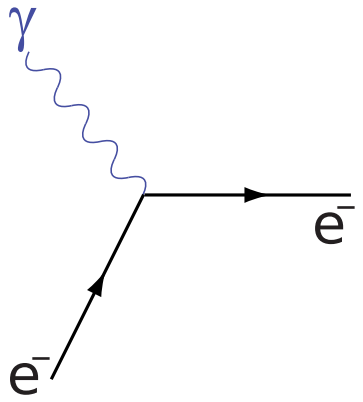

FIGURE 8. Diagram of electron-photon interaction
Feyman diagram for photon absorption or emission by an electron. .

We'll stick to the conventions of Cohen-Tannoudji et al. [72] and define

$$H = H_0 + H_I \tag{2.91}$$

$$H_0 = \frac{p^2}{2m_e} + \sum_i \hbar\omega_i \left(a_i^\dagger a_i + \frac{1}{2}\right) \tag{2.92}$$

$$H_I = \frac{1}{2m_e}\left(e\left(\mathbf{p}\cdot\mathbf{A} + \mathbf{a}\cdot\mathbf{p}\right) + e^2A^2\right) \tag{2.93}$$

The amplitude for absorption is

$$\mathscr{T}_{\text{abs}} = \frac{e}{2m_e}\left\langle\psi_f\right|_e \left\langle 0\right|_\gamma \mathbf{p}\cdot\mathbf{A} + \mathbf{A}\cdot\mathbf{p}\left|\psi_i\right\rangle_e \left|1_{\mathbf{k},\sigma}\right\rangle_\gamma \tag{2.94}$$

where the electron state is represented as $\left|\psi\right\rangle_e$ the photon state as either a single photon or the vacuum. $\mathbf{p}$ is the electron momentum operator and $\mathbf{A}$ is the vector potential. Emission is the complex conjugate of this amplitude.

In the plane wave basis, Cohen-Tannoudji et al. write [72] the vector potential as

$$\mathbf{A}(\mathbf{r}) = \int \mathrm{d}\mathbf{k} \sum_\sigma \mathscr{A}_\omega \left(\hat{\boldsymbol{\epsilon}}_\sigma a_\sigma(\mathbf{k}) e^{i\mathbf{k}\cdot\mathbf{r}} + \hat{\boldsymbol{\epsilon}}_\sigma^* a_\sigma^\dagger(\mathbf{k}) e^{-i\mathbf{k}\cdot\mathbf{r}}\right) \tag{2.95}$$

Birula and Birula show [73] that the creation and annihilation operators can be rewritten in the Bessel basis, a plane wave-like cylindrically symmetric basis, by integrating over the azimuthal angle in momentum space, ϕ_k:

$$a_\sigma(k_z, k_\perp, m) = \frac{1}{2\pi}\int_0^{2\pi} \mathrm{d}\phi_k e^{-im\phi_k} a_\sigma(\mathbf{k}) \tag{2.96}$$

We can therefore rewrite the vector potential in the Bessel basis if we perform the integral over ϕ_k in (2.95). To do so, we just first need to perform the Jacobi-Anger expansion:

$$e^{i\mathbf{k}\cdot\mathbf{r}} = e^{ik_z z} e^{ik_\perp \rho\cos(\phi-\phi_k)} = e^{ik_z z}\sum_m i^m J_m(k_\perp\rho) e^{im(\phi-\phi_k)} \tag{2.97}$$

where $k_\perp$ and ρ are the magnitudes of the components of momentum and position, respectively, that lie in a plane perpendicular to $\hat{z}$. If we do so and integrate over ϕ_k, (2.95) becomes

$$\begin{aligned}\mathbf{A}(\mathbf{r}) = \int \mathrm{d}k_z k_\perp \mathrm{d}k_\perp \sum_{\sigma,m} 2\pi\mathscr{A}_\omega \big(&\hat{\boldsymbol{\epsilon}}_\sigma a_\sigma(k_z, k_\perp, m) e^{ik_z z} e^{im\phi} i^m J_m(k_\perp\rho) + \\ &\hat{\boldsymbol{\epsilon}}^*_\sigma a^\dagger_\sigma(k_z, k_\perp, m) e^{-ik_z z} e^{-im\phi} i^{-m} J_m(k_\perp\rho)\big)\end{aligned} \tag{2.98}$$

We can see transfer of angular momentum from photons to electrons easily if we also use a Bessel basis for the absorbed or emitted photon state, denoted $|1_{\kappa_z,\kappa_\perp,n,\sigma_0}\rangle_\gamma$ and for the electron state, denoted $|k_{z_i}, k_{\perp_i}, m_i\rangle_e$. With eigenstates of the Bessel basis for both, absorption of a photon co-propagating with an electron is represented by

the amplitude

$$\mathscr{T}_{\text{abs-cyl}} = \frac{e}{2m_e}\int \mathrm{d}k_z k_\perp \mathrm{d}k_\perp \sum_{\sigma,m} 2\pi\mathscr{A}_\omega \left\langle k_{z_f}, k_{\perp_f}, m_f\right|_e \left\langle 0\right|_\gamma (\mathbf{p}\cdot\hat{\boldsymbol{\epsilon}}_\sigma \phi_{k_z,k_\perp,m}(\mathbf{r}) + \phi_{k_z,k_\perp,m}(\mathbf{r})\mathbf{p}\cdot\hat{\boldsymbol{\epsilon}}_\sigma)\, a_\sigma(k_z,k_\perp,m)\left|k_{z_i},k_{\perp_i},m_i\right\rangle_e \left|1_{\kappa_z,\kappa_\perp,n,\sigma_0}\right\rangle_\gamma \tag{2.99}$$

where $\phi_{k_z,k_\perp,m}(\mathbf{r}) = e^{ik_z z}e^{im\phi}i^m J_m(k_\perp\rho)$, which simplifies to

$$\mathscr{T}_{\text{abs-cyl}} = \frac{e}{2m_e}\kappa_\perp 2\pi\mathscr{A}_\omega \left\langle k_{z_f}, k_{\perp_f}, m_f\right|_e \mathbf{p}\cdot\hat{\boldsymbol{\epsilon}}_{\sigma_0}\phi_{\kappa_z,\kappa_\perp,n} + \phi_{\kappa_z,\kappa_\perp,n}\mathbf{p}\cdot\hat{\boldsymbol{\epsilon}}_{\sigma_0}\left|k_{z_i},k_{\perp_i},m_i\right\rangle_e \tag{2.100}$$

We can now see that there's clear transfer of orbital angular momentum, as the operator $e^{im\phi}$ raises orbital angular momentum:

$$e^{im\phi}\left|k_{z_i},k_{\perp_i},m_i\right\rangle \propto \left|k_{z_i},k_{\perp_i},m_i+m\right\rangle \tag{2.101}$$

Photon spin angular momentum, too, can be transfered to electron orbital angular momentum. If the photon is circularly polarized with helicity $\sigma = \pm 1$, then $\hat{\boldsymbol{\epsilon}}_\sigma = \hat{\mathbf{x}} + i\sigma\hat{\mathbf{y}}$. As

$$\mathbf{p}\cdot\hat{\boldsymbol{\epsilon}}_\sigma = p_x + i\sigma p_y = (p_\perp + i\sigma p_\phi)\, e^{i\sigma\phi_p}, \tag{2.102}$$

and as $e^{im\phi_p}$ also raises orbital angular momentum,[1]

$$e^{\sigma i\phi_p}\left|k_{z_i},k_{\perp_i},m_i\right\rangle \propto \left|k_{z_i},k_{\perp_i},m_i+\sigma\right\rangle, \tag{2.103}$$

[1]This can be shown easily in two ways. One is to project onto a plane wave basis: $\langle\mathbf{k}|\, e^{i\sigma\phi_p}\left|k_{z_i},k_{\perp_i},m_i\right\rangle = e^{i\sigma\phi_p}\left\langle\mathbf{k}|k_{z_i},k_{\perp_i},m_i\right\rangle \propto e^{i(\sigma+m_i)\phi_k}$. Another is to protect onto a position basis: $\langle\mathbf{r}|\mathbf{p}\cdot\hat{\boldsymbol{\epsilon}}_\sigma|\psi\rangle = e^{i\sigma\phi}\left(\frac{\partial}{\partial\rho} + \frac{i\sigma}{\rho}\frac{\partial}{\partial\phi}\right)\psi(\mathbf{r})$.

we see that that absorption of a photon with helicity σ contributes σ to the z-component of the orbital angular momentum of an electron in free space.

Transition probability

We must enforce energy conservation to calculate a transition probability in the long-interaction-time limit. Energy and momentum cannot simultaneously be conserved in absorption or emission of a single photon by a single free electron, as $\hbar kc \gg \frac{\hbar^2 k^2}{2m_e}$, so we'll have to consider other vertices to calculate a transition probability for interaction with monochromatic light.

If the kinetic energy of the electron is much larger than the energy of the photon and the electron is paraxial, i.e. $k_{z_i} \ |k_i|$, the largest transition amplitude comes from the A^2 term.[2]

The amplitude for absorption and re-emission of a photon with the A^2 term is

$$\mathscr{T}_{\text{scat}} = \langle k_{z_f}, k_{\perp_f}, m_f|_e \, \langle 1_{\kappa_{z_f},\kappa_{\perp_f},n_f,\sigma_f}|_\gamma \, \frac{e^2 A^2}{2m_e} \, |k_{z_i}, k_{\perp_i}, m_i\rangle_e \, |1_{\kappa_{z_i},\kappa_{\perp_i},n_i,\sigma_i}\rangle_\gamma \, . \tag{2.104}$$

If we act the annihilation and creation operators and ignore terms that won't conserve energy, we see that

$$\mathscr{T}_{\text{scat}} = \frac{4\pi^2 e^2}{m_e} \kappa_{\perp_i} \kappa_{\perp_f} \mathscr{A}_{\omega_i} \mathscr{A}_{\omega_f} \hat{\boldsymbol{\epsilon}}_{\sigma_i} \cdot \hat{\boldsymbol{\epsilon}}^*_{\sigma_f} \, \langle k_{z_f}, k_{\perp_f}, m_f|_e \, \phi_{\kappa_{z_i},\kappa_{\perp_i},n_i}(\mathbf{r}) \phi^*_{\kappa_{z_f},\kappa_{\perp_f},n_f}(\mathbf{r}) \, |k_{z_i}, k_{\perp_i}, m_i\rangle_e \tag{2.105}$$

where $\phi_{\kappa_{z_i},\kappa_{\perp_i},n_i}(\mathbf{r}) \phi^*_{\kappa_{z_f},\kappa_{\perp_f},n_f}(\mathbf{r}) = e^{i(\kappa_{z_i}-\kappa_{z_f})z} e^{i(n_i-n_f)\phi} J_{n_i}(\kappa_{\perp_i}\rho) J_{n_f}(\kappa_{\perp_f}\rho) i^{n_i-n_f}$.

[2]The second-order process associated with the $\mathbf{p}\cdot\mathbf{A}$ term, absorption and re-emission, is much smaller for a circularly polarized photon co-propagating with an electron. This second-order transition amplitude includes an extra factor that the A^2 term does not of (roughly) $\frac{(\mathbf{p}\cdot\hat{\boldsymbol{\epsilon}}_\sigma)^2}{\hbar^2 k_{z_i} \kappa_z}$; both k_{z_i} are much larger than any transverse wavevectors when both the electron and photon are paraxial.

Now, we see that energy conservation will produce a delta function that sets $\kappa_{z_i} = \kappa_{z_f}$ but leaves n_i and n_f free. Therefore, at lowest order, only orbital angular momentum can be transferred from a photon to an electron. One could prepare a pure electron orbital angular momentum state if one could efficiently prepare and post-select photons of arbitrary orbital angular momentum.

Practial Preparation of Electron OAM States

A much more practical and efficient experimental setup likely involves lasers. If, instead of two single photon states, we choose two coherent states, α and β, for our light, we see an angular Kaptiza-Dirac effect.

$$\mathscr{T}_{\text{2laser}} = \langle k_{z_f}, k_{\perp_f}, m_f|_e \langle \phi_{\alpha,\beta}|_\gamma \frac{e^2 A^2}{2m_e} |k_{z_i}, k_{\perp_i}, m_i\rangle_e |\phi_{\alpha,\beta}\rangle_\gamma \tag{2.106}$$

If we write our coherent states as

$$|\phi_{\alpha,\beta}\rangle_\gamma = c_\alpha |\alpha_{\kappa_z,\kappa_{\perp_1},m_1,\sigma}\rangle_\gamma + c_\beta |\beta_{\kappa_z,\kappa_{\perp_2},m_2,\sigma}\rangle_\gamma , \tag{2.107}$$

we see that the sum of two cross-terms in A^2 interfere. This is not surprising, as the laser beams also interfere.

The transition amplitude, without energy-non-conserving terms and loops, reduces to

$$\mathscr{T}_{\text{2laser}} = \frac{4\pi^2 e^2}{m_e} \kappa_{\perp_1} \kappa_{\perp_2} \mathscr{A}_\omega \mathscr{A}_\omega \langle k_{z_f}, k_{\perp_f}, m_f|_e \Big(\phi_{\kappa_z,\kappa_{\perp_1},m_1}(\mathbf{r}) \phi^*_{\kappa_z,\kappa_{\perp_2},m_2}(\mathbf{r}) + \phi^*_{\kappa_z,\kappa_{\perp_1},m_1}(\mathbf{r}) \phi_{\kappa_z,\kappa_{\perp_2},m_2}(\mathbf{r}) \Big) |k_{z_i}, k_{\perp_i}, m_i\rangle_e \tag{2.108}$$

Let's look at the interference:

$$\left(\phi_{\kappa_z,\kappa_{\perp_1},m_1}(\mathbf{r})\phi^*_{\kappa_z,\kappa_{\perp_2},m_2}(\mathbf{r}) + \phi^*_{\kappa_z,\kappa_{\perp_1},m_1}(\mathbf{r})\phi_{\kappa_z,\kappa_{\perp_2},m_2}(\mathbf{r})\right)$$
$$= c_\alpha c^*_\beta e^{i(m_1-m_2)(\phi+\frac{\pi}{2})} J_{m_1}(\kappa_{\perp_1}\rho)J_{m_2}(\kappa_{\perp_2}\rho) + c^*_\alpha c_\beta e^{-i(m_1-m_2)(\phi+\frac{\pi}{2})} J_{m_1}(\kappa_{\perp_1}\rho)J_{m_2}(\kappa_{\perp_2}\rho) \tag{2.109}$$

If $c_\alpha = |c|e^{i\delta_\alpha}$ and $c_\beta = |c|e^{i\delta_\beta}$, then

$$\left(\phi_{\kappa_z,\kappa_{\perp_1},m_1}(\mathbf{r})\phi^*_{\kappa_z,\kappa_{\perp_2},m_2}(\mathbf{r}) + \phi^*_{\kappa_z,\kappa_{\perp_1},m_1}(\mathbf{r})\phi_{\kappa_z,\kappa_{\perp_2},m_2}(\mathbf{r})\right)$$
$$= 2|c|^2 \cos\left(\Delta m(\phi+\frac{\pi}{2}) + \delta_\alpha - \delta_\beta\right) J_{m_1}(\kappa_{\perp_1}\rho)J_{m_2}(\kappa_{\perp_2}\rho) \tag{2.110}$$

where we've defined $\Delta m = m_1 - m_2$.

This transition amplitude tells us that the most significant final electron states produced by this interaction, aside from the initial state, are a superposition of states with $m_f = m_i + \Delta m$ and $m_f = m_i - \Delta m$.

Much like the linear Kapitza-Diract effect, this angular effect can be considered as diffraction of the electron by a standing wave of light–in this case, the interference pattern varies azimuthally. As the physical mechanism is the same–the linear Kapitza-Dirac effect is also caused by the A^2 term–we can therefore estimate the efficiency of the transition we're interested in based on previous calculations of the linear Kapitza-Dirac effect.

We expect that the probability of transition to a superposition of $m_f = m_i \pm \Delta m$ will be of order 0.1 with an incident electron kinetic energy of hundreds of eV and a nanosecond-pulsed laser with an energy of hundreds of micro-Joules per pulse focused to a spot size of tens of microns [74].

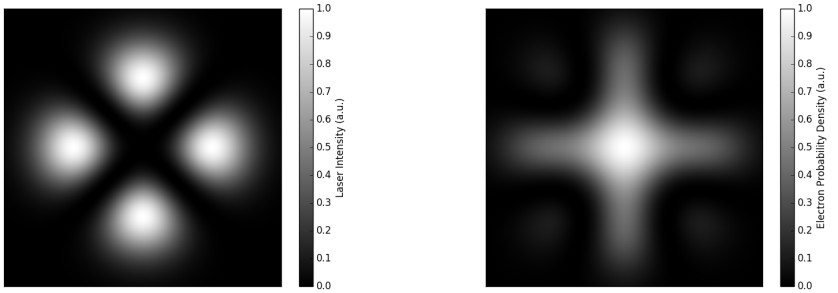

(a) (b)

FIGURE 9. Visualization of angular diffraction of electrons
(left) Simulated intensity of a laser described by a superposition of coherent states with $m_1 = +2$ and $m_2 = -2$ in a Laguerre-Gaussian basis (in contrast with the Bessel basis used in the text). (right) Qualitative visualization of the probability density of an electron diffracted by the laser shown to the left with amplitudes of 0.1 for the first-order diffracted modes, with higher-order diffracted modes excluded. (Note: this visualization excludes the effect of the laser on the radial part of the electron wavefunction.)

Open Questions

We've shown that several interactions can produce angular momentum transfer from photons to electrons. There may yet be others that are more practical. In particular, surface plasmons offer relief from the tight constraints of conservation of energy and momentum in free space. Recent work has shown [75, 76] that surface plasmons excited by a laser can efficiently transfer momentum and energy to free electrons. It may be similarly be possible to transfer angular momentum and energy with the appropriate surface plasmon resonance.

Similarly, it would be interesting to explore whether it's possible to efficiently diffract electrons from a superposition of co-propagating lasers with different orbital angular momenta and a slight linear momentum mismatch that produces a helical interference pattern. One might also wonder what happens if more laser beams are added–can one bias the angular momentum transfer in one direction?

Lastly, the most straightforward approach to preparation of a pure electron orbital angular momentum state with light might be the addition of a difference in the convergence angle of the two interfering lasers. The resulting interference pattern looks like a spiral zone plate [77, 78] and, in combination with an aperture in an appropriate plane, could produce a well-isolated pure orbital angular momentum state.

Chapter Conclusion

In this chapter, we introduced a method to produce electron orbital angular momentum states with phase diffraction gratings. We measured efficiency of a large range of diffraction gratings and showed that they matched reasonably well with our model. We also explored the possibility to prepare electron orbital angular momentum states using light. In the next chapter, we will consider applications of electron orbital angular momentum.

CHAPTER III

APPLICATION

Notes on Manuscripts

Note on 'Demonstration of Electron Helical Dichroism as a Probe of Local Chirality'

The first part of this chapter is from a submitted manuscript currently available on the arXiv: Tyler R Harvey *et al.*, arXiv:01810.

Benjamin McMorran and I developed the project idea together. I designed the experiment with help from co-authors. I conducted all experiments and took all data for the paper with help from co-authors. I wrote the manuscript with help from co-authors. I produced all figures.

Note on 'Holography in Scanning Transmission Electron Microscopy with Forked Diffraction Gratings'

The second part of the chapter is the skeleton of a manuscript that is in preparation. Benjamin McMorran contributed the project idea. I developed the theoretical model, with help from Colin Ophus, Fehmi Yasin, Jordan Chess, Vincenzo Grillo and Benjamin McMorran. The final manuscript, with experimental data, will likely include Burak Ozdol, Peter Ercius, Hao Yang, Jim Ciston and Roberto dos Reis as co-authors. These latter co-authors helped with specimen preparation, experiment design, and microscope control.

Demonstration of electron helical dichroism as a local probe of chirality

Tyler Harvey[1], Jordan Pierce[1], Jordan Chess[1], and Benjamin McMorran[1]

[1] Department of Physics, University of Oregon, Eugene, Oregon

02 July 2015

Chirality – the absence of symmetry under parity – lies at the heart of a variety of open research questions, including CP violation, the existence of an elementary majorana fermion, magnetic skyrmion behavior, and broken symmetry in the biochemistry of life. Chirality can also serve as an easy proxy for properties that are more difficult to directly measure. For example, sugar molecules consumed and produced by living organisms are always right-handed; to measure the concentration of a sugar in solution, one can measure the rotation of linearly polarized light passed through the solution [79].

Light has long been used to measure the chirality of ensembles of molecules, and more recently, increasingly small engineered structures. Circular dichroism (CD) is a standard spectroscopic tool for structural fingerprinting of molecules through measurement of three-dimensional chirality associated with molecular structure at a particular length scale [80]. Circular dichroism measures the difference in absorption of right- and left-circularly polarized light. Circularly polarized light carries chirality; the chirality of a massless particle is equivalent to its spin helicity,

$$h_S = \mathbf{S} \cdot \hat{\mathbf{p}} \tag{3.1}$$

where $\mathbf{S}$ is the spin angular momentum vector and $\hat{\mathbf{p}}$ is the propagation direction of incident light. Helicity, like chirality, is invariant under rotation and changes sign

under parity. Chirality-sensitive interactions between circularly polarized light and engineered chiral structures have also recently been predicted theoretically [81] and observed in experiments [82, 83, 84, 85]. Circular dichroism is sensitive to other kinds of chirality beyond material structure: X-ray magnetic circular dichroism (XMCD) characterizes the chirality associated with unpaired electron angular momentum in atoms that leads to magnetization [86].

However, circular dichroism techniques can only survey limited energy ranges with diffraction-limted spatial resolution. Standard light sources for visible circular dichroism typically can efficiently produce only the lowest energy UV light, and atmospheric oxygen strongly absorbs UV over 6 eV. However, UV circular dichroism spectra are necessary for amino acid [87] and protein secondary structural characterization [88]; X-ray circular dichroism allows for local, element-specific magnetization determination in magnetic materials [86]. Far-UV and X-ray circular dichroism spectra are typically gathered at synchrotron light sources [86, 89].

Electron microscopes, on the other hand, are equipped for spectroscopic analysis of materials over a stunning range of energies: a single electron microscope can quickly measure spectra across five orders of magnitude in energy. Monochromated, aberration-corrected electron microscopes can resolve excitations with energies as low as 10 meV (far-infrared) and well into keV (hard X-ray) *in combination* with sub-nanometer structural resolution on durable specimens [90]; good progress has been made towards atomic resolution on beam-sensitive materials [91]. In this Letter, we demonstrate sensitivity to chirality in a new kind of spectroscopy with helical electron states.

Free electrons can be prepared in states with helical wavefronts, called electron vortices. Electron vortices are eigenstates of L_z, the orbital angular momentum

operator along the direction of propagation $\langle \hat{\mathbf{p}} \rangle = \hat{\mathbf{z}}$. These states carry a property we call orbital helicity

$$h_L = \mathbf{L} \cdot \langle \hat{\mathbf{p}} \rangle = L_z. \tag{3.2}$$

The helicity of massive particles is a reference frame-dependent analogue of chirality: helicity is invariant under rotation, changes sign under parity, but also changes sign under a boost into a reference frame that reverses the direction of propagation. As seen in (3.2), orbital helicity behaves differently under transformation but is equivalent to orbital angular momentum in a given reference frame.

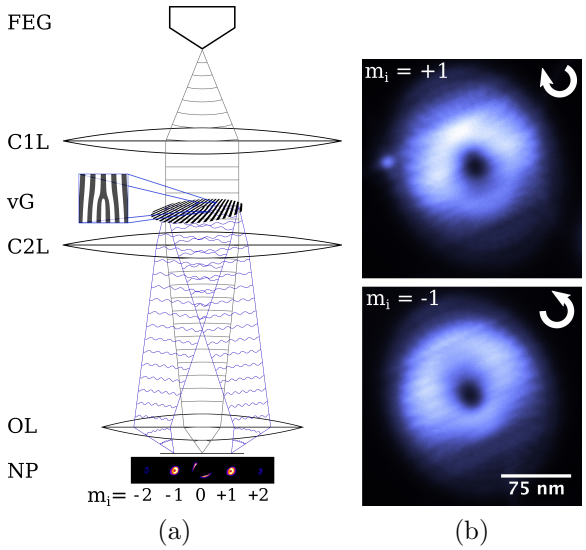

FIGURE 10. Probe-forming optics and image of probes
(a) Schematic of probe-forming optics. Electrons produced by the field-emission gun (FEG) are accelerated through a gun lens (not pictured) to 300 keV, and emerge from the upper condenser lens system (C1L) with planar wavefronts. The single-forked vortex diffraction grating (vG) adds an azimuthal phase and transverse momentum. The lower condenser lens system (C2L, OL) produces a focused far-field diffraction pattern at the specimen plane (NP); the nth diffraction order is a vortex with $m_i = n$ quanta of orbital helicity. (b) Transmission electron micrograph of an $m_i = -1$ (top) and $m_i = +1$ (bottom) electron vortices with nearly identical intensity distributions passed through silicon nitride substrate. Due to the phase singularity at the center of the beam, intensity is near zero there.

Electron eigenstates of orbital helicity can be prepared in a transmission electron microscope (TEM) by inclusion of an optical element that adds an azimuthal phase to the electron wavefunction [11, 12, 13]. The resultant wavefunction $\psi(\mathbf{x}) \propto e^{im\phi}$, where ϕ is the azimuthal angle and m is the orbital helicity quantum number ($\langle h_L \rangle = m\hbar$). Nanofabricated diffraction gratings [12, 13, 14, 15], material [11] and magnetic phase plates [18, 19] can produce beams with well-defined orbital angular momentum. The orbital helicity of electron vortices is well-suited for chirality measurement.

We report observation of electron helical dichroism on a material with chiral structure. Electron helical dichroism is the electron-vortex analogue of circular dichroism. We record an electron energy-loss (EEL) spectrum for the interaction of incident single-helix electron vortices (with incident orbital helicity quantum number $m_i = \pm 1$) with a specimen, and we post-select for the component of the outgoing wave that has zero final orbital helicity ($m_f = 0$). When the probability of multiple-scattering is low, electron intensity as a function of energy lost is approximately proportional to a differential scattering cross-section (for volume excitations) or a differential scattering probability (for surface excitations) [92]. An orbital helicity dependence in the electronic density of states appears as a peak in the electron helical dichroism spectra. Structural chirality of a specimen breaks the symmetry between positive- and negative-orbital helicity modes in the density of states. The dichroic interaction therefore probes the chirality of a specimen. Indeed, Asenjo-Garcia and García de Abajo recently predicted that dichroism is possible with electron vortices incident on a material with chiral structure [27].

The electron vortices employed in this experiment were produced in an FEI Titan transmission electron microscope (TEM) at 300 kV. We placed a nanofabricated forked diffraction grating in the condenser lens aperture of the microscope, as shown

in Fig. 10a [14]. We then focused the $+1$ (-1) diffracted order of the grating to a nanoscale probe in the plane of the sample to be analyzed; this beam carried $m_i = +1$ (-1) quanta of orbital helicity [13]. We examined chiral clusters of sub-100 nm-diameter aluminum nanoparticles, shown under planar illumination in Figure 11c. Aluminum nanoparticles were well-suited for study in our instrument, as the electronic states we excited are most likely surface plasmon resonances, and aluminum nanoparticles have documented surface plasmon resonances well into the UV (i.e. above 3 eV) [93]; these resonances were easily resolvable on our instrument, which has a spread in incident electron energy on the order of 1 eV.

A successful dichroism experiment depends on pre- and post-selection of angular momentum. In the case of optical and X-ray circular dichroism, in which the incident spin is fully transferred to the specimen when a photon is absorbed, a post-selection for a vacuum state means $m_f = 0$ and thus one quantum of angular momentum is always transferred to the specimen per photon. To measure electron helical dichroism, we must be more careful; the electron we send into a specimen exits with a spectrum of energies and orbital angular momenta. We seek to pick out the electron $m_f = 0$ state. We compare the inital and final states in circular dichroism and electron helical dichroism in Table 2. Electron energy loss measurement devices are commercially available for electron microscopes, but orbital angular momentum measurement is not so well-developed.

As yet, no quantitative, non-interferometric orbital angular momentum measurement technique exists for electrons. Interferometric measurement techniques [39, 40] cannot measure the orbital angular momentum of the incoherent superposition of energy and orbital angular momentum eigenstates produced by inelastic scattering in a specimen [25]. Fortunately, we did not need a sophisticated orbital angular

Particle used as probe	Initial probe state	Final state
Circularly polarized photon	$\|\mathbf{k_i}, m_s = \pm 1\rangle$	$\|\mathbf{0}\rangle$
Electron vortex	$\|\mathbf{k_i}, m_i\rangle$	$\|\mathbf{k_f}, m_f\rangle$

TABLE 2. Comparison of electron and photon dichroism
In a simplified decription of circular dichroism, measurement of absorption of a photon probe $|\mathbf{k_i}, m_s = \pm 1\rangle$, i.e. post-selection for the vacuum state $|\mathbf{0}\rangle$, automatically guarantees post-selection for a zero-angular momentum $m_s = 0$ final state as a zero-photon state carries no angular momentum. However, as massive electrons cannot annihilate to a vacuum state, we must carefully prepare the incident electron probe state $|\mathbf{k_i}, m_i\rangle$ and post-select for the final electron state $|\mathbf{k_f}, m_f\rangle$.

momentum measurement technique to select for the final state that corresponds to a transfer of one quantum of orbital angular momentum to the specimen.

Instead, we performed a simple post-selection for the zero-orbital angular momentum final state. We admitted only the center of an in-focus projection of the incident vortex beam on the specimen through an aperture, into the detector, as shown in Figure 11. This post-selection weights more heavily the component of the outgoing wave that transferred all incident orbital angular momentum to the specimen [94, 95]. We detail this post-selection in Section 3.3 in the Supplemental Material [96].

We sought to use this centered-aperture post-selection technique to control the angular momentum transfer to characterize the chirality of our aluminum nanoparticle cluster. We measured electron energy-loss spectrum pairs $J_+(E)$ for $m_i = +1$ and $J_-(E)$ for $m_i = -1$ and a more heavily weighted $m_f = 0$ final state with this post-selection. The peak in the dichroic electron energy-loss spectrum $J_\mathrm{d} = J_+ - J_-$ produced is a measurement of the difference in differential scattering probability $\frac{dP_\pm}{dE}$ for excitation of electronic states with opposite angular momentum:

$$J_\mathrm{d} \propto \frac{dP_+}{dE} - \frac{dP_-}{dE}. \tag{3.3}$$

An extended explanation of helical dichroism measurement can be found in Section 3.4 in the Supplemental Material [96].

Great care must be taken to produce a dichroism spectrum. A small misassignment of energies to peaks in any two consecutive energy loss spectra, such as our dichroic pairs, can produce apparently significant dichroism. The beam-specimen interaction recorded in the spectrometer can change in response to any small drift in the position of the specimen relative to the beam, caused by, for example, thermal expansion of the stage or fluctuations in temperature, pressure or stray magnetic or electric fields in the microscope room. We controlled for these potential issues in this experiment by intentionally re-aligning the beam, specimen and post-selection aperture and recording spectra over multiple timescales so that our measured uncertainty accurately reflects all relevant fluctuations in our microscope.

We also controlled for the possibility that small differences in the wavefunctions of beams with opposite incident helicity could produce spurious dichroism. We would expect to see such an artifact on specimens without explicit chiral structure. However, We observed no significant dichroic peaks for vortex beams incident on a symmetric aluminum nanoparticle or a silicon nitride substrate (Fig. 12a).

Dichroic spectra on the chiral aluminum cluster in Figure 12b show one significant UV peak at 3.5 ± 0.8 eV. This dichroic peak likely corresponds to excitation of surface plasmon vortex states. A surface plasmon vortex is a collective excitation of surface conduction electrons that carries orbital angular momentum, and therefore features the same azimuthal phase structure carried by an electron vortex [84]. Three observations support the identification of this peak as surface plasmon vortex excitation:

1. The majority of the post-selected wavefunction that enters the spectrometer does not directly pass through the aluminum particle, but rather passes near the surface, as shown in Figure 11d.

2. Isolated aluminum nanoparticles with diameters on the order of 100 nm have dipolar plasmon resonances on the order of 3 eV [93]; we should therefore expect a surface plasmon vortex mode on a chiral cluster of similarly-sized particles at the same order of magnitude.

3. Localized surface plasmon resonances are strongly sensitive to geometry, and in particular, surface plasmon vortex excitation is sensitive to structural chirality [84, 97]. Not every chiral cluster for which we recorded spectra showed a strong dichroic peak, which suggests a strong dependence on particle size, shape and cluster configuration. We discuss further observations of dichroism in section 3.5 in the Supplemental Material [96].

We therefore conclude that the observed dichroic peak on the chiral cluster likely corresponds to excitation of a surface plasmon vortex. There may be other significant contributions under 1 eV, or less signficant peaks of the opposite sign, that might be identifiable in an electron helical dichroism experiment conducted on an instrument with better energy resolution. A Nion HERMES instrument will soon be equipped to probe dichroism at much lower energies [98].

We have demonstrated electron helical dichroism on a chiral cluster of aluminum nanoparticles. We inferred that the dichroic peak represents a difference in the density of plasmon vortex states for this cluster. With further development, electron helical dichroism may be valuable for high-spatial resolution measurement of chirality over a large range of energies.

In particular, fully-developed chirality measurement with electrons demands a theoretically predicted and experimentally validated quantitative description of the relationship between the geometric chirality of a material and the magnitude of dichroism. If further work can shed light on this connection, electron helical dichroism may be employed to map out the chirality of single biomolecules and nanostructures with high spatial resolution over infrared, visible, ultraviolet and X-ray energies.

As structural determination of non-crystalline biomolecules at near-atomic resolution remains challenging [91, 99], structural biology stands to benefit from a new tool to measure chirality and infer structure in lieu of perfect atom-by-atom imaging. Furthermore, the ability to map surface plasmons with orbital angular momentum in the transmission electron microscope could illuminate future plasmon vortex-based device engineering. Lastly, the tools developed for this electron helical dichroism measurement may be transferrable to the advancement of other applications for dichroism measurement with electron vortices.

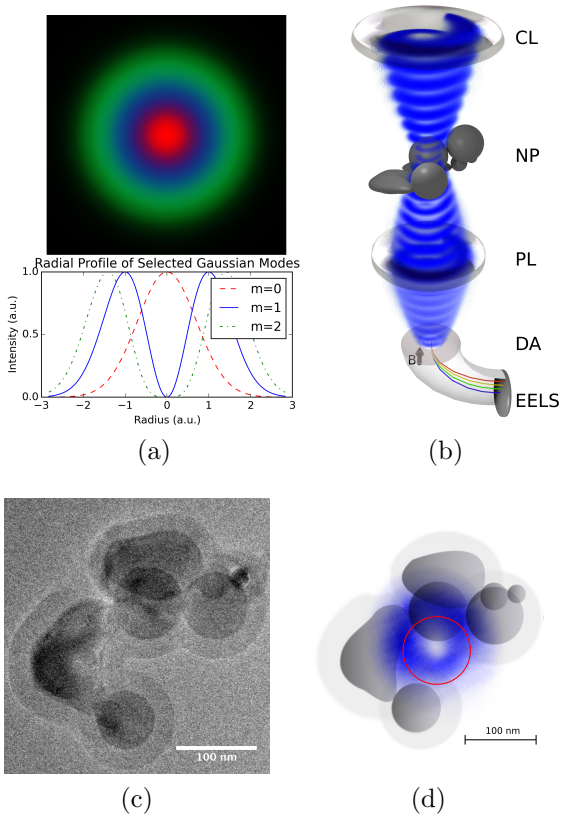

FIGURE 11. Post-specimen optics for post-selection
(a) Simulated two-dimensional cross-sectional intensity (top) and radial intensity profile (bottom) of fully coherent beams with angular momentum quantum numbers $m = 0$ (red), $m = 1$ (blue) and $m = 2$ (green) and other beam parameters held constant. Only the $m = 0$ beam has non-zero amplitude at the center of the beams. (b) Schematic of post-specimen optical configuration. The condenser lens system (CL) focuses the incident vortex onto the chiral nanoparticle cluster in the specimen plane (NP); the projector lens system (PL) re-forms an image of the vortex-on-specimen at the round detector entrance aperture (DA). The electron energy-loss spectrometer (EELS), highly simplified in this schematic, separates the outgoing wave by energy to produce a spectrum. (c) Transmission electron micrograph of chiral particle cluster under parallel illumination. (d) To-scale representation of chiral particles under vortex beam illumination. (grey) Aluminum particles (grey); (white) deposited hydrocarbon layer; (blue) $m_i = +1$ vortex beam; (red) actual spectrometer entrance aperture position used for one pair of electron energy-loss spectra.

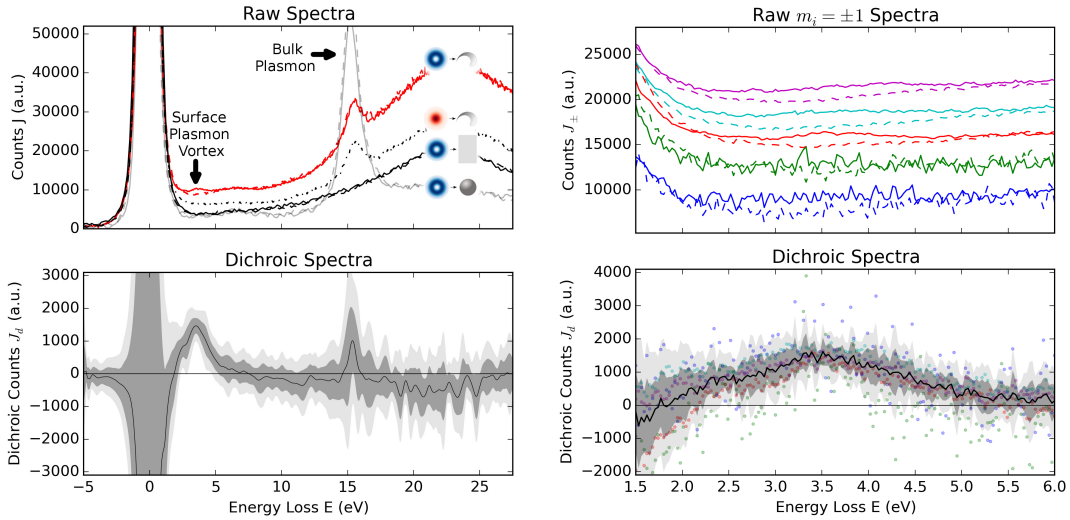

(a) (b)

FIGURE 12. Measured dichroic electron energy loss spectra

(a) (**top**) Comparison of electron energy-loss spectra for several incident wavefunction and specimen permutations. Dichroism appears at 3.5 ± 0.8 eV in the energy-loss spectrum pair $J_+(E)$ (red, solid) and $J_-(E)$ (dashed) produced by interaction of vortices with the chiral cluster of Al nanoparticles on a SiN_x substrate, shown in Fig. 11c. Spectrum pairs produced by interaction with the SiN_x substrate without nanoparticles (black) or a spherically symmetric nanoparticle (grey) show no significant differences. Energy loss from an $m_i = 0$ planar wave (black, dash-dot) due to interaction with the same Al chiral cluster has no distinct peaks in the 3.5 ± 0.8 eV range. (**bottom**) The average of all dichroic spectra (black line) shows a significant dichroic peak at 3.5 ± 0.8 eV. The 68% (dark grey region) and 95% (light grey region) confidence intervals are smoothed for clarity. The extreme width of the confidence intervals near zero energy loss illustrate that small variations in beam position cause large fluctuations in zero-loss intensity with our post-selection technique.

(b) (**top**) Electron energy-loss spectrum pairs J_+ for the interaction of a single-helix vortex beam with $m_i = +1$ (solid) and J_- for $m_i = -1$ (dashed) with the chiral cluster. Spectra are offset for clarity, and blue and green spectra were recorded with a shorter exposure to control for the possibity of beam position fluctuation. (**bottom**) Dichroic spectra $J_d(E)$ (colored points) calculated by subtraction of J_+ spectra from J_- spectra shown above; the average (black line) of all dichroic spectra deviates from zero dichroic counts with 68% confidence (dark grey region) only in this energy range. In fact, the dichroic peak deviates from zero with 95% confidence (light grey region) over a 1 eV range.

Supplemental Material for "Demonstration of electron helical dichroism as a local probe of chirality"

Tyler Harvey[1], Jordan Pierce[1], Jordan Chess[1], and Benjamin McMorran[1]

[1] Department of Physics, University of Oregon, Eugene, Oregon

23rd June 2017

Post-Selection

The post-selection technique we use in this work is based upon the spatial distribution of intensity caused by the singularity of vortex beams, which we developed in more detail in past work [94, 95].

The peak intensity of a vortex beam forms a ring (Fig. 10b). Inside this ring, the intensity of a fully coherent vortex drops to zero, because the azimuthal phase term of a vortex beam, $e^{im\phi}$, is singular at the center of the beam. The orbital angular momentum of a vortex beam is conserved in free space; in other words, the hole in the center of a vortex is stable under free-space propagation [100]. Equivalently, because transverse variations in phase grow infinitely large towards the center of the beam, the wavefunction of a vortex is diffraction-limited at its center and must develop a hole upon far-field propagation. A gaussian beam with no angular momentum, however, has no phase singularity and the peak intensity is at the center of the beam (Fig. 11a). We can utilize this difference in the position of peak intensity to perform a simple post-selection for the component of an outgoing wave that transferred all incident orbital angular momentum to the specimen.

If an incident electron vortex beam with $m_i = \pm 1$ quantum of angular momentum along the propagation axis transfers that angular momentum via interaction with a

specimen, the full-OAM-transfer $\Delta m \equiv m_i - m_f = \pm 1$ scattered component of the beam that has $m_f = 0$ will cause an increase in the intensity of the center of the beam. However, if the opposite angular momentum transfer occurs upon interaction, with $\Delta m = \mp 1$, the scattered component of the beam that corresponds to this interaction has $m_f = \pm 2$ and retains the singularity at the center of the beam. The distinct radial profiles of $m = 0$, $m = 1$ and $m = 2$ beams with a common radial quantum number are illustrated in Figure 11a. An aperture with a radius equal to the radius of peak intensity of the $m = 1$ vortex would allow 63% of the intensity of the $m = 0$ beam to pass, but only 8% of the $m = 2$ beam. Therefore, a spatial post-selection can serve as a qualitative measurement of orbital angular momentum transfer: any measurement that weights intensity at the center of the outgoing wave higher than intensity at larger radii will weight the scattering amplitude for the full-transfer $\Delta m = \pm 1$ transition more heavily than the $\Delta m = \mp 1$ transition.

Electron Helical Dichroism: an Introduction

There are 3 steps necessary for an electron helical dichroism experiment. First, one records the electron energy-loss spectrum $J_{\pm}(E)$ for the orbital angular momentum-transfer interaction (in this experiment, the $m_f = 0$ final state) for both positive and negative-orbital angular momentum initial states. Then, since the total intensity produced by the post-selection scheme described in Section 3.3 is highly sensitive to fluctuations in beam position, one must normalize the spectra so that non-chiral peaks are equally large. Lastly, one subtracts the negative-orbital angular momentum-transfer spectrum J_- from the positive-orbital angular momentum-transfer spectrum J_+ to produce an EHD spectrum. We used initial orbital angular momentum states $m_i = \pm 1$. As all $m_f = m_i$ signal will cancel in

the dichroic spectrum, since the probability for $\Delta m = 0$ inelastic scattering does not depend on the sign of m_i, and as higher-order orbital angular momentum transfer has negligible measured intensity due to our post-selection, the dichroic spectrum J_d is a measurement of the difference in differential scattering probability $\frac{dP_\pm}{dE}$ for excitation of surface plasmon vortices of opposite angular momentum:

$$J_\mathrm{d} = J_+(E) - J_-(E) \propto \frac{dP_+}{dE} - \frac{dP_-}{dE} \tag{3.4}$$

As current orbital angular momentum measurement techniques for electrons cannot post-select for a single final orbital angular momentum state from an incoherent superposition of states with varying energy, we use the spectrometer entrance aperture to post-select for the $m_f = 0$ final state.

We measured the electron energy-loss spectrum of the central scattered portion of an electron vortex with $m_i = \pm 1$ orbital angular momentum incident on a chiral distribution of aluminum nanoparticles. To do so, we centered the particle cluster and electron vortex over the entrance aperture of the electron energy-loss spectrometer in order to increase the ratio of the intensity of the central scattered $m_f = 0$ portion of the beam relative to the unscattered $m_f = m_i = \pm 1$ beam that passes into the spectrometer. Electron energy-loss spectra recorded this way are shown in Figure 12a. We then subtracted J_- spectra recorded for the $m_i = -1$ incident beam from the $m_i = +1$-incident J_+ spectra. These dichroic spectra are shown in Figure 12b. As the alignment of the incoming vortex, particle cluster and entrance aperture are crucial for good post-selection of the zero-orbital angular momentum component of the outgoing wave, we recorded J_+ and $J-$ spectrum pairs with five independent alignments of the beam, specimen and aperture. Indeed, we see significant variation

in the non-chiral plasmonic spectrum among the five spectrum pairs shown in Figure 12b, but a consistent difference between J_+ and J_-.

Supplemental Observation of Dichroism

As a further control for the possibility of misalignment-induced spurious dichroism, we performed an electron helical dichroism experiment on a second chiral cluster. We observed a similar peak at 1.8 ± 0.5 eV, and no other significant peaks, as shown in Figure 13a. We also reconstructured a three-dimensional model of the particle cluster by tomographic tilt series, shown in Figure 13b.

We recorded spectra on several other chiral clusters which showed a barely-significant or no significant dichroic peak in the same energy range. We speculate that this dearth of dichroism on some clearly chiral clusters results from the strong dependence of surface plasmon resonances on particle size, shape and cluster structure: we may have incidentally gathered spectra from a location on the cluster with a relatively weak plasmon resonance. Further development of electron helical dichroism may allow for rapid spectrum acqusition across all positions on a chiral structure.

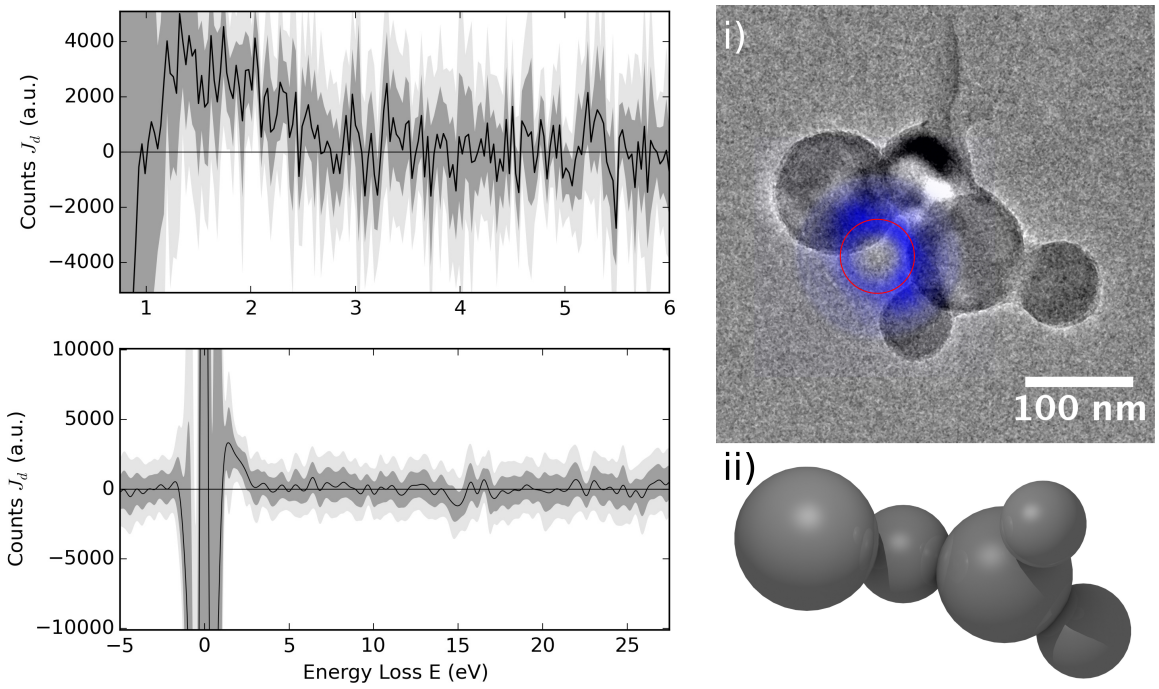

(a) (b)

FIGURE 13. More dichroic electron energy loss spectra
(a) Second observation of dichroic electron energy-loss spectra on a chiral particle cluster. (b) (i) Micrograph of particle cluster with orientation, beam positon (blue) and aperture position (red) used in acquisition of dichroic spectra shown in (a). (ii) Three-dimensional model of the chiral particle cluster, reconstructed by tomographic tilt series.

Holography in scanning transmission electron microscopy with forked diffraction gratings

Tyler Harvey[1], Colin Ophus[2], Fehmi Yasin[1], Jordan Chess[1], Vincenzo Grillo[3,4] and Benjamin McMorran[1]

[1] Department of Physics, University of Oregon, Eugene, Oregon

[2] National Center for Electron Microscopy, Lawrence Berkeley National Laboratory, Berkeley, California

[3] CNR-Istituto Nanoscienze, Centro S3, Via G Campi 213/a, I-41125 Modena, Italy

[3] CNR-IMEM Parco Area delle Scienze 37/A, I-43124 Parma, Italy

23rd June 2017

Introduction to STEM-Holography

The electron microscope offers the opportunity to directly image material structure and physical processes at extremely small length scales. Whereas many bulk measurements must be interpreted to infer microscopic structure or processes, in the transmission electron microscope, one can directly measure the positions of atoms and atomic columns or local shifts in transition energies with high precision. Scanning transmission electron microscopy (STEM) with a high-angle annular dark field detector (HAADF) has long offered highly interpretable contrast. However [101], the electron dose required to produce a good signal-to-noise ratio is high even on high-atomic-number materials, and becomes prohibitive for low-atomic-number materials that only weakly scatter electrons and may change in structure due to electron beam damage past a certain dose. Ptychography and matched illumination and detector interferometry (MIDI) offer a dose-efficient alternative for reasonably interpretable phase contrast in STEM, but as both techniques are only senstive to local phase

variations surrounding a tightly-focused probe, both techniques effectively high-pass-filter the phase contrast image [102, 103, 104].

Electron holography offers a more interpretable reconstruction of phase with respect to a vacuum reference wave, but high dose is necessary to accurately reconstruct phase with high spatial resolution. In this manuscript, we develop a method to reconstruct phase measured from the interference of multiple STEM probe beams produced with an electron diffraction grating. This technique is called STEM-holography in past works that used or assumed a pre-specimen biprism to produce multiple probes; we retain that name in this manuscript. Cowley issued a clever proposal for STEM-holography that relied on the assumption of exactly two beams. We develop a more general approach to handle the three or more beams produced by a realistic diffraction grating in an instrument that does not contain specialized apertures to block the additional beams. This general approach also allows us to consider STEM-holography with vortex beams.

An electron diffraction grating has several advantages over a biprism for STEM-holography. The transverse coherence length necessary for optimal fringe visibility is much lower: when a biprism is used to split the beam, the fringe visibility decreases with the ratio of the transverse coherence length over the width of the illumination; when a grating is used to split the beam, the fringe visibility decreases with the ratio of the transverse coherence length over the grating period. A biprism produces two opposing half-circular probes in reprocal space, whereas a grating can produce probes with identical phase and amplitude distributions [1]. Lastly, a diffraction grating can produce electron beams with orbital angular momentum.

[1]Indeed, identical probes are necessary to realize the analysis method Cowley proposed. The optimal instrument designed to realize his proposal might be a STEM instrument with a diffraction grating in the condenser aperture and a second aperture at a crossover above the specimen to select only two beams.

Let us first consider STEM-holography with a straight diffraction grating, then add orbital angular momentum and consider the kinds of information we can access with that addition. In particular, vortex-STEM-holography provides access to out-of-plane magnetic fields.

Note to the reader: in this early version of this manuscript, some signs might be off and some normalization factors (such as the factor of 2π necessary for a properly normalized Fourier transform pair) may be omitted, but the basic mechanics of the model have been triple-checked by hand as well as numerically validated.

Simple Grating Analysis

First, let's introduce our notation. We'll use a pre-specimen probe wavefunction

$$\psi_i(\mathbf{x}) = a(\mathbf{x} - \mathbf{x}_p) \tag{3.5}$$

where $\mathbf{x}_p$ is the offset-position of our probe. If we assume a thin specimen, we can describe the interaction of the probe with the specimen as a multiplication by a specimen transfer function $t(\mathbf{x})$, resulting in a post-specimen wavefunction

$$\psi_f(\mathbf{x}) = a(\mathbf{x} - \mathbf{x}_p)t(\mathbf{x}) \tag{3.6}$$

and an interference pattern at the detector at probe position $\mathbf{x}_p$

$$G_p(\mathbf{k}) = |\psi_f(\mathbf{k})|_p^2 = \left(A_p^*(\mathbf{k}) * T^*(\mathbf{k})\right)\left(A_p(\mathbf{k}) * T(\mathbf{k})\right) \tag{3.7}$$

where $A_p(\mathbf{k})$ is the Fourier transform of $a(\mathbf{x} - \mathbf{x}_p)$. If we assume that we've used a diffraction grating to produce multiple sharply-peaked, evenly spaced probes, our

probe wavefunction is

$$a(\mathbf{x}-\mathbf{x}_p) = \sum_m c_m a_0(\mathbf{x} - m\mathbf{x}_0 - \mathbf{x}_p), \tag{3.8}$$

where $a_0(\mathbf{x})$ is sharply peaked at $\mathbf{x} = \mathbf{0}$ and thus

$$A_p(\mathbf{k}) = \sum_m c_m e^{-i\mathbf{k}\cdot(m\mathbf{x}_0+\mathbf{x}_p)} A_0(\mathbf{k}). \tag{3.9}$$

We have here assumed that the aperture function, or probe wavefunction, is identically A_0 for all probes. This assumption is valid for a straight diffraction grating with no phase structure. It would be easy to keep track of different phase distributions A_m for each probe for the case of a diffraction grating with non-trivial structure.

The simplest example of $A_0(\mathbf{k})$ is also the most commonly used: a round aperture.

$$A_0 = \begin{cases} 1 & \mathbf{q} < \mathbf{q}_{\max} \\ \\ 0 & \mathbf{q} \geq \mathbf{q}_{\max} \end{cases} \tag{3.10}$$

Let's plug this into (3.7).

$$G_p(\mathbf{k}) = \sum_{m,n} c_m^* c_n \left[\left(A_0^*(\mathbf{k}) e^{i\mathbf{k}\cdot(m\mathbf{x}_0+\mathbf{x}_p)}\right) * T^*(\mathbf{k})\right] \left[\left(A_0(\mathbf{k}) e^{-i\mathbf{k}\cdot(n\mathbf{x}_0+\mathbf{x}_p)}\right) * T(\mathbf{k})\right] \tag{3.11}$$

Using the property of plane-wave terms under convolution,

$$\left(f(x)e^{ikx}\right) * g(x) = \left[f(x) * \left(g(x)e^{-ikx}\right)\right] e^{ikx}, \tag{3.12}$$

we see that (3.11) can be rewritten as

$$G_p(\mathbf{k}) = \sum_{m,n} c_m^* c_n \left[A_0^*(\mathbf{k}) * \left(T^*(\mathbf{k}) e^{-i\mathbf{k}\cdot(m\mathbf{x}_0+\mathbf{x}_p)}\right)\right] \left[A_0(\mathbf{k}) * \left(T(\mathbf{k}) e^{i\mathbf{k}\cdot(n\mathbf{x}_0+\mathbf{x}_p)}\right)\right] e^{i\mathbf{k}\cdot((m-n)\mathbf{x}_0)}. \tag{3.13}$$

We can see that the specimen transfer function $t(\mathbf{x})$ is encoded in the set of plane waves $e^{i\mathbf{k}\cdot((m-n)\mathbf{x}_0)}$. How do we retrieve it? Let's consider a set of simiplifying assumptions to illustrate what (3.13) means.

We can immediately get some intuition by considering the limit that the specimen transfer function does not vary over the scale of the probe size. In the limit that $A_0(\mathbf{k}) = 1$, the probes are infinitely small, and

$$\left[A_0^*(\mathbf{k}) * \left(T^*(\mathbf{k}) e^{-i\mathbf{k}\cdot(m\mathbf{x}_0+\mathbf{x}_p)}\right)\right] \left[A_0(\mathbf{k}) * \left(T(\mathbf{k}) e^{i\mathbf{k}\cdot(n\mathbf{x}_0+\mathbf{x}_p)}\right)\right] \rightarrow t^*(m\mathbf{x}_0+\mathbf{x}_p) t(n\mathbf{x}_0+\mathbf{x}_p). \tag{3.14}$$

So, in the slowly-varying specimen limit, we see clearly that every plane wave in (3.13) of order $\ell = m - n$ carries information from beams that have passed through the specimen at probe positons separated by a distance $\ell\mathbf{x}_0$.

Let us now consider a massive simplification: all beams but the $m = 0$ and $m = +1$ beams are blocked, and $m = 0$ passes through vacuum $t(\mathbf{x}) = 1$ near $\mathbf{x} = 0$ over a region larger than the maximum range of $\mathbf{x}_p$. Now, (3.13) simplifies to

$$G_p(\mathbf{k}) = c_0^* c_1 A_0^*(\mathbf{k}) \left[A_0(\mathbf{k}) * \left(T(\mathbf{k}) e^{i\mathbf{k}\cdot(\mathbf{x}_0+\mathbf{x}_p)}\right)\right] e^{-i\mathbf{k}\cdot\mathbf{x}_0} + c.c. + G_0(\mathbf{k}, \mathbf{x}_p) \tag{3.15}$$

where G_0 corresponds to the $n = m$ terms that contain information only about the amplitude of the specimen transfer function. Let's now for simplicty ignore aberrations and assume A_0 is real. The Fourier transform of G_p will be clearer without the complex conjugations. Let's take it.

$$G(\mathbf{x}_p, \mathbf{x}) = \int \mathrm{d}\mathbf{k} e^{i\mathbf{k}\cdot\mathbf{x}} G_p(\mathbf{k}) \tag{3.16}$$

$$= c_0^* c_1 a_0(\mathbf{x}) * [a_0(\mathbf{x}) t(\mathbf{x} + \mathbf{x}_0 + \mathbf{x}_p)] * \delta(\mathbf{x} - \mathbf{x}_0) + c.c. + G_0(\mathbf{x}, \mathbf{x}_p) \tag{3.17}$$

$$\tag{3.18}$$

For clarity, let's take $\mathbf{x} \to \mathbf{x} + \mathbf{x}_0$–let's shift the first "diffraction" order of the Fourier transform into the center. This gets rid of the delta function, since convolving with a delta centered around zero is an identity operator. We'll now ignore the other terms; numerically, we'll perform a discrete Fourier transform over a window that only includes the term of interest.

We want an interpretable function of just $t(\mathbf{x}_p)$, but we have two position variables. Let's get rid of one. The simplest way to do this is to integrate over $\mathbf{x}$ with $a_0(\mathbf{x})$ as a kernel.

If $A_0^* = A_0$, this integral is very simple, as $a_0(\mathbf{x}) * a_0(\mathbf{x}) = a_0(\mathbf{x})$, wondrously [2].

---

[2]

$$a_0(\mathbf{x}) * a_0(\mathbf{x}) = \int \mathrm{d}\mathbf{x}' a_0(\mathbf{x}') a_0(\mathbf{x} - \mathbf{x}') \tag{3.19}$$

$$= \int \mathrm{d}\mathbf{x}' \int \mathrm{d}\mathbf{k} e^{i\mathbf{k}\cdot\mathbf{x}'} A_0(\mathbf{k}) \int \mathrm{d}\mathbf{k}' e^{i\mathbf{k}'\cdot(\mathbf{x}-\mathbf{x}')} A_0(\mathbf{k}') \tag{3.20}$$

$$= \int \mathrm{d}\mathbf{k} A_0(\mathbf{k}) \int \mathrm{d}\mathbf{k}' e^{i\mathbf{k}'\cdot\mathbf{x}} A_0(\mathbf{k}') \delta(\mathbf{k} - \mathbf{k}') \tag{3.21}$$

$$= \int \mathrm{d}\mathbf{k} |A_0(\mathbf{k})|^2 e^{i\mathbf{k}\cdot\mathbf{x}} = \int \mathrm{d}\mathbf{k} A_0(\mathbf{k}) e^{i\mathbf{k}\cdot\mathbf{x}} \tag{3.22}$$

$$= a_0(\mathbf{x}) \tag{3.23}$$

$$t_M(\mathbf{x}_p + \mathbf{x}_0) = \int \mathrm{d}\mathbf{x} a_0(\mathbf{x}) G(\mathbf{x}_p, \mathbf{x}) \tag{3.24}$$

$$= \int \mathrm{d}\mathbf{x} \int \mathrm{d}\mathbf{x}' c_0^* c_1 a_0(\mathbf{x}) a_0(\mathbf{x} - \mathbf{x}') \left[a_0(\mathbf{x}') t(\mathbf{x}' + \mathbf{x}_0 + \mathbf{x}_p) \right] \tag{3.25}$$

$$= \int \mathrm{d}\mathbf{x}' c_0^* c_1 |a_0(\mathbf{x}')|^2 t(\mathbf{x}' + \mathbf{x}_0 + \mathbf{x}_p) \tag{3.26}$$

$$= -c_0^* c_1 \mathrm{psf}(\mathbf{x}_p) * t(\mathbf{x}_p + \mathbf{x}_0) \tag{3.27}$$

We see that the object we've defined, which we call t_M to mean the measured transfer function, is exactly the specimen transfer function convolved with a point spread function $|a_0(\mathbf{x}')|^2$.

Forked Grating Analysis

If we use a forked diffraction grating, the biggest change to our formalism happens in (3.6). In principle, the interaction of the transverse components of the magnetic vector potential with a transverse electron wavefunction can be calculated exactly as a convolution in reciprocal space, we'll take a shortcut here. Even with shortcuts, though, the effective operator for the interaction is no longer diagonal in position space. The lowest-order interaction of an electron orbital angular momentum state with a magnetic field produces a constant phase shift (see (4.25),(4.43)). We will therefore treat the magnetic interaction as a unitary operator, for each each beam is an eigenstate. This approach should completely fail if there are rapid variations of the out-of-plane magnetic field over the size of each beam (over $a_0(\mathbf{x})$), but will roughly show us what to expect for an out-of-plane magnetic field that varies on the scale of $\mathbf{x}_0$, the separation between beams.

The unitary operator, acting on orbital angular momentum eigenstates, becomes

$$U_{\text{Larmor}} \left| m_\ell \right\rangle = e^{i\phi_{\text{Larmor}}(m_\ell)} \left| m_\ell \right\rangle \tag{3.28}$$

where m_ℓ is the orbital angular momentum quantum number, and

$$\phi_{\text{Larmor}}(m_\ell) = -m_\ell \sqrt{\frac{e}{8 m_e V_a}} \int_{-\infty}^{\infty} B_1(z) dz. \tag{3.29}$$

m_e is the electron rest mass, V_a is the accelerating voltage, and $B_1(z)$ describes the longitudinal profile of the magnetic field.

We can now use the model we developed above with small tweaks, and treat the Larmor phase as part of the specimen transfer function.

The easiest way to add orbital anguar momentum is to modify what we called the aperture function to include the azimuthal phase.

$$A_m(\mathbf{k}) = A_0(\mathbf{k}) e^{im\ell\phi} \tag{3.30}$$

This azimuthal phase produces an orbital angular momentum $m_\ell = m\ell$ in the mth diffraction order.

Now, (3.15) becomes

$$G_p(\mathbf{k}) = c_0^* c_1 A_0^*(\mathbf{k}) \left[\left(A_1(\mathbf{k}) e^{i\phi_{\text{Larmor}}(\ell)} \right) * \left(T(\mathbf{k}) e^{i\mathbf{k}\cdot(\mathbf{x}_0 + \mathbf{x}_p)} \right) \right] e^{-i\mathbf{k}\cdot\mathbf{x}_0} + c.c. + G_0(\mathbf{k}, \mathbf{x}_p) \tag{3.31}$$

Fortunately, although it's not trivial to show, it still appears to be true that $a_1^*(\mathbf{x})$ is an appropriate kernel. As we noted before, the convolution of an aperture-limited probe wavefunction with itself is trivial because the equivalent multiplication

in reciprocal space is trivial. Fortunately, orbital angular momentum is invariant under the Fourier transform, so, with approproate care towards signs and complex conjugation, we see that

$$a_1^*(\mathbf{x}) * a_0(\mathbf{x}) = a_1^*(\mathbf{x}) \tag{3.32}$$

which, as before, produces an all-real point spread function. In this case, that point spread function is donut-shaped:

$$t_M(\mathbf{x}_p + \mathbf{x}_0, \ell) = -c_0^* c_1 e^{i\phi_{\text{Larmor}}(\ell)} |a_1(\mathbf{x}_p)|^2 * t(\mathbf{x}_p + \mathbf{x}_0) \tag{3.33}$$

We therefore see with quick arguments that STEM-holography with a vortex grating provides sensitivity to the out-of-plane magnetic field. We already have some experimental evidence that this method can work [38]. In principle, it should be possible to flip the sign of ℓ and then subtract $t_M(-\ell)$ from $t_M(+\ell)$ to isolate the Larmor phase. In practice, this may be challenging, as small artifactual differences between the two signals could be much larger than the Larmor phase. Coupled with normal STEM-holography, this method may used to efficiently map electrostatic, in-plane magnetic and out of plane magnetic fields produced by a specimen.

We may also be able to access other kinds of information about a specimen with vortex-STEM-holography. We could, for example, consider integrating with respect to a modified kernel $a_1^*(\mathbf{x})e^{i\ell\phi}$ kernel that has the appropriate amplitude but no azimuthal phase. This kernel produces a point spread function with a leftover azimuthal phase, which might be interpreted as spiral phase-contrast STEM-holography [105]. More careful analysis of the elastic interaction of a vortex beam with a large chiral structure is necessary to predict whether chiral sensitivity in vortex-STEM-holography is feasible.

Chapter Conclusion

In this chapter, we demonstrated two applications of electron orbital angular momentum: for spectroscopic chirality determination, and for holographic magnetic field measurement. In the next chapter, we will consider methods to measure or postselect final electron orbital angular momentum states. Efficient postselection will make applications of electron orbital angular momentum involving inelastic interactions much more feasible and efficient.

CHAPTER IV

APPLICATION

Notes on Manuscripts

Note on 'Stern-Gerlach-like Approach to Orbital Angular Momentum Measurement'

The first part of this chapter is from Tyler Harvey *et al.*, *Phys. Rev. A* **95** 021801 (2017). https://doi.org/10.1103/PhysRevA.95.021801

I came up with the project idea, with inspiration from past simulations of electron vortex propataion in magnetic lenses that Dave Shook and Benjamin McMorran conducted [106]. I had been exploring the possibility to entangle orbital angular momentum with linear momentum for a while using a longitudinal magnetic field that linearly decreases in a transverse direction, like the original Stern-Gerlach experiment. With input from Vincenzo Grillo, I realized that a cylindrically symmetric field was far more sensible, as OAM is conserved, and the idea began to converge toward the question Dave Shook had explored: does the focal length of a magnetic lens depend on orbital angular momentum?

I wrote the manuscript, and made most figures. Vincenzo Grillo made one. I developed the model with help from Vincenzo Grillo.

Note on 'Efficient Sorting of Free Electron Orbital Angular Momentum'

The second part of this chapter is from Benjamin McMorran *et al.*, *New J. Phys.* **19** 023053 (2017). https://doi.org/10.1088/1367-2630/aa5f6f

Martin Lavery originally devised the idea as a method for measuring the orbital angular momentum of light [107]. He and Benjamin McMorran contributed the idea

to develop the same method for electrons. Benjamin McMorran noticed that an electrostatic needle produces the required phase for the unwrapper element; I then noticed that the corrector phase is a solution to Poisson's equation could also be easily produced electrostatically.

Benjamin McMorran wrote the introduction, conclusion, and the section on the unwrapper element with help from Martin and me. I wrote the section on the corrector element and much of the Appendices with help from Bejamin McMorran and Martin Lavery. I performed all electrostatic potential simulations and produced many of the figures.

Stern-Gerlach-like approach to electron orbital angular momentum measurement

Tyler Harvey[1], Vincenzo Grillo[2,3], and Benjamin McMorran[1]

[1] Department of Physics, University of Oregon, Eugene, Oregon

[2] CNR-Istituto Nanoscienze, Centro S3, Via G Campi 213/a, I-41125 Modena, Italy

[3] CNR-IMEM Parco Area delle Scienze 37/A, I-43124 Parma, Italy

28 February 2017

Introduction to Orbital Angular Momentum Measurement

How does one measure the orbital angular momentum (OAM) of the quantum state of an unbound, massive, charged particle after interaction with another particle or a material? Free electrons with OAM, also called electron vortices, are now routinely prepared in electron microscopes [11, 12, 13, 14, 15, 16, 18, 19, 77, 108, 109] and control of this new degree of freedom is widely recognized as a useful tool in the both the study of materials and basic physical processes [12, 25, 27, 34]. A variety of impressive techniques now exist to prepare an electron in an OAM state. Full control of free electron orbital angular momentum, though, demands good measurement tools.

One of the most promising potential applications of electron OAM–measurement of magnetization at atomic resolution via helical dichroism spectroscopy–serves as an excellent example of the importance of both preparation and post-selection in applications of electron OAM. Magnetic dichroism has, surprisingly, not yet been realized with electrons prepared in OAM states. This application is analogous to X-ray Magnetic Circular Dichroism (XMCD), a widely-used technique for magnetization measurement based on the ratios of core-transition peaks in left- and right-circularly polarized X-ray absorption spectra. There exists a crucial difference, though,

between circular dichroism–which involves controlled transfer of photon spin angular momentum–and helical dichroism–which involves controlled transfer of electron OAM [34]. Photons are massless and can be absorbed by materials, so the final state of a photon in a circular dichroism measurement is just the vacuum state. Electrons are massive, and carry away non-zero energy and angular momentum from an interaction. If we seek to gain the most information about a material in an electron spectroscopy experiment, we ought to measure both the final electron energy and OAM [1]. Helical dichroism can be made far more efficient with careful post-selection of electron OAM states. This insight, in fact, applies to many applications of electron OAM.

There are a wide range of applications of good OAM post-selection. Theoretical predictions and simulation suggest that electron impact ionization [30, 111], photoionization [112, 113], electron-atom scattering [114], material investigation with angle-resolved photoelectron spectroscopy [115] and electron energy loss spectroscopy [31], production of spin-polarized electrons [116], and even high-energy elementary particle collisions [23] can produce non-trivial final OAM states and could therefore benefit from OAM post-selection.

Several techniques have so far been developed for electron OAM measurement; they work well as quality-assurance tests for new OAM state preparation techniques. All have limitations that prohibit their application to post-selection of a single final state of an inelastic interaction. Indeed, two recent theoretical proposals that demand perfect post-selection of OAM final states for application of electron OAM to the study of materials recognized that existing techniques are not sufficient [27, 117]. Self-interferometric techniques [39, 40, 41, 108] depend on analysis of the spatial distribution an electron after a transformation. In general, inelastic interaction of an

[1]Simulations [110] suggest that a small dichroism effect does exist when one measures only the probability density of the final state–and therefore traces out OAM in the final state.

electron and a material produces mixed electron final states thanks to entanglement with the material. Mixed and superposed OAM states are extremely difficult to quantitatively measure with self-interferometric techniques [44]. Furthermore, energy-filtered TEM is necessary to isolate and analyze the spatial distribution of the states scattered to a given energy. Holographic phase-flattening [42, 43] can partially spatially isolate a single component of a mix of inelastically scattered final OAM states, but is currently fairly inefficient.

We propose a technique for OAM post-selection based on coupling of OAM to a spatially varing magnetic field. The effect is analogous to the coupling between spin and a spatially varying magnetic field that Stern and Gerlach employed in their demonstration of the quantization of spin [118]. In the Stern-Gerlach device, spins aligned (anti-aligned) with the magnetic field are pulled by the Zeeman interaction toward the side of the device with higher (lower) field strength. Unlike the Stern-Gerlach device for measurement of spin, we consider a cylindrically symmetric design for measurement of OAM. Cylindrical symmetry gaurantees conserve electron OAM through the measurement device [119] and control the Lorentz force [120, 121]. Fortunately, cylindrically symmetric, spatially varying magnetic fields find great use as electron round lenses [122]. We show that the coupling of OAM to the field of a magnetic round lens produces a shift in the focal length of a magnetic round lens. In this proposed device, electrons with orbital dipole moments aligned (anti-aligned) with the magnetic field are pulled inward toward (pushed outward away from) the strong magnetic field along the optic axis.

OAM-dependent Focusing Effect

An ideal measurement device introduces a unitary interaction that entangles a state of interest with a measurement apparatus state that lies in a separate Hilbert space [123]. In the case of electron orbital angular momentum measurement, we consider entangling orbital angular momentum states (the states of interest) with radial states (the measurement apparatus state). In other words, we seek to encode information about orbital angular momentum in the radial wavefunction of the electron and then measure the position of the electron. The simplest realization of such a measurement device is an orbital angular momentum-dependent lensing effect.

For a state propagating along the z-axis, the transfer function of a lens with focal length f on an electron with wavelength λ is

$$U_{\text{lens}} = e^{-i\frac{\pi\rho^2}{\lambda f}} \tag{4.1}$$

where ρ is distance from the z-axis in cylindrical coordinates (z, ρ, ϕ).

If instead we want an OAM-dependent focal length, we'll want to construct a transfer function

$$U = \exp\left(-i\frac{L_z\rho^2}{\hbar b^2}\right). \tag{4.2}$$

This transfer function produces a quantum non-demolition measurement of orbital anguar momentum: OAM is an eigenstate of both this transfer function and the free-space Hamiltonian, and OAM is encoded in the radial distribution of the electron wavefunction. The effect of this transfer function on an OAM state is visualized in Figure 14.

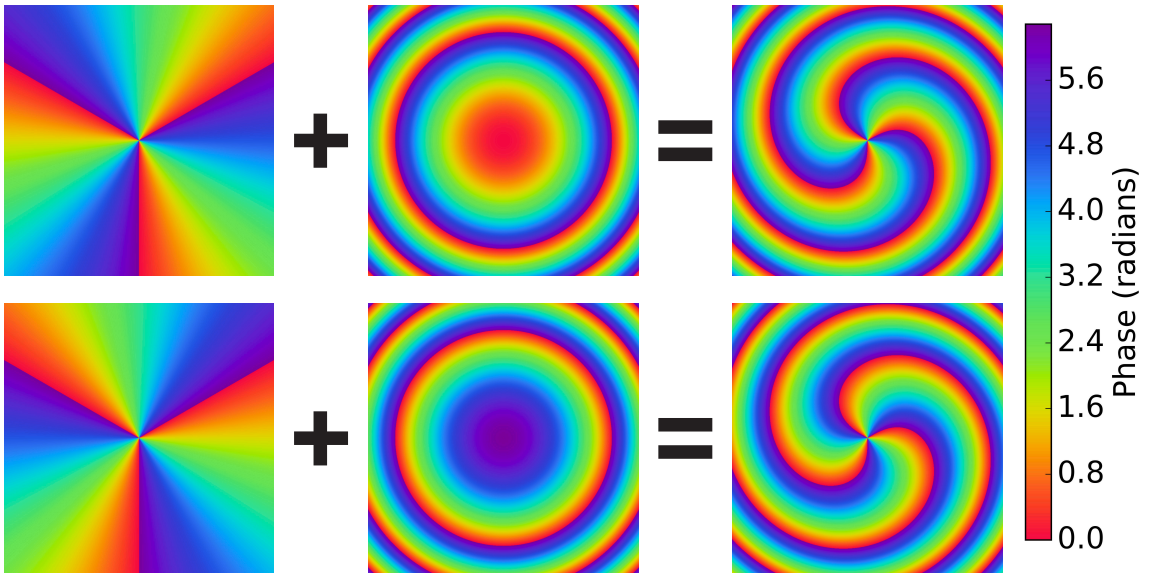

FIGURE 14. Phase effects of OAM-dependent lensing
Illstration of the effect of the orbital angular momentum-dependent lensing effect. Propagation of a wave with, in this case, $\pm 3\hbar$ OAM–and therefore an azimuthal phase (first column)–in a Hamiltonian with the OAM-dependent lensing term in equation (4.4) produces a parabolic phase (second column) in proportion to the OAM. The result is a spiralling phase with a winding magnitude and direction that depends on OAM (third column).

For quick insights into the potentials necessary to produce an OAM-dependent lensing effect, we notice that, in the short-time limit, the time evolution operator applies a phase modulation that's proportional to the Hamiltonian. (See Section 4.8 of the Supplemental Material for an explanation of a magnetic round lens in these terms.) So, we need to find a potential that will produce an $L_z\rho^2$ term in the electron Hamiltonian.

Counting powers of momentum and position, we see that only the $\mathbf{A}\cdot\mathbf{p}$ term can produce this term. In particular, we can see that we'll produce a transfer function like (4.2) with the vector potential

$$\mathbf{A} = \left(B_1(z)\frac{\rho}{2} - B_3(z)\frac{\rho^3}{8b^2} + ...O(\rho^5)\right)\hat{\boldsymbol{\phi}}. \tag{4.3}$$

where B_1 and B_3 describe the longitudinal profile of the field, i.e. $B_z = B_1(z) - B_3(z)\frac{\rho^2}{2b^2}$. This vector potential corresponds to a magnetic field that points along the $\pm\hat{\mathbf{z}}$-direction at the origin and curves outward away from the origin over a length scale b. We'll call b the dispersion length. The corresponding Hamiltonian for an electron in this vector potential includes two lensing terms,

$$H_{\text{lens}} = \frac{1}{8m_e}\left(e^2B_1^2 - \frac{eB_3L_z}{b^2}\right)\rho^2. \tag{4.4}$$

where $e = |e|$ is the magntide of the electron charge. The latter term produces an OAM-dependence in the focal length of the lensing effect. Figure 15 illustrates this lensing effect with multislice-simulated [124] propagation of superposed OAM states in this Hamiltonian [2] and ray trajectories calculated by numerical integration of the radial equation of motion. Filled intervals represent a range of classical trajectories that correspond to a single wavefunction.

The intuitive explanation in terms of the Zeeman potential $U_Z = -\boldsymbol{\mu}\cdot\mathbf{B}$ shows us that a magnetic dipole $\boldsymbol{\mu}$ aligned with a magnetic field $\mathbf{B}$ is pulled toward regions of higher field strength by a force $F_\rho = -\frac{\partial U_Z}{\partial\rho}$. An orbital magnetic dipole $\boldsymbol{\mu} = -\frac{e}{2m_e}\mathbf{L}$ is therefore pulled inward in a field when the longitudinal strength $B_z(z,\rho)$ decreases away from the optic axis (i.e. B_3 is nonzero) and the orbital dipole moment is aligned with the field. Although we treat only spin-unpolarized electrons here, it may be interesting in the future to examine the analogous effect on spin-polarized electrons. We expect that the OAM-dependent lensing effect, a spin-dependent lensing effect, and spin-to-orbital conversion via spin precession [116, 125] should all be independently observable in the non-relativistic limit.

[2] The non-unitarity of the lowest-order approximation to the transformation induced by L_z terms produces a small, unphysical loss of probability density with each slice.

The vector potential (4.3) above is an approximation to the vector potential of any cylindrically symmetric current distribution with azimuthal current flow. The dispersion length is related to the radial extent of the current distribution. In the case of a single loop of wire of radius R, b is just R and B_3 is on the same order as B_0, the magnetic field at the center of the loop. So, in fact, there exists a small OAM-dependence in the focal length of any standard magnetic round lens. The key to designing an orbital angular momentum measurement device is to isolate or maximize the OAM-dependence.

To do anything with an OAM-dependent lensing effect, we need to know the focal length of the lens. The focal length can be calculated analytically with two reasonable approximations: the paraxial approximation, and the thin lens approximation. The thin lens-paraxial Schrodinger equation [126] for an electron in our model vector potential (4.3) is a separable first-order differential equation,

$$2ik_z\frac{\partial\chi}{\partial z} = \frac{e}{\hbar}\left(B_1(z) - B_3(z)\frac{\rho^2}{4b^2}\right)m\chi + \frac{e^2B_1^2(z)}{4\hbar^2}\rho^2\chi \tag{4.5}$$

for a transverse wavefunction $\chi(\rho,\phi)$ with $L_z\chi = m\hbar\chi$. k_z is the longitudinal wavevector of the full wavefunction. Upon integration, we see that

$$U_{\text{lens}} = \exp\left(-i\frac{e^2}{8\hbar^2k_z}\int_{-\infty}^{\infty}\mathrm{d}z\left[B_1^2(z) - \frac{m\hbar}{eb^2}B_3(z)\right]\rho^2\right). \tag{4.6}$$

Comparing this with (4.1), we see that an initially collimated eigenstate of L_z with quantum number m that passes through the vector potential (4.3) will be focused at a distance f_m from the center of the potential, where

$$\frac{1}{f_m} = \frac{e^2}{8m_eE}\int_{-\infty}^{\infty}B_1^2(z) - \frac{m\hbar}{eb^2}B_3(z)\mathrm{d}z. \tag{4.7}$$

where E is the kinetic energy of the electron.

We can more simply rewrite this as

$$f_m = \frac{f_0}{1 - \Lambda m}, \tag{4.8}$$

where f_0 is the focal length of the $m = 0$ eigenstate and the OAM dispersion coefficient $\Lambda = \frac{\beta_0 \hbar}{eB_0 b^2}$ is a dimensionless constant that depends only on the peak field strength B_0, the dispersion length b, fundamental constants, and a dimensionless $O(1)$ number β_0 that depends on the shape of the current distribution. We calculate this focal length for several current distributions in Section 4.10 of the Supplemental Material. For small OAM dispersion Λ, therefore, focal length is approximately linear with OAM.

$$f_m \approx f_0 \left(1 + \Lambda m\right). \tag{4.9}$$

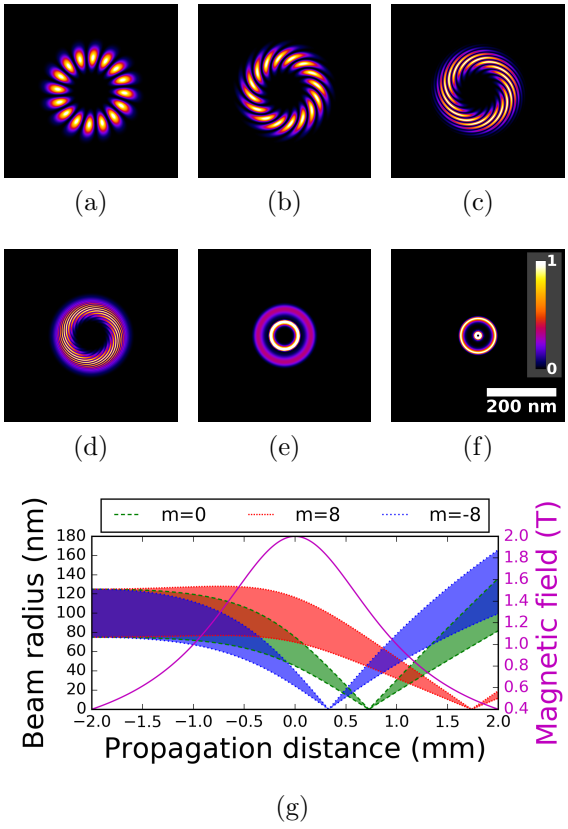

FIGURE 15. Propagation of OAM superpositions in a strongly OAM-dependent lens (top) Multislice-simulated intensities of a superposition of $m = \pm 8$ Laguerre-Gaussian orbital angular momentum states with $E = 80$ keV in a Glaser-model, i.e. equation (4.59), field with maximum field strength $B_0 = 2$ T, longitudinal extent $a = 1$ mm and an OAM dispersion length $b = 79$ nm, sampled at (a) -2.0 mm, (b) -1.5 mm, (c) -1.0 mm, (d) -0.5 mm, (e) 0.0 mm and (f) 0.5 mm from the center of the lens. (bottom) Ray trajectories for $m = -8$, $m = 0$ and $m = +8$ modes calculated by numerical integration of the radial equation of motion corresponding to the full Hamiltonian in equation (4.30) with a Glaser-model field.

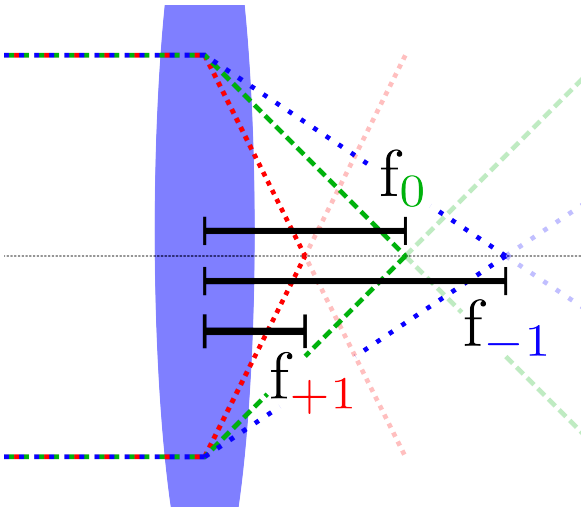

FIGURE 16. Schematic depicting the action of an OAM-dependent lens
Ray diagrams for a lens (blue disk) with a strongly OAM-dependent focal length f_m as given in (4.9). (red, dense dots) rays for $m = +1$ electrons; (green, dashes) rays for $m = 0$ electrons; (blue, loose dots) rays for $m = -1$ electrons.

Physical Realization of Device

When the current source for the vector potential in (4.3) is a superconducting ring, there's an easy physical interpretation of the OAM dispersion coefficient Λ. A superconducting ring of radius b encloses an area πb^2 and has an OAM dispersion coefficient inversely proportional to the number n of flux quanta in the ring, as $n \propto \frac{B_0 \pi b^2}{\Phi_0}$ and the flux quantum $\Phi_0 = \frac{h}{2e}$. We can therefore write the focal length of a lens made of superconducting ring as

$$f_m \approx f_0 \left(1 + \beta_1 \frac{m}{n}\right) \tag{4.10}$$

where β_1 is another $O(1)$ number.

If a lens can be constructed with a large OAM dispersion coefficient $\Lambda \sim 1$, the simplest application of this lensing effect to OAM measurement needs only a small aperture to select out one focused mode in the appropriate plane, as shown in Figure 17. In fact, preferential admission of individual modes into an aperture might be used to perform a simple helical dichroism experiment without incident OAM. One can see that the focal length (4.7) has an OAM-independent part that depends just on the magnitude of the lensing magnetic field and an OAM-dependent part that depends on both the magnitude and direction of the magnetic field. In other words, one can control OAM dispersion via the direction of the lensing field. With an aperture set to preferentially admit the $m = +1$ mode, one can flip the polarity of the lens and therefore flip the sign of OAM dispersion, and consequentially admit the $m = -1$ mode without physically moving anything. This experiment likely will require an exceptionally stable microscope and careful alignment to ensure that no other beam properties change upon a lens polarity flip.

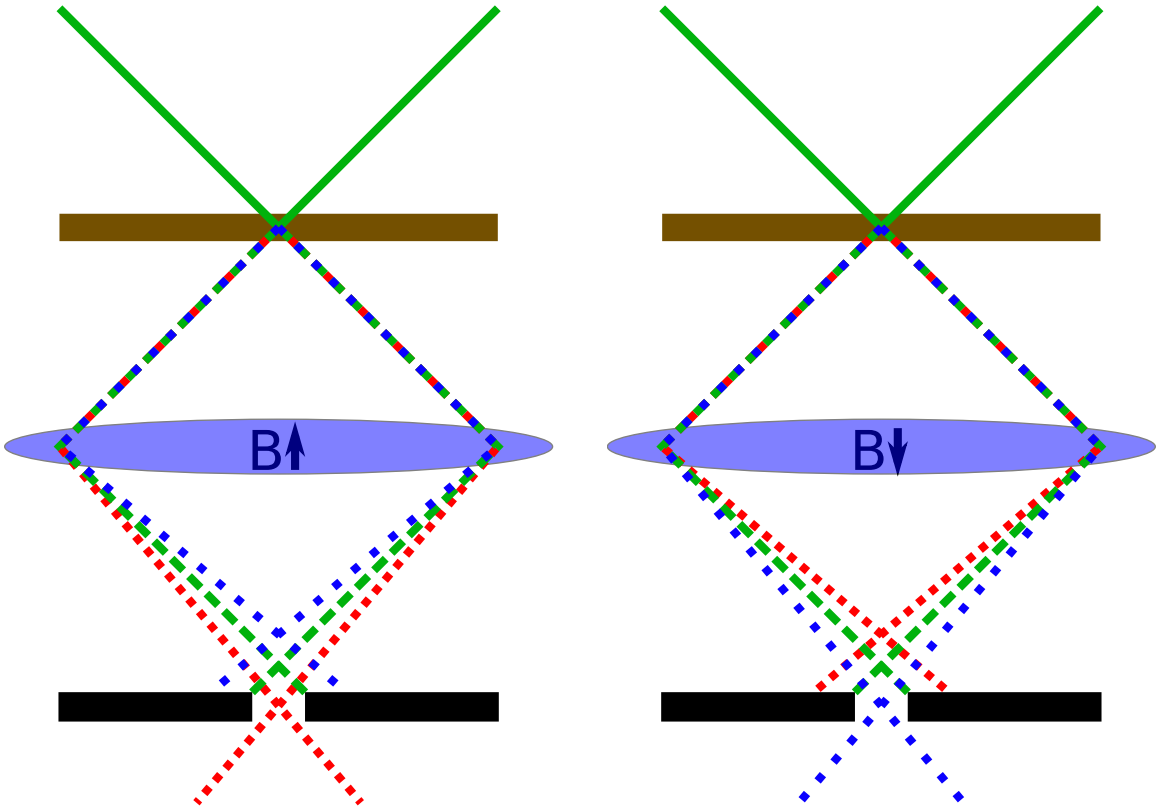

FIGURE 17. Schematic depicting a possible dichroism experiment
Schematic ray diagrams for a dichroism experiment based on the OAM-dependent lensing effect. Interaction with a specimen (brown) produces a mix of outgoing $m = +1$ (red, dense dots), $m = 0$ (green, dashes) and $m = -1$ (blue, loose dots) OAM eigenstates. (left) An aperture (black) preferentially admits the $m = +1$ OAM eigenstate. The $m = +1$ state has a longer focal length in the positive-polarity lens (blue disk). (right) The aperture preferentially admits the $m = -1$ OAM state when the lens polarity is flipped.

Several physical sources could produce a magnetic field with a significant OAM dispersion. The most obvious, but perhaps the most difficult to build, is a nanoscale solenoid. A solenoid with a radius on the order of 100 nm and a peak magnetic field on the order of 1 Tesla produces an OAM dispersion coefficient on the order of 0.1. The bound current density on the surface of a hole in an out-of-plane-polarized ferromagnetic thin film looks identical to the current density of a solenoid and could produce the same dispersion; such a hole would be far more easily nanofabricated and

has the advantage over a loop of wire that the normal lensing effect will be partially canceled in the hole. A pulsed laser with a radially polarized magnetic field has the appropriate symmetry. The laser used in a recent experiment to prepare well-defined electron momentum states [76], with a peak magnetic field of 0.334 T and a spot size of 50 um, would produce an OAM dispersion coefficient on the order of 10^{-6}. This might be improved by several orders of magnitude with plasmonic field enhancement.

It is also likely that a more detailed analysis of non-trivial current distributions and electron propagation through them, including thick lens effects, could reveal other ways to maximize $B_3(z)/b^2$. In particular, for slower electrons, where adiabatic invariance of the magnetic moment can be assumed [127], it may be possible to analytically derive OAM-dependent effects in the propagation of electrons through a magnetic bottle or magnetic mirror.

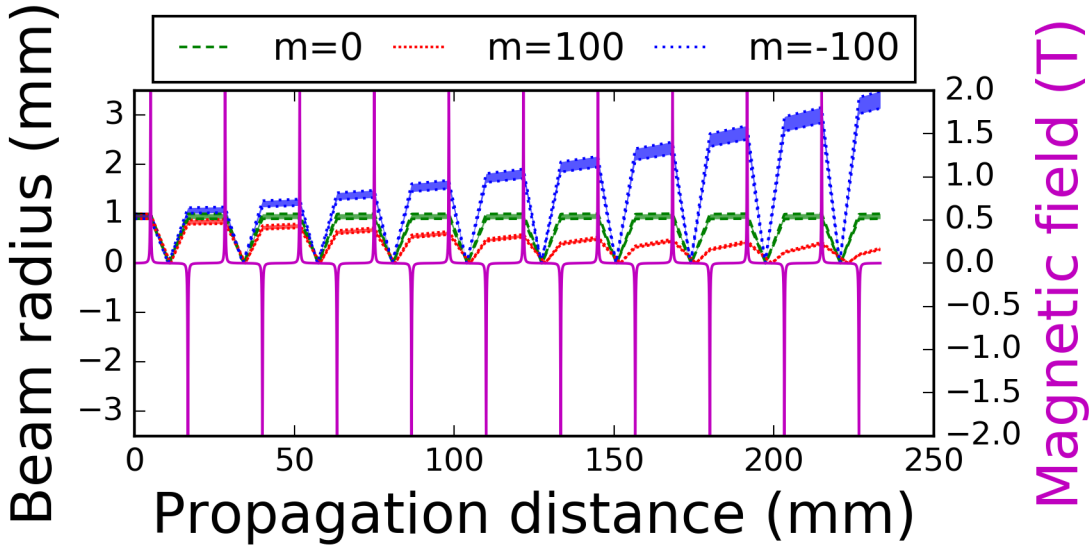

FIGURE 18. Ray trajectories in a set of stacked OAM-dependent lenses
Ray trajectories of $m = -100$ (blue), $m = 0$ (green) and $m = +100$ (red) OAM modes propagating in a set of ten stacked afocal systems (4.13) of Glaser-model lenses (4.59) with longitudinal extent $a = 100$ μm, OAM dispersion length $b = 1$ μm and maximum field strength $B_0 = 2$ T. The magnification of OAM goes exponentially with the number of lens sets.

A completely orthogonal approach to realization of an OAM measurement device of this kind might involve stacking many lenses with a small OAM dispersion coefficient in a manner that magnifies the OAM-dependent effect. We discuss two possible designs for a stacked lens OAM measurement device below: an afocal system with spacing $2f_0$ between lenses with opposite OAM dispersion in Section 4.5, which produces exponentially increasing OAM-dependent magnification with number of lenses, as shown in Figure 18; and a system with variable spacing between the lenses in Section 4.6. Both designs produce strongly OAM-dependent magnification but only weakly OAM-dependent image plane locations.

Device Design 1: Afocal System

If the OAM dispersion coefficient $\Lambda = \frac{2\hbar}{eB_0b^2}$ is small, then the focal length is approximately

$$f_m = f_0 \left(1 + \Lambda m\right) \tag{4.11}$$

If we set two lenses back-to-back with a distance $2f_0$ in between them with opposite OAM dispersion in each ($\Lambda_1 = -|\Lambda|$; $\Lambda_2 = |\Lambda|$) we produce an afocal system with

$$M_m = -\left(1 + 2\Lambda m\right) \tag{4.12}$$

Since an afocal system produces no convergence or divergence–the effective focal length is infinite [128]–any combination of afocal systems is also an afocal system; this afocal system is thus easy to stack. In particular, for a stack of N such afocal systems, in the limit of large N, the total magnification approaches

$$M_m^N = (-1)^N \exp\left(2\Lambda m N\right) \tag{4.13}$$

This set of N afocal systems has one clear advantage: even with arbitrarily small OAM dispersion Λ, we can easily distinguish between any two OAM orders with a sufficiently long stack N.

A twenty-element ($N = 20$) set of identical afocal systems with $a = 10$ μm, $b = 100$ nm, $B_0 = 2$ T and a resultant $f_0 \approx 60$ mm has an OAM dispersion coefficient $|\Lambda| = 0.066$ and a produces a magnification of an $m = +1$, 80 keV electron beam of $|M_{+1}^{20}| = 3.73$; on the other hand, an $m = -1$ beam sees a magnification of $|M_{-1}^{20}| = 0.27$. A superposition of two otherwise-identical $m = +1$ and $m = -1$ modes passed through this device leave with a fourteen-times difference in magnification. The total length of this device is on the order of a couple meters.

Device Design 2: Variable Spacing Between Lenses

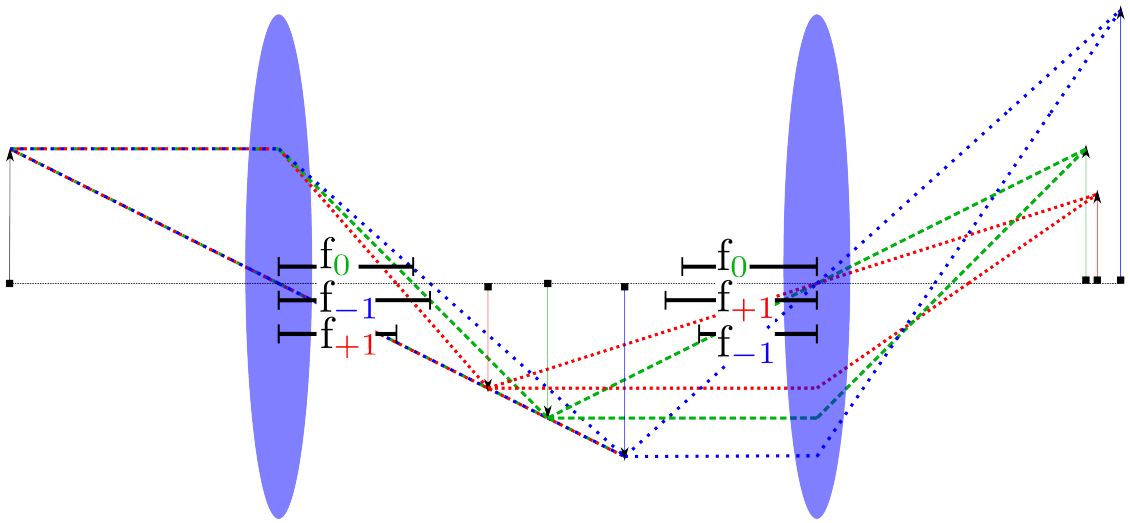

FIGURE 19. Ray diagram of a possible combination of two OAM-dependent lenses Ray diagram for a combination of two lenses (blue disks) with variable spacing in between and opposite OAM dispersion which combine to produce a strongly OAM-dependent magnification, as given by (4.14) and a weakly OAM-dependent image position.

If we place two lenses with opposite OAM dispersion back-to-back with a distance $2\frac{s+1}{s}f_0$ between them, and place an object at a distance $(s+1)f_0$ in front of the first lens, we'll see a focused image at a distance $(s+1)f_0$ behind the second lens with a magnification

$$M_m = \frac{1}{1-2(s+1)\Lambda m} \tag{4.14}$$

The result is similar to that for an afocal system with two major differences: the advantage of this system is that larger magnification is produced by a larger spacing, rather than more lenses; the disadvantage is that only one mode can be fully separated from the rest at a time, as if $2(s+1)\Lambda m \approx 1$ so as to maximize magnification of the m-OAM components of the beam, then $2(s+1)\Lambda(m+1)$ cannot also be close to 1 unless m is very large.

Conclusion

If the measurement device can produce a sufficiently strong OAM-dependent magntification and the initial transverse spread of a state is small, the OAM distribution is mapped onto magnification. The orbital angular momentum spectrum can be quantitatively measured as the radial profile of the probability density after the electron is passed through the device. This OAM measurement is fully quantitative, parallel and effective for inelastically scattered states.

As the orbital angular momentum-dependent lensing effect we study is a non-destructive measurement of OAM, it may also we possible to employ it for preparation of a pure OAM state. Pratical preparation of OAM states inevitably involves small errors in the definition of the correct amplitude and phase for a desired state. These small errors introduce extra OAM states in superposition with the desired state [109]. The combination of a single lens with a strong OAM-dependent lensing effect with a

small aperture placed at the focal point of the desired OAM state is ideally-suited to prepare pure OAM states.

We have demonstrated a Stern-Gerlach-like effect for measurement of electron orbital angular momentum. The measurement technique is applicable to the mixed states produced by inelastic scattering, which are otherwise difficult to measure. We outlined several strategies for practical implementation of this measurement device. If the device can be successfully built and integrated into electron spectrometers, simultaneous measurement of electron energy and orbital angular momentum distributions may be possible.

Supplemental Material for 'Stern-Gerlach-like approach to electron orbital angular momentum measurement'

Tyler Harvey[1], Vincenzo Grillo[2,3], and Benjamin McMorran[1]

[1] Department of Physics, University of Oregon, Eugene, Oregon

[2] CNR-Istituto Nanoscienze, Centro S3, Via G Campi 213/a, I-41125 Modena, Italy

[3] CNR-IMEM Parco Area delle Scienze 37/A, I-43124 Parma, Italy

28 February 2017

Hamiltonian Approach to Magnetic Lensing

How does a standard magnetic round lens work? We shall schematically identify terms in the electron Hamiltonian that cause lensing by inspecting the time evolution operator that results from the Hamiltonian. Although this approach won't get us the focal length of a magnetic lens–we will need to solve the paraxial Schrodinger equation (see Section 4.9) to do that–it will allow us some intiutive insight with regard to lensing behavior.

Standard Lensing Hamiltonian

In order to construct a time evolution operator that causes lensing,

$$U(t) = \exp\left(iHt/\hbar\right) \propto \exp\left(-i\frac{\pi\rho^2}{\lambda f}\right), \tag{4.15}$$

we need a Hamiltionian with a ρ^2 term. The round magnetostatic lenses used most frequently used in electron microscopes can be described by a vector potential

$$\mathbf{A} = \frac{B_0(z)}{2}\rho\hat{\boldsymbol{\phi}}. \tag{4.16}$$

In cartesian coordinates, we see

$$\mathbf{A} = \frac{B_0(z)}{2}\left(x\hat{\mathbf{y}} - y\hat{\mathbf{x}}\right); \tag{4.17}$$

$$\mathbf{A}\cdot\mathbf{p} = \frac{B_0}{2}\left(xp_y - yp_x\right) = \frac{B_0}{2}L_z; \tag{4.18}$$

$$A^2 = \frac{B_0^2(z)\rho^2}{4}; \tag{4.19}$$

which produces a non-relativistic Hamiltonian

$$H = \frac{1}{2m_e}\left(\mathbf{p} + e\mathbf{A}\right)^2 = H_0 + H_{\text{Larmor}} + H_2, \tag{4.20}$$

$$\text{where} \qquad H_0 = \frac{p^2}{2m_e}; \tag{4.21}$$

$$H_{\text{Larmor}} = \frac{eB_0L_z}{2m_e}; \tag{4.22}$$

$$H_2 = \frac{e^2B_0^2(z)}{8m_e}\rho^2; \tag{4.23}$$

where the electron charge $q_e = -e$, H_0 is the free Hamiltonian, H_{Larmor} causes image rotation through a magnetic lens, and H_2 causes lensing.

Full Hamiltonian with OAM-dependent Lensing

Let us now add in a lowest-order radial correction to the vector potential that arises from the finite size of the current source. In the main text, we wrote our model vector potential in Eq. (3) as

$$\mathbf{A} = \left(B_1(z)\frac{\rho}{2} - B_3(z)\frac{\rho^3}{8b^2} + ...O(\rho^5)\right)\hat{\boldsymbol{\phi}}. \tag{4.24}$$

The full non-relativistic Hamiltonian for this vector potential is

$$H = H_0 + H_{\text{Larmor}} + H_2 + H_4 + H_6, \tag{4.25}$$

$$\text{where} \qquad H_0 = \frac{p^2}{2m_e}; \tag{4.26}$$

$$H_{\text{Larmor}} = \frac{eB_1L_z}{2m_e}; \tag{4.27}$$

$$H_2 = \frac{1}{8m_e}\left(e^2B_1^2 - \frac{eB_3L_z}{b^2}\right)\rho^2; \tag{4.28}$$

$$H_4 + H_6 = \frac{e^2}{8m_e}\left(-B_1B_3\frac{\rho^4}{2b^2} + B_3^2\frac{\rho^6}{16b^4}\right); \tag{4.29}$$

where, as in the lowest-order description, H_0 is the free Hamiltonian, H_{Larmor} causes image rotation. H_4 and H_6 are higher-order terms that traditional multipole magnetic corrector elements can cancel without affecting H_2 (see Section 4.12). The term we care about is H_2, which again produces lensing and now has two contributions: the standard magnetic lensing term, $\frac{e^2B_1^2}{8m_e}\rho^2$ [122], and the OAM-dependent term $\frac{eB_3L_z}{8m_eb^2}\rho^2$. Just as the Larmor term can be interpreted either as causing a rotation or an OAM-dependent phase shift, the OAM-depent lensing term could equivalently be interpreted as a radius-dependent rotation. This term is one source of spiral distortion, an aberration that Scherzer documented in 1937 [129].

If higher-order terms $H_4 + H_6$ are corrected (see Section 4.12), the full orbital angular momentum measurement Hamiltonian is

$$H_0 = \frac{p^2}{2m_e} + \frac{eB_1L_z}{2m_e} + \frac{1}{8m_e}\left(e^2B_1^2 - \frac{eB_3L_z}{b^2}\right)\rho^2. \tag{4.30}$$

Calculation of General Thin Lens Focal Length

In this section, we derive an expression for the orbital angular momentum-dependent focal length for a thin magnetostatic lens. One can use the same formalism for the focal length of a thick lens [3]. We use the non-relativistic Schrodinger equation for simplicity; low-order relativistic corrections can easily be added into the result.

$$\nabla^2\psi - \frac{2e}{\hbar i}\mathbf{A}\cdot\boldsymbol{\nabla}\psi + \frac{2m_e}{\hbar^2}\left(eV+E\right)\psi - \frac{e^2}{\hbar^2}A^2\psi = 0, \tag{4.31}$$

where m_e is the rest mass of the electron and $E = eV_a$ is the non-relativistic total energy of the electron accelerated by a voltage V_a. If write ψ in terms of longitudinal and transverse parts of the wavefunction,

$$\psi = \psi_0\chi, \tag{4.32}$$

where

$$\psi_0 = e^{ik_z z}, \tag{4.33}$$

we can quickly simplify our Schrodinger equation with a paraxial approximation. If $k_z \approx k = \frac{\sqrt{2m_eE}}{\hbar}$, we then see that

$$\nabla^2\psi_0 + \frac{2m_e}{\hbar^2}E\psi_0 \approx 0. \tag{4.34}$$

[3]Pozzi [126] elegantly showed that one can calculate electron wavefunction propgation through arbitrarily thick electrostatic or magnetostatic optical elements with an analytical multislice formalism. As the lens effect we're interested in will be practically easiest to implement with a thin lens, we only include the thin lens-approximate calculation. However, we follow Pozzi's notation so that an interested reader could complete the thick lens calculation.

Let us now parse through the terms in the the paraxial Schrodinger equation that results. As

$$\begin{aligned}\nabla^2\psi &= \psi_0\nabla_\perp^2\chi + 2ik_z\psi_0\frac{\partial\chi}{\partial z} - k_z^2\psi_0\chi + \psi_0\frac{\partial^2\chi}{\partial z^2},\\ &\approx \psi_0\nabla_\perp^2\chi + 2ik_z\psi_0\frac{\partial\chi}{\partial z} - k_z^2\psi_0\chi,\end{aligned} \tag{4.35}$$

since $\psi_0\frac{\partial^2\chi}{\partial z^2} \ll k_z^2\psi_0\chi$, we can use (4.34) and divide out ψ_0 to produce the paraxial Schrodinger equation for χ:

$$\nabla_\perp^2\chi + 2ik_z\frac{\partial\chi}{\partial z} - \frac{2e}{i\hbar}\mathbf{A}\cdot\boldsymbol{\nabla}_\perp\chi - \frac{2e}{i\hbar}A_z\left(\frac{\partial\chi}{\partial z} + ik_z\chi\right) + \frac{2m_e e}{\hbar^2}V\chi - \frac{e^2}{\hbar^2}A^2\chi = 0. \tag{4.36}$$

If we first choose

$$A_\phi = B_1(z)\frac{\rho}{2} - B_3(z)\frac{\rho^3}{8b^2}, \tag{4.37}$$

we see that we can cancel the higher-order (ρ^4 and ρ^6) terms in A^2 independently with similar terms in V produced by an electrostatic aberration corrector or A_z produced by a multipolar magnetostatic aberration corrector [4] (see Section 4.12). Let us then solve the Schrodinger equation without these higher-order terms. We will come back to them in Section 4.11. We want to study a propagation of an orbital angular momentum eigenstate,

$$\chi \propto e^{im\phi}. \tag{4.38}$$

[4]Of course, a ρ^4 term in A_z produces a ρ^8 term in A^2, so, as with any multitpolar aberration corrector, we can only push aberrations up to a higher order.

With this eigenstate,

$$\frac{2e}{i\hbar\psi}\mathbf{A}\cdot\boldsymbol{\nabla}\left(\chi\psi\right) = \frac{2e}{i\hbar}A_\phi\frac{1}{\rho}\frac{\partial\chi}{\partial\phi}, \\ = \frac{2e}{\hbar}\frac{A_\phi}{\rho}m\chi. \tag{4.39}$$

If we take a thin lens approximation and drop the small $\nabla_\perp^2\chi$ term [5], this resulting equation is a separable first-order differential equation. The thin lens-paraxial Schrodinger equation with this vector potential, then, is

$$2ik_z\frac{\partial\chi}{\partial z} = \frac{e}{\hbar}\left(B_1(z) - B_3(z)\frac{\rho^2}{4b^2}\right)m\chi + \frac{e^2B_1^2(z)}{4\hbar^2}\rho^2\chi. \tag{4.40}$$

Upon integration, we can identify the transfer function of the lens as

$$\frac{\chi(z\to\infty)}{\chi(z\to-\infty)} = \exp(i\phi_{\text{Larmor}})U_{\text{lens}}, \tag{4.41}$$

$$\text{where} \qquad U_{\text{lens}} = \exp\left(-i\frac{e^2}{8\hbar^2k_z}\int_{-\infty}^{\infty}dz\left[B_1^2(z) - \frac{m\hbar}{eb^2}B_3(z)\right]\rho^2\right), \tag{4.42}$$

$$\text{and where} \qquad \phi_{\text{Larmor}} = -\frac{me}{2\hbar k_z}\int_{-\infty}^{\infty}B_1(z)dz, \tag{4.43}$$

$$= -m\sqrt{\frac{e}{8m_eV_a}}\int_{-\infty}^{\infty}B_1(z)dz. \tag{4.44}$$

[5] In dropping this term, we ignore other orbital angular momentum-dependent effects that are beam radius-dependent and therefore harder to control. In particular, the non-commutation of the Larmor term and p_z^2 produces lensing that is linear with L_z, and the p_ϕ^2 term produces lensing that is parabolic with L_z. These thick-lens orbital angular momentum-dependent effects may be worthy of further study, and are clearer in a Langrangian analysis.

We see, by comparison with (4.15) that

$$\frac{1}{f} = \frac{e^2\lambda}{8\pi\hbar^2 k_z}\int_{-\infty}^{\infty} dz\left[B_1^2(z) - \frac{m\hbar}{eb^2}B_3(z)\right], \tag{4.45}$$

$$= \frac{e^2}{8m_e E}\int_{-\infty}^{\infty} dz\left[B_1^2(z) - \frac{m\hbar}{eb^2}B_3(z)\right], \tag{4.46}$$

$$= \frac{e}{8m_e V_a}\int_{-\infty}^{\infty} dz\left[B_1^2(z) - \frac{m\hbar}{eb^2}B_3(z)\right]. \tag{4.47}$$

We thus showed that we can derive the orbital angular momentum-dependent focal length of a thin lens from the paraxial Schrodinger equation. Let us now calculate the that focal length using some example current sources.

Calculation of Example OAM-dependent Focal Lengths

Loop of Wire

The simplest current source that acts as a round magnetic lens is a single loop of wire in a plane normal to the electron propagation direction. We shall calculate the OAM-dependent focal length of a single loop of wire. First, we need to calculate the vector potential.

For a loop of wire with radius R and current I_0, the vector potential can be calculated as

$$\mathbf{A}(\mathbf{r}) = \frac{\mu_0 I_0 R}{4\pi}\int d\phi' \frac{\hat{\boldsymbol{\phi}}'}{\sqrt{z^2 + R^2 + \rho^2 + 2R\rho\cos(\phi' - \phi)}}. \tag{4.48}$$

For small $\rho \ll R$, we can use only the lowest-order terms in the Taylor series expansion,

$$\mathbf{A}(\mathbf{r}) \approx \frac{\mu_0 I_0 R}{4\pi d(z)} \int d\phi' \hat{\boldsymbol{\phi}}' \left(1 - \frac{1}{2}\frac{\rho^2 + 2R\rho\cos(\phi' - \phi)}{s^2(z)} + \frac{3}{8}\left(\frac{\rho^2 + 2R\rho\cos(\phi' - \phi)}{s^2(z)}\right)^2 - \right.$$
$$\left. - \frac{5}{8}\left(\frac{\rho^2 + 2R\rho\cos(\phi' - \phi)}{s^2(z)}\right)^3 + \ldots\right), \tag{4.49}$$

where $s(z) = \sqrt{z^2 + R^2}$. If we perform the integral over ϕ' and keep terms up to ρ^3, we see

$$\mathbf{A}(\mathbf{r}) = \frac{\mu_0 I_0 R}{4\pi}\left(\frac{\rho R\pi}{s^3(z)} - \frac{3}{2}\frac{\rho^3 R\pi}{s^5(z)} - \frac{15}{4}\frac{\rho^3 R^3\pi}{s^7(z)} + \ldots\right)\hat{\boldsymbol{\phi}}. \tag{4.50}$$

Using the formalism we developed above, let us calculate the focal length of the lensing behavior produced by this term. First, let us define

$$B_0 = \frac{\mu_0 I_0}{2R}; \tag{4.51}$$
$$B_1(z) = \frac{B_0 R^3}{s^3(z)}; \tag{4.52}$$
$$B_3(z) = 6B_0\left(\frac{R^5}{s^5(z)} + \frac{5}{2}\frac{R^7}{s^7(z)}\right); \tag{4.53}$$

such that can write the vector potential as

$$\mathbf{A}(\mathbf{r}) \approx \frac{B_1(z)}{2}\rho - \frac{B_3(z)}{8R^2}\rho^3\hat{\boldsymbol{\phi}}. \tag{4.54}$$

We thus observe that our model vector potential, equation (4.3), is an accurate physical description up to ρ^3. Let us now calculate the focal length of this lens.

We see that, as

$$\int_{-\infty}^{\infty} B_3(z)dz = 24B_0R, \tag{4.55}$$

and as

$$\int_{-\infty}^{\infty} B_1^2(z)dz = \frac{3\pi}{2}B_0^2R, \tag{4.56}$$

we can write the focal length of this lens, using (4.45), as

$$\frac{1}{f_m} = \frac{e^2}{8m_eE}\left(\frac{3\pi}{2}B_0^2R - \frac{m\hbar}{eR^2}\left(24B_0R\right)\right), \tag{4.57}$$

$$f_m = \frac{16m_eE}{3e^2B_0^2R\pi\left(1-\frac{16m\hbar}{eB_0R^2\pi}\right)}. \tag{4.58}$$

Glaser Field

Another simple model for the longitudenal field of a magnetic lens is the Glaser field. Let us compare the OAM dependence of the focal length with a Glaser field model to the focal length we calculated above for a single loop of wire. The Glaser field,

$$B_{\mathrm{G}}(z) = B_0\left(1+\frac{z^2}{a^2}\right)^{-1}, \tag{4.59}$$

has a peak magnetic field B_0 and a longitudinal extent of length a. If we choose $B_1 = B_3 = B_{\mathrm{G}}$ for our focal length calculation, so that the Glasel model field has our lowest-order correction for the finite transverse extent of the field, we see

$$f_m = \frac{16m_eE}{e^2B_0^2a\pi\left(1-\frac{2m\hbar}{eB_0b^2}\right)}. \tag{4.60}$$

We see that this result is indentical in form to the focal length of a loop of wire, (4.58), if the longitudinal extent of the Glaser field is set by the radius of the wire

($a = R$) and the OAM dispersion length is set by the radius ($b = R$). The focal lengths differ only by constant factors.

OAM Lensing and Spherical Aberration

If, instead of dropping terms above ρ^2 in Eq. (4.36), we include up to ρ^4, we can calculate the contribution to the spherical aberration coefficient C_s from the OAM dispersion term. Keeping this term in our thin lens-paraxial Schrodinger equation, we see

$$2ik_z\frac{\partial\chi}{\partial z} = \frac{e}{\hbar}\left(B_1(z) - B_3(z)\frac{\rho^2}{4b^2}\right)m\chi + \frac{e^2B_1^2(z)}{4\hbar^2}\rho^2\chi - \frac{e^2B_1(z)B_3(z)}{8\hbar^2b^2}\rho^4\chi. \quad (4.61)$$

Integrating as in (4.42), our transfer function now includes the term

$$U_{\text{spherical}} = \exp\left(i\frac{e^2}{16\hbar^2k_zb^2}\int_{-\infty}^{\infty}dz\,[B_1(z)B_3(z)]\,\rho^4\right). \quad (4.62)$$

The aberrations of an electron lens are conventionally expanded in terms of the polar angle of incidence at the back focal plane of the lens $\alpha = \arctan\left(\frac{\rho}{f}\right)$ with a transfer function for the lowest-order spherical aberration [130],

$$U_{\text{spherical}} = \exp\left(i\frac{2\pi}{\lambda}\frac{C_3}{4}\alpha^4\right), \quad (4.63)$$

where C_3 is the third-order spherical aberration coefficient. If we rewrite (4.62) in this form with the approximation that $\rho \approx f\alpha$, we can calculate the contribution to C_3.

$$U_{\text{spherical}} = \exp\left(i\frac{2\pi}{\lambda}\frac{e^2}{4\hbar^2k_z^2b^2}\int_{-\infty}^{\infty}dz\,[B_1(z)B_3(z)]\,f^4\frac{\alpha^4}{4}\right). \quad (4.64)$$

By comparison with (4.63), we see with some reorganization that in the thin lens approximation, the contribution to C_3 from the OAM dispersion term we introduced is

$$C_3 = \frac{e^2 f^4}{8 m_e E b^2} \int_{-\infty}^{\infty} dz \left[B_1(z) B_3(z) \right]. \tag{4.65}$$

As the OAM dispersion length b must be small to produce significant orbital dispersion, C_3 could be prohibitively large under standard transmission electron microscope conditions even with independent reduction of C_3 by a multipole corrector (see Section 4.12). Realization of orbital dispersion that is distinguishable over spherical aberration for 80 to 300 keV electrons may demand better aberration correctors than are available today. On the other hand, it may still be possible to distinguish differences between two spectra produced with opposite lens polarities, even with large spherical aberration.

Independent Correction of Aberrations

In this section, we show that a multipole corrector has no A_ϕ component and thus can independently correct aberrations produced by the A^2 term of an OAM measurement device without affecting measurement of OAM.

If we represent an n-pole magnetic lens as a ring of n solenoids of alternating polarity with the solenoid axis oriented radially, we will immediately see that the A_ϕ component of the vector potential would produce a lens with infinite focal length–no lensing effect–in the thin lens approximation.

First, though, we shall write a model for the vector potential of a solenoid oriented along the z axis. As the current of an ideal solenoid is entirely azimuthal

and cylindrically symmetric, we can write this vector potential as

$$\mathbf{A}_{\text{ax}} = A_0(z, \rho)\hat{\boldsymbol{\phi}}. \tag{4.66}$$

If we now rotate this vector potential to point along the x axis, we see

$$\mathbf{A}_{\text{rad}} = A_0(x, \sqrt{y^2 + z^2}) \left(\frac{-z}{\sqrt{y^2 + z^2}} \hat{\mathbf{y}} + \frac{y}{\sqrt{y^2 + z^2}} \hat{\mathbf{z}} \right). \tag{4.67}$$

Lastly, if we define a set of rotated coordinates (x_m, y_m) defined by a rotation angle $\theta_m = \frac{2\pi m}{n}$ where

$$x_m = x\cos(\theta_m + y\sin(\theta_m), \tag{4.68}$$

$$y_m = y\cos(\theta_m) - x\sin(\theta_m), \tag{4.69}$$

we can now easily write the vector potential of this lens in terms of a sum of solenoidal vector potentials in the rotated coordinates.

$$\mathbf{A}_{n-\text{pole}} = \sum_{m=0}^{n-1} A_0(x_m, \sqrt{y_m^2 + z^2}) \left(\frac{-z}{\sqrt{y_m^2 + z^2}} \hat{\mathbf{y}}_m + \frac{y_m}{\sqrt{y_m^2 + z^2}} \hat{\mathbf{z}} \right). \tag{4.70}$$

We can immediately see that the $\hat{\mathbf{y}}_m$ component, which includes a non-zero $\hat{\boldsymbol{\phi}}$ term, is odd in z and thus integrates to zero under a calculation of the focal length in the thin lens approximation.

$$\int_{-\infty}^{\infty} dz\ \mathbf{A}_{n-\text{pole}} \cdot \hat{\boldsymbol{\phi}} = 0 \qquad \Rightarrow \qquad f_{m_{n-\text{pole}}} = \infty. \tag{4.71}$$

Therefore, a multipolar magnetostatic aberration corrector element has a vanishingly small orbital angular momentum lensing effect, and can safely be used

to independently correct higher-order aberrations produced by a round lens without affecting the orbital angular momentum dispersion of that round lens.

Efficient Sorting of Free Electron Orbital Angular Momentum

Benjamin McMorran[1], Tyler Harvey[1], and Martin Lavery[2]

[1] Department of Physics, University of Oregon, Eugene, Oregon

[2] School of Engineering, University of Glasgow, Glasgow G12 8QQ, Scotland, UK

27 February 2017

Introduction to the OAM Sorter

Electrons scattered by an interaction with matter, such as from individual atoms, molecules, or materials, acquire a spectrum of energies, linear momenta, and spin polarizations. Information about the event is encoded in these various degrees of freedom by the electron's wavefunction. Recently, several groups demonstrated control of the orbital angular momentum (OAM) of freedom of free electrons [11, 12, 13]. Myriad techniques for generating electron OAM states now exist, including material and magnetic spiral phase plates [11, 17, 18, 19], phase [14, 15, 16] and amplitude [12, 77] diffraction gratings, and mode conversion [108]. Exchange of OAM between a target specimen and a fast electron could provide information about the structural chirality [27, 34] and out-of-plane magnetization of the target [24, 25, 131]. In these applications, the electrons can scatter to many different final orbital angular momentum states, and measurement of the final orbital angular momentum distribution can provide new information about the scattering targets. However, there are currently no measurement techniques that can efficiently and quantitatively measure the orbital angular momentum distribution of free electrons.

In 2010, Berkhout *et al.* [107] demonstrated a new method to efficiently sort OAM states of light using four refractive optical elements. The apparatus transforms

an azimuthal phase at the input into a linear phase at the output, such that OAM components at the input are mapped into separate linear momentum states at the output. This ability to measure superpositions and mixed states of optical OAM enables parallel orbital angular momentum measurement. The apparatus has been rapidly employed for a range of optical applications in both fundamental research [132, 133], quantum information [134], and communications [135, 136]. As shown in Fig. 20a, the apparatus is based on two custom-made non-spherical refractive optical components, the phase unwrapper U and the phase corrector C, with two lenses L1 and L2 used to the Fourier transform the output of each.

The first optical element (U and L1 in Fig. 20) is a log-polar transformer [137] that transforms a set of concentric rings at the input plane into a set of parallel lines at the back focal plane of the lens–or, equivalently, orbital angular momentum states into planar waves. The phase profile of this unwrapper element is described by Eq. 1 in [107]:

$$\varphi_{\mathrm{U}}(x,y) = \frac{1}{\Delta t}\left[y \arctan\left(\frac{y}{x}\right) - x \ln\left(\frac{\sqrt{x^2+y^2}}{b}\right) + x\right], \tag{4.72}$$

where Δt is a lengthscale that sets the separation distance between orbital angular momentum states in the output plane, and b is a lengthscale that determines the position of the unwrapped beam in the corrector plane. A plot of the phase distribution for this lens is shown in Fig. 21a.

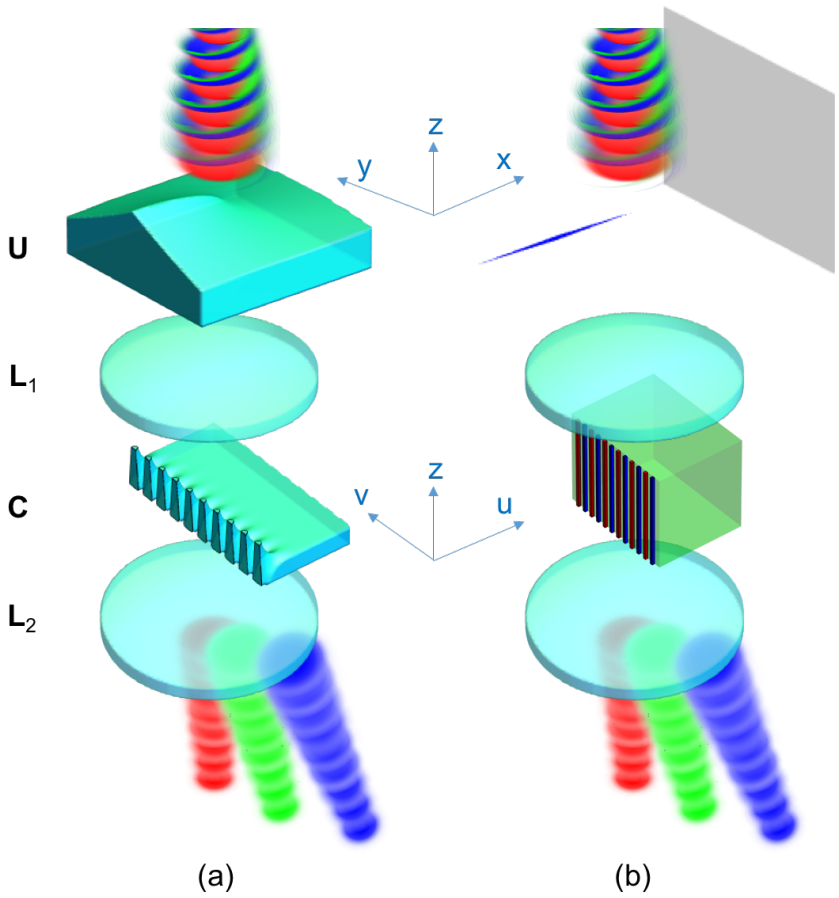

FIGURE 20. Schematic comparison of photon and electron OAM sorters
Schematic of the optical arrangement of OAM-sorting devices for (a) light and (b) electrons. Different OAM states are shown in different colors. Mixed OAM states are incident on the top of both systems, each of which consists of four elements. A phase unwrapper element U in the front focal plane of a lens L1 is followed by a phase corrector element C in the back focal place of L1. For electrons, the proposed element U is a charged needle or knife edge, and the corrector element C is an array of electrodes with alternating bias. Immediately after the corrector element C, different OAM components are separated in momentum space. At the bottom of each device, a Fourier-transforming lens L2 separates OAM components into different spots in real space at the output.

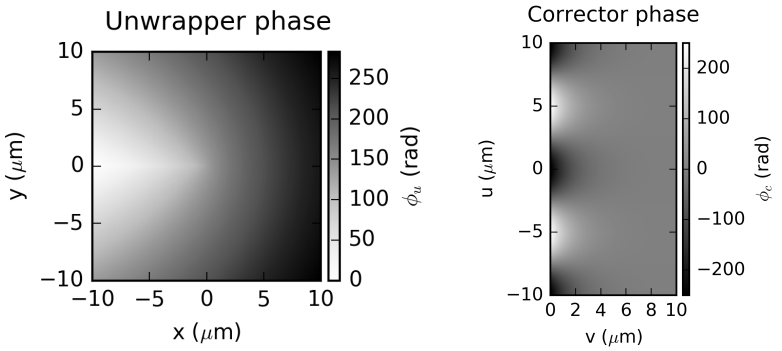

(a) (b)

FIGURE 21. Phases necessary for sorter elements
Phase profiles of the (a) unwrapper element U described in Equation 4.72 and (b) the corrector element C described in Equation 4.75. In (a), the lowest phase (white) occurs at the position of the needle. Both plots use parameters expressed in Table 3.

Electrostatic OAM Unwrapper for Electrons

To imprint the phase profile described in Eq. 4.72 onto an electron wavefunction, one could use either refractive or diffractive wavefront-shaping techniques. In light optics, there are established methods for fabricating custom phase plates out of transparent material such as glass. However, while thin film phase plates for electrons are possible [17], they contaminate easily and are difficult to fabricate. Finally, no material is sufficiently electron-transparent to imprint the large phases required for sorting OAM. Arbitrary electron phase profiles can be imprinted holographically using nanofabricated diffractive optics [14, 15]. However, the smaller but still significant inelastic scattering in the material, the small diffraction angles, low diffraction efficiency, and finite size of the diffractive structures make the use of such holograms for an OAM mode sorter impractical.

Instead, a relatively simple electrostatic phase plate consisting of a charged needle and a conductive plate can be used to imprint a phase equivalent to Eq. 4.72 onto

a charged particle wave. The phase that the tip of a charged needle imparts to an electron has been studied previously by several different groups [138, 139, 140]. Matteucci *et al.* [138] calculated this analytically by first considering the electrostatic potential $V(\mathbf{r})$ around an infinitesimally thin wire of finite length and uniform charge density placed a distance h away from a flat conducting plate. The spatially varying phase shift a potential $V(\mathbf{r})$ imparts to an electron plane wave of energy E and relativistically-corrected wavelength λ traveling in the $+z$ direction can be calculated by the integral

$$\varphi(\mathbf{r}) = C_E \int_{-\infty}^{\infty} V(\mathbf{r}) dz, . \tag{4.73}$$

where C_E is a constant that depends only on the energy of the beam [141] ($C_E = 6.53$ mrad V^{-1} nm^{-1} for 300 keV electrons).

In 4.19, we adapt Matteucci *et al.*'s result (Equation 4 in [138]) for the purpose of imprinting Eq. 4.72. We show that if the electron beam is localized around the needle tip nearest the plate electrode, and the length of the needle and its separation from the plate are sufficiently large, this arrangement imprints the appropriate unwrapping phase for sorting electron OAM:

$$\varphi_{\mathrm{U}}(x, y) = \frac{QC_E}{4\pi\epsilon_0 L} \left[y \arctan\left(\frac{y}{x}\right) - x \ln\left(\frac{\sqrt{x^2+y^2}}{L}\right) \right] + \varphi_0, \tag{4.74}$$

where L is the length of the needle, E is the kinetic energy of the electron beam, and φ_0 is a uniform phase common to all paths, which is unobservable at the detector. With the exception of a missing linear phase, we see that Eq. 4.74 exactly matches Eq. 4.72 if $b = L$ and $\frac{Q}{L} = \frac{4\pi\epsilon_0}{C_E \Delta t}$. This discrepancy is unimportant, as a linear phase in the unwrapper plane corresponds to a position offset in the corrector plane that can

be easily provided by position alignment optics (based on static in-plane magnetic or electric fields) found in the transmission electron microscope.

There are several possible methods for practical realization of such an electrostatic element in an electron microscope, as discussed further in 4.20. A thin insulating wire could provide the constant line charge density assumed for the derivation of Eq. 4.72, although in an actual device the charge density could be affected by the incident beam current and could fluctuate in time. On the other hand, a conducting wire fabricated such that its physical surface coincides with the equipotential surface of a constant line charge may be more easily tunable and more robust against changes in the incident beam current. In 4.20, we use simulations to demonstrate that such needles can impart the appropriate unwrapper phase modulation with excellent fidelity, and we find that this is insensitive to electrostatic boundary conditions. The inner conductive surfaces of an electron microscope are typically grounded and are hundreds of microns to millimeters away from the electron beam, and in such limits these surfaces will have little effect on the phase imparted by the needle.

When using the proposed device to measure OAM distributions of electrons scattered from a specimen in a TEM, it is important to realize that these orbital states will originate from different locations in the sample. For example, electron orbital states could be generated by scattering from each atom in a material, and so the electron vortices will have different centers each offset from one another. This results in a complicated distribution in the near field of the specimen. To ensure all of these offset orbital states are aligned with the input of the proposed OAM sorter, the input of the sorter should be positioned in the far-field of the specimen where the orbital mode distribution will be spatially coherent and all electron vortices will

be concentric. For actual experiments, the needle-based phase unwrapper should therefore be placed in the back focal plane of the sample. A modified aperture holder provides a convenient way to install, position, and electrically bias the needle-based corrector. Such holders have already been developed for a variety of TEMs in order to control charged Möllendstedt biprism wires for use in electron holography.

We also note that an extended knife edge electrode could potentially be used instead of a charged needle. The 2D electrostatic potential of a semi-infinite plane of charge with it's edge along the z-axis has the same functional form as the desired unwrapper phase $\varphi_{\mathrm{U}}(x, y)$ (see Chapter 7 in [142]). Thus, a knife-edge electrode aligned along the optical axis could provide an alternative design to the needle, if the length were long enough such that phase introduced near the beginning and end of the electrode were negligible.

Electrostatic Phase Corrector for Electrons

The phase unwrapper element is followed by a conventional electron lens system (L1). Simulations of the electron wave function in the back focal plane of this intermediate lens show that there are large variations in the phase due to the unwrapping operation. These phase variations must be removed by a second optical element to reveal the subtler OAM-dependent differences. This phase corrector (labelled "C" in Fig. 20) is described by the following phase profile:

$$\varphi_{\mathrm{C}}(u, v) = \frac{b}{\Delta t} \exp\left(-\frac{2\pi u}{d}\right) \cos\left(-\frac{2\pi v}{d}\right), \tag{4.75}$$

where, following the notation of Berkhout et al. [107], we use (u, v) to describe the transverse coordinates of the transformed field in the corrector plane from the transverse coordinates of the input field. This corrector phase, shown in Fig. 21b,

is identical to the phase derived by Berkhout *et al.* [107], using some re-labeled variables. To accurately correct the phase in this plane, the amplitude of this phase modulation must be proportional to $\frac{b}{\Delta t}$, and the lengthscale $d = \frac{\lambda f}{\Delta t}$, where f is the focal length of lens L1 between the unwrapper and corrector planes.

Electrostatic elements can also be employed to imprint this corrector phase. As the phase distribution is a solution to Laplace's equation in 2D, i.e. $\nabla^2 \varphi_{\mathrm{C}}(u, v) = 0$, we see that an electrostatic potential in 2D can take this form. We can approximate the 2D potential solution in 3D with a potential that varies slowly in z. Specifically, we can apply $\varphi_{\mathrm{C}}(u, v)$ to an electron with a set of alternating electrodes, as shown in Fig. 22b. As long as the longitudinal height D of the electrodes is much longer than the period d (see4.21), and the thin grating condition, $\lambda D \ll d^2$ is satisfied, the variation of the potential in the longitudinal direction is negligible over the depth. The corrector phase can be written as

$$\varphi_{\mathrm{C}}(u, v) = C_E D V_{\mathrm{C}_0} \exp\left(\frac{-2\pi u}{d}\right) \cos\left(\frac{-2\pi v}{d}\right). \tag{4.76}$$

We see that we get the appropriate φ_{C} (Eq. 4.75) if $C_E D V_{\mathrm{C}_0} = \frac{bd}{\lambda f}$ and $V_{\mathrm{C}_1} = V_{\mathrm{C}_0} \exp\left(-\frac{2\pi u_1}{d}\right)$. Further analysis (see 4.21) shows that it could be practical to remove the reference electrodes at $u = u_1$ if the nearest grounded surface is sufficiently far away (at some distance much larger than d).

As shown in Figure 23b, and 23e, immediately after the corrector the phase of the electron beam is flattened, such that an input state with orbital angular momentum quantum number m is transformed here into a bar-shaped distribution with a phase that linearly varies in the v-direction from 0 to $2\pi m$ over the width of the beam profile. The slope of this corrected phase ramp is inversely proportional to the width of the beam profile in the v-direction, equal to Δt. Thus, after the Fourier-transforming

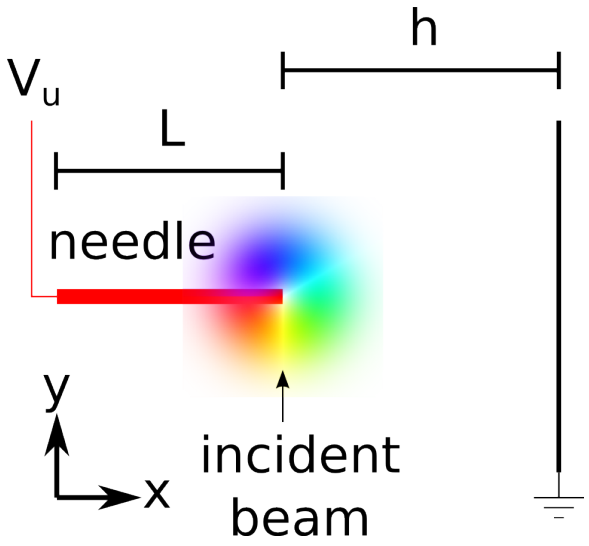

(a)

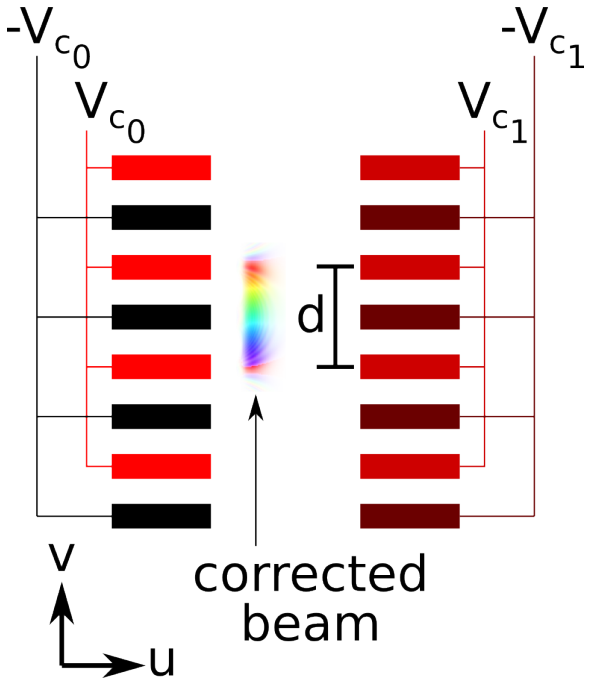

(b)

FIGURE 22. Cartoon depicting both electrostatic sorter elements
(a) Top-view cartoon of charged needle and ground plate used to produce the unwrapper phase. Electrons passing into the device near the right end of the needle will acquire the phase described by Eq. 4.74. (b) Top-view cartoon of example electrodes that could be used to produce the corrector phase, 4.75. Alternating very high (V_{C_0}) and very low ($-V_{C_0}$) voltages at the boundary at $u = 0$ produce a sinusoidal potential in the v-direction. Alternating weakly high (V_{C_1}) and weakly low ($-V_{C_1}$) voltages at the boundary at $u = u_1$ produce an exponential decay in the u-direction. The electrodes at $u = u_1$ aren't physically necessary, as we show in Fig. 29b

lens L2, the initial orbital modes are focused at the output plane into separate lines (Fig. 23) with a final spacing of

$$\Delta t = \frac{\lambda f}{d}. \tag{4.77}$$

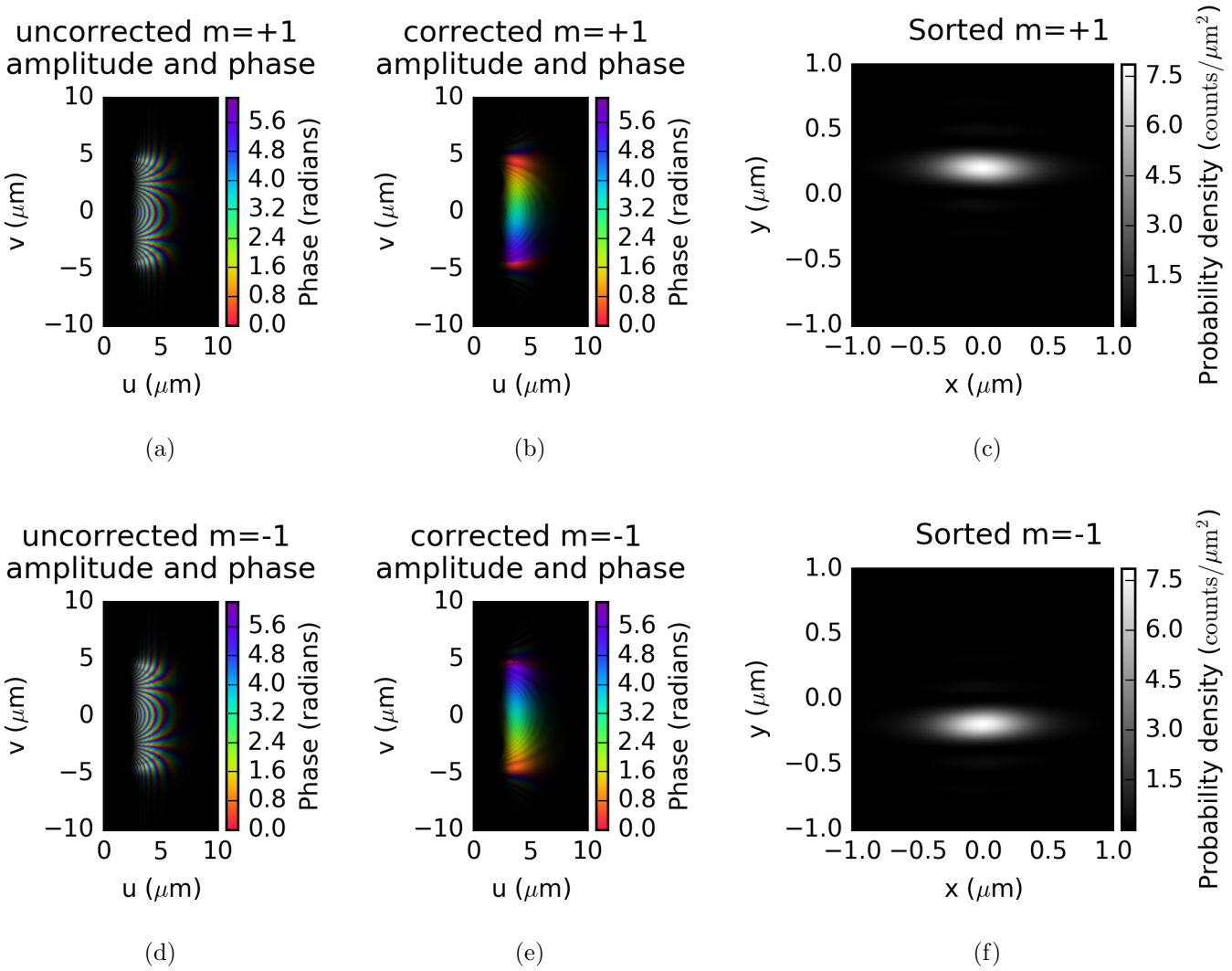

FIGURE 23. Illustration of sorted OAM states

Illustration of the action of the device. The unwrapper U and intermediate lens L1 produces a beam in the corrector plane that has width d in the v-direction and that has rapid phase variations (a,d). The corrector C removes the rapid phase variations to produce plane wave-like beams in the corrector plane (b,e) which correspond to deflected spots in the output plane (c,f). These simulations assume ideal unwrapper and corrector phases (Eqs. 4.74 and 4.76) with parameters shown in Table 3.

Design Parameters and Simulated Outputs

Lavery *et al.* separated orbital angular momentum states of light with a wavelength of $\lambda = 632.8$ nm, lens focal length $f = 300$ mm, a corrector period $d = 8$ mm and therefore an unmagnified separation of $\Delta t = 23.73$ μm [132]. As preparation of a collimated photon orbital angular momentum state with a waist on the order of 10 μm is straightforward, this separation is sufficient.

The orders of magnitude of these parameters are wildly different for electrons, but good separation is similarly straightforward. One set of possible parameter values to achieve this is listed in Table 3. With a needle length of $L \sim 50$ μm, an incident beam waist on the order of 1 μm is physically reasonable. Separation on the order of $\Delta t = 0.2$ μm can be achieved in a transmission electron microscope at 300 kV with $\lambda \sim 1.97$ pm and a corrector period of $d \sim 10$ μm if the focal length of the lens between the needle and corrector, L1, is $f \sim 100$ cm. Several lenses with focal lengths in the 1 cm to 10 cm range can be combined to more practically produce a 1 meter focal length over a much shorter distance.

TABLE 3. Exemplary parameters for the sorter

Sorter Parameter	Magnitude
λ	1.97 pm
f	1 m
d	10 μm
$b = L$	50 μm
$V_{C_0} D$	39 V $\cdot$ μm
Q/L	8.5 pC/m
V_U	0.63 V

To review, the parameters of this arrangement are: (a) the charge Q added to the needle-based unwrapper phase plate, (b) the length of the needle L, (c) the voltage V_{C_0} applied to the corrector electrodes, (d) the spatial periodicity d of the corrector

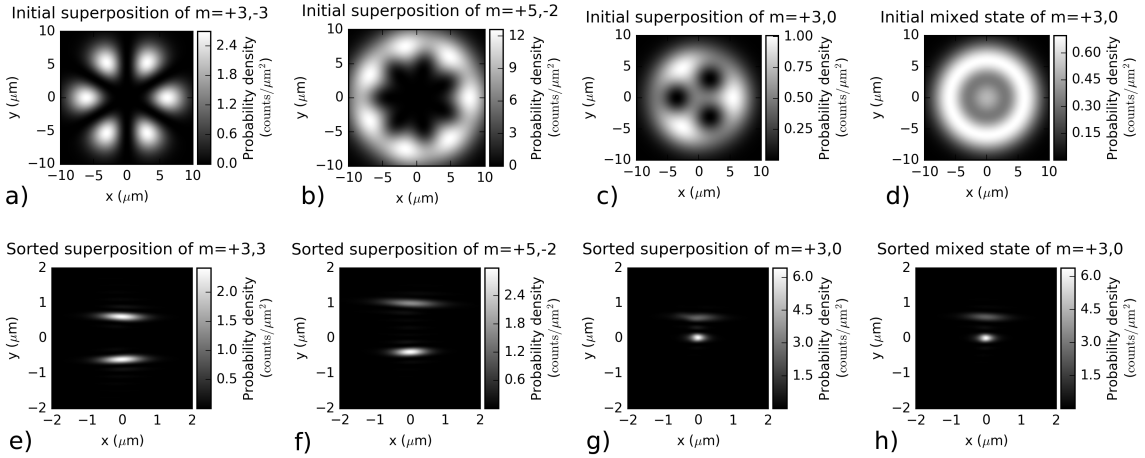

FIGURE 24. Sorted mixes and superpositions of OAM states
The simulated (a,b,c,d) input and (e,f,g,h) output of the proposed electron OAM sorter using parameters shown in Table 3. Input states are Laguerre-Gaussian modes with a 5 μm beam waist and (a) superposed $m = +3$ and $m = -3$, (b) superposed $m = +5$ and $m = -2$, (c) superposed $m = 3$ and $m = 0$, and (d) mixed $m = +3$ and $m = 0$. Each electron OAM component at the input gets mapped onto a separate region in space at the output, which is viewed directly using TEM imaging optics. In this way, a spectrum of electron OAM states can be efficiently recorded in parallel.

electrodes, and (e) the focal length of the lenses f. We have offered one possible combination of parameters here, but this may of course be tuned according to the application.

Figures 23, 24, and 25 show the action of a sorter with these parameters on various input states. Note that, just as with an optical OAM sorter, the electron device sorts multiple input OAM states identically regardless of whether they are in coherent superpositions (Fig. 24(c) and 24(g)) or incoherent mixtures (Fig. 24(f) and 24(h)). As shown in the simulation in Fig. 25, the electron OAM sorter could also be used for orbital mode decomposition of arbitrary wavefunctions, which could be used to reveal hidden chiral asymmetries in electron-scattering targets.

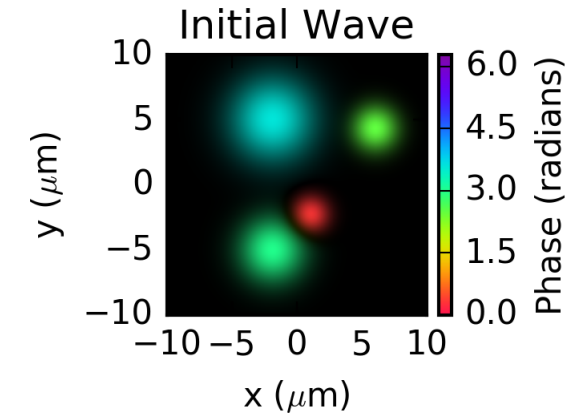

(a)

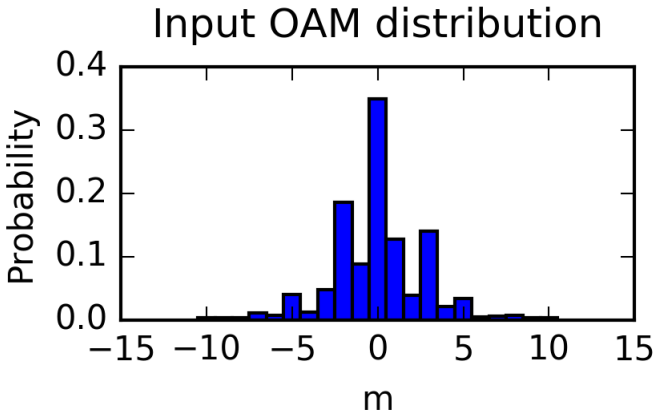

(b)

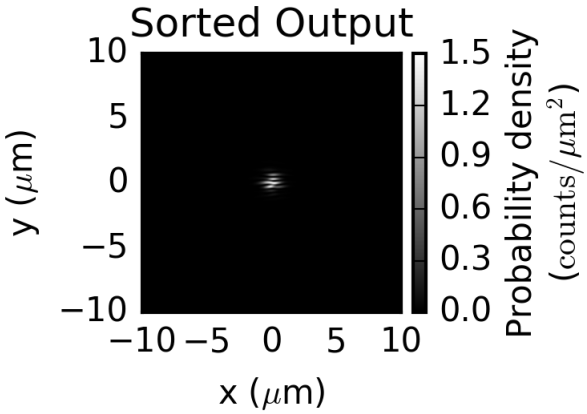

(c)

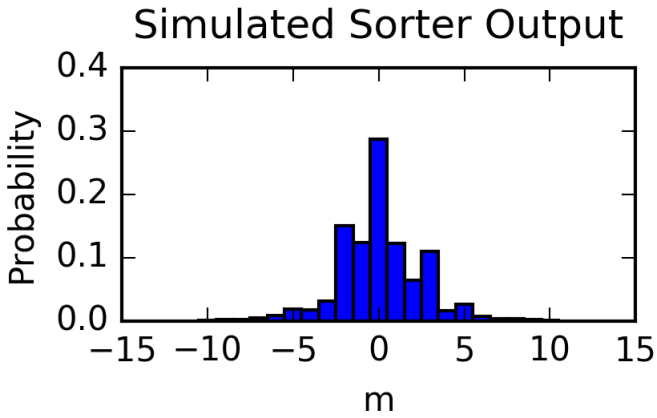

(d)

FIGURE 25. Sorted random globs

(a) Initial random wavefunction with non-trivial orbital angular momentum distribution; amplitude is shown as brightness and phase is shown as hue; (b) calculated orbital angular angular momentum distribution; (c) probability density of the random wavefunction passed through the sorter; (d) orbital angular momentum distribution calculated by binning the output of the sorter.

Crosstalk

An important figure of merit for a measurement device is the crosstalk: the rate of erroneous counts that occur when adjacent measurement outcomes are counted as the outcome of interest. In the proposed electron OAM sorter, there will be some crosstalk that arises from the diffraction limit. Input electron orbital modes separated by a single OAM quanta ($\Delta m = 1$) become plane waves just after the corrector element that are just slightly tilted from one another, with phase ramps that only differ by 2π across the width of the states. Thus, when focused onto an imaging detector by lens L2, these two states are only just resolvable. Figure 26 shows the crosstalk of an ideal electron orbital angular momentum sorter, simulated with phases shown in Eqs. 4.74 and 4.76 and parameters shown in Table 3. In a real device, aberrations and misalignment of the electron beam are likely to further increase this minimum amount of crosstalk.

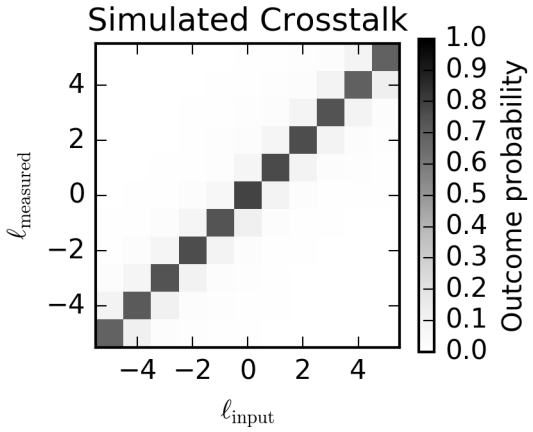

(a)

FIGURE 26. Crosstalk of the sorter
Crosstalk of the electron orbital angular momentum measurement with parameters shown in Table 3. A perfect sorter would have outcome probabilities of exactly 1 for every $\ell_{\text{measured}} = \ell_{\text{input}}$ and 0 elsewhere. As with an optical OAM mode sorter, the crosstalk of this device is due to diffraction limit.

Conclusion

Knowledge of interactions in which a free electron exchanges OAM with a specimen can lead to insights into the properties of the object. However, many attempts by several groups to observe OAM transfer between a prepared focused electron with OAM and an atom have so far been unsuccessful, due to the fact that electrons are scattered into a superposition of orbital states. Here we described an electron-optical analog of the OAM sorter developed for photons. This device can non-destructively disperse the spectrum of electron OAM, providing a way to measure the OAM distribution of electrons scattered or ejected from atoms, molecules, and larger collections of matter. Thus, this could provide a completely new form of spectroscopy that can be used to probe the asymmetric structure of matter, atomic and molecular polarizations, and chiral interactions.

Calculation of Phase Past Charged Needle

Here we consider electrons propagating in the z direction past an infinitesimally thin needle of constant charge density $\sigma = Q/L$, where L is the length of the needle. We consider that the needle lies on the x-axis with one tip at the origin and the other located at $x = -L$. The charged needle is oriented perpendicularly to a conducting plate that lies parallel to the $y - z$ plane at $x = h$. The electrostatic potential of this arrangement can be written as

$$V(\mathbf{r}) = \frac{Q}{4\pi\epsilon_0 L} \ln \left[\left(\frac{x+L+\sqrt{(x+L)^2+y^2+z^2}}{x+\sqrt{x^2+y^2+z^2}} \right) \times \left(\frac{x-2h-L+\sqrt{(x-2h-L)^2+y^2+z^2}}{x-2h+\sqrt{(x-2h)^2+y^2+z^2}} \right) \right] \tag{4.78}$$

Following [138], we use Eq. 4.73 to calculate the phase an electron plane wave acquires as it propagates through this potential:

$$\begin{aligned}\varphi_{\mathrm{U}}(\mathbf{r}) = \; & -\tfrac{QC_E}{4\pi\epsilon_0 L}\Bigg[|y|\sin^{-1}\left(\tfrac{-x-L}{\sqrt{(x+L)^2+y^2}}\right) - |y|\sin^{-1}\left(\tfrac{-x}{\sqrt{x^2+y^2}}\right) \\ & +|y|\sin^{-1}\left(\tfrac{-x+2h+L}{\sqrt{(x-2h-L)^2+y^2}}\right) - |y|\sin^{-1}\left(\tfrac{-x+2h}{\sqrt{y^2+(x-2h)^2}}\right) \\ & -x\ln\left(\tfrac{\sqrt{(x+L)^2+y^2}}{\sqrt{x^2+y^2}}\right) - x\ln\left(\tfrac{\sqrt{(x-2h-L)^2+y^2}}{\sqrt{(x-2h)^2+y^2}}\right) \\ & -L\ln\left(\tfrac{\sqrt{(x+L)^2+y^2}}{\sqrt{(x-2h-L)^2+y^2}}\right) + 2h\ln\left(\tfrac{\sqrt{(x-2h-L)^2+y^2}}{\sqrt{(x-2h)^2+y^2}}\right)\Bigg]. \end{aligned} \tag{4.79}$$

We consider a situation in which the incident electron beam is confined only to the region immediately adjacent to the tip of the needle nearest to the plate. If we take the distance h between the needle and the plate to be much larger than the region of interest, i.e. $h \gg \sqrt{x^2+y^2}$, we see some simplification. The third and fourth terms cancel, the sixth term goes to zero, and the last two terms go to a constant phase shift that depends only on L and h. Depending on the relative magnitudes of h and L, it is also possible to extract a linear phase in x from the latter three terms.

$$\begin{aligned}\varphi_{\mathrm{U}}(\mathbf{r}) = \; & -\tfrac{QC_E}{4\pi\epsilon_0 L}\Bigg[|y|\sin^{-1}\left(\tfrac{-x-L}{\sqrt{(x+L)^2+y^2}}\right) - |y|\sin^{-1}\left(\tfrac{-x}{\sqrt{x^2+y^2}}\right) \\ & -x\ln\left(\tfrac{\sqrt{(x+L)^2+y^2}}{\sqrt{x^2+y^2}}\right)\Bigg] + \varphi_0, \end{aligned} \tag{4.80}$$

where φ_0 is a constant "background" phase that does not affect the sorter mechanism.

If we rewrite the inverse trigonometric functions, we see that the extra $|y|\frac{\pi}{2}$ terms cancel and we have

$$\varphi_{\mathrm{U}}(\mathbf{r}) = -\frac{QC_E}{4\pi\epsilon_0 L}\Bigg[\quad |y|\cos^{-1}\left(\frac{x+L}{\sqrt{(x+L)^2+y^2}}\right) - |y|\cos^{-1}\left(\frac{x}{\sqrt{x^2+y^2}}\right) \\ -x\ln\left(\frac{\sqrt{(x+L)^2+y^2}}{\sqrt{x^2+y^2}}\right)\Bigg] + \varphi_0, \tag{4.81}$$

If we now take the length of the needle as large compared to the region of interest, i.e. $L \gg \sqrt{x^2+y^2}$, we see further simplification of the result. As $\cos^{-1}(1) = 0$, we're left with two terms. With this approximation, the phase distribution induced onto an electron wave passing close to the tip of the needle is:

$$\varphi_{\mathrm{U}}(\mathbf{r}) = \quad -\frac{QC_E}{4\pi\epsilon_0 L}\left[-|y|\cos^{-1}\left(\frac{x}{\sqrt{x^2+y^2}}\right) + x\ln\left(\frac{\sqrt{x^2+y^2}}{L}\right)\right] + \varphi_0, \tag{4.82}$$

which we can finally rewrite, using the fact that $\cos^{-1}\frac{x}{\sqrt{x^2+y^2}} = \tan^{-1}\frac{|y|}{x}$, as

$$\varphi_{\mathrm{U}}(\mathbf{r}) = \quad \frac{QC_E}{4\pi\epsilon_0 L}\left[y\tan^{-1}\left(\frac{y}{x}\right) - x\ln\left(\frac{\sqrt{x^2+y^2}}{L}\right)\right] + \varphi_0. \tag{4.83}$$

Eq. 4.83 is exactly the desired phase of the unwrapper element (Eq. 4.72) minus a linear phase. The missing linear phase corresponds to a position shift in the output plane that can be easily corrected with readily available magnetostatic or electrostatic position alignment optics.

Fidelity of the Phase of Proposed Unwrapper Element

It is well established that a thin, biased conducting needle does not maintain a constant line charge density [143, 144]. Experiments have shown that a thin, insulating needle aquires a negative charge under the incident electron beam [20], and it's possible that the charge density on such an insulating needle is nearly constant. However, it seems that the value of the charge density, and therefore the parameters of the sorter, might depend more strongly on the incident beam current than is desirable for a robust, tunable device.

A more controllable approach involves the use of a biased conductor with a physical surface fabricated to match the equipotential surfaces of a constant line charge density [143]. In particular, to produce a potential that corresponds to a line charge density Q/L and a length of the line charge L, the needle should be held at a voltage V_{U} with a surface defined by the equipotential

$$V_{\mathrm{U}} = \frac{Q}{4\pi\epsilon_0 L} \ln\left(\frac{x + L + \sqrt{(x+L)^2 + y^2 + z^2}}{x + \sqrt{x^2 + y^2 + z^2}}\right) \tag{4.84}$$

which corresponds to Eq. 4.78 in the limit that $h \to \infty$.

We simulated the potential produced by the nearly-hyperboloid tip described above, with a conducting surface at the equipotential $V_{\mathrm{U}} = 8\frac{Q}{4\pi\epsilon_0 L}$. As Eq. 4.78 is a solution to Laplace's equation, i.e. $\nabla^2 V(x, y, z) = 0$, everywhere except at the position of the needle, we numerically solved Laplace's equation with a Dirichlet boundary given by Eq. 4.84. We tried several boundary conditions for the external boundaries to test the robustness of the potential against variations in the shape and location of the grounded conductor. The results of these simulations are shown in Fig. 27. The phases calculated with Eq. 4.73 from simulated potentials show

excellent agreement with the ideal unwrapper phase, Eq. 4.83, regardless of boundary conditions, and especially as the distance h to the conducting plate is increased. When h is smaller (e.g. Fig. 27c), a noticeable astigmatic $y^2 - x^2$ phase is noticeable. This deviation is correctable using standard quadrupolar stigmators.

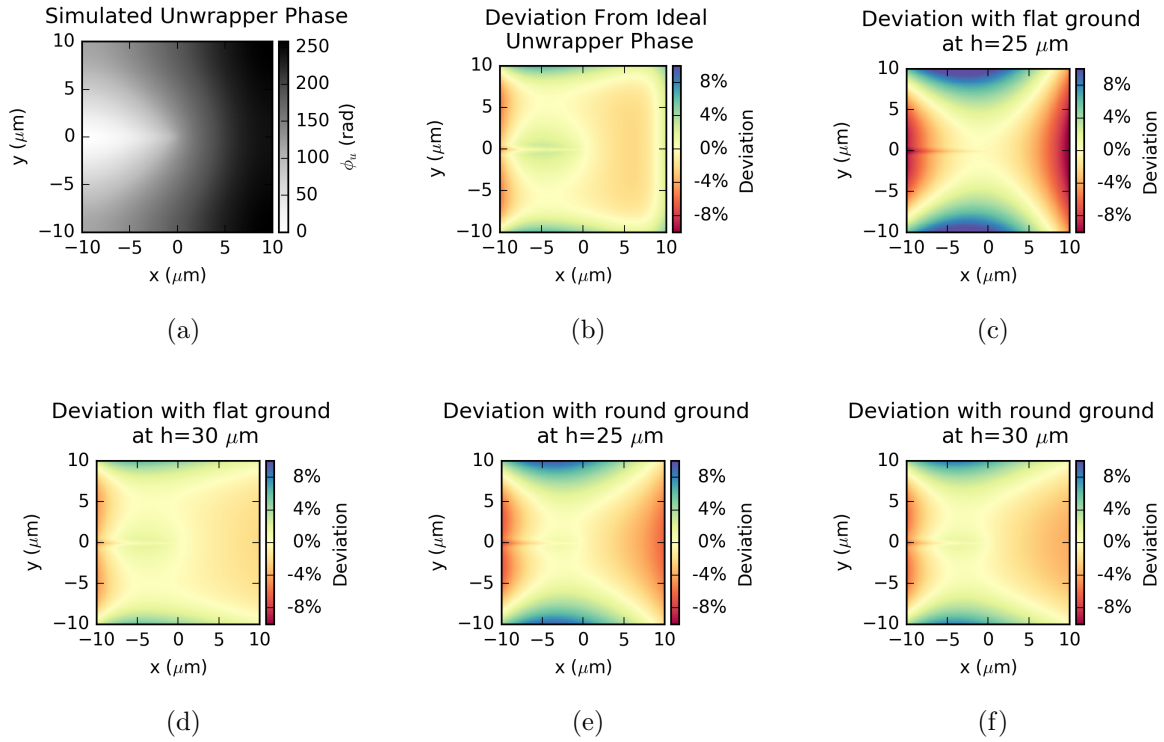

FIGURE 27. Simulation showing possible errors with electrostatic needle transformer Simulations of the electron phase effects of a shaped conducting needle with physical surfaces defined to match equipotentials of a constant line charge density, with various boundary conditions. The electrostatic potential was calculated around a needle of length $L = 50$ μm with various boundary conditions, and the phase imparted to the electron was calculated after traversing the region from $x = -10$ μm to $x = +10$ μm, $y = -10$ μm to $y = +10$ μm, and $z = -40$ μm to $z = +40$ μm. The von Neumann boundary condition $\boldsymbol{\nabla} V \cdot \hat{\mathbf{n}} = 0$ was used for all boundaries. (a) Phase distribution imprinted by the needle on an electron wave passing through the simulated region. (b) Deviation of the phase shown in (a) from an ideal unwrapper phase described by Eq. 4.72. Deviation is defined as the difference between the simulated phase and the ideal phase, divided by the difference between the maximum and minimum ideal phase in the 20 μm x 20 μm region shown. (c) Deviation of a phase calculated from a simulation box with a flat ground plate (Dirichlet boundary) at $x = +25$ μm. (d) Deviation of a phase calculated from a simulation box with a flat ground plate at $x = +30$ μm. (e) Deviation of a phase calculated from a simulation box with a semi-cylindrical ground plate at a radius of $+25$ μm from the end of the needle. (e) Deviation of a phase calculated from a simulation box with a semi-cylindrical ground plate at a radius of $+30$ μm from the end of the needle.

Fidelity of the Phase of Proposed Corrector Element

As the corrector phase solves Laplace's equation, it is straightforward to generate this phase with an electrostatic potential $V(u, v)$, following Eq. 4.73. We can approximate the two-dimensional solution to Laplace's equation $V(u, v)$ with a nearly-z-independent three-dimensional solution. The simplest boundary conditions are constant over a range in z that we'll call the depth, D. In particular, we can specify the $V(u, v)$ we want with boundaries at $u = 0$ and $u = u_1$. In other words,

$$V(u_i, v, z) = \begin{cases} V(u_i, v) & |z| \leq \frac{D}{2} \\ \text{free} & \text{elsewhere} \end{cases} \tag{4.85}$$

We investigated these boundaries with a numerical solution to Laplace's equation. For Figures 28 and 29a, we set Dirichlet boundary conditions at two positions in u. In the range $|z| < \frac{D}{2}$, we set the Dirichlet boundary conditions

$$V(u = 0, v) \quad = V_{\mathrm{C}_0} \cos\left(-\tfrac{2\pi v}{d}\right) \tag{4.86}$$

$$V(u = u_0, v) \quad = V_{\mathrm{C}_1} \cos\left(-\tfrac{2\pi v}{d}\right), \tag{4.87}$$

where V_{C_0} and V_{C_1} are the peak potentials at $u = u_0 = 0$ and $u = u_1$, respectively, and d is the period in v. We see that, to satisfy Laplace's equation, we must have $V_{\mathrm{C}_1} = V_{\mathrm{C}_0} \exp\left(-\frac{2\pi u_1}{d}\right)$. We used periodic boundary conditions in v, and the von Neumann boundary condition $\boldsymbol{\nabla} V \cdot \hat{\mathbf{n}} = 0$ for all other boundaries. For Figure 29b, we used a more physical approximation to the above: we used Dirichlet boundary conditions with constant potentials along $u = 0$ only inside square, flat electrodes, and used the von Neumann boundary condition at $u = 0.8d$.

We found that, as long as the depth D was much larger than the period d, i.e. the potential is constant in z over a much longer length scale than it varies in u and v, the fringing fields were insignificant. Specifically, we found that the potential decayed exponentially with a decay length $\frac{d}{2\pi}$ outside the device. The contribution of this tail to the phase scales with d, while the contribution from inside the device scales with D. The precision of the phase can therefore be arbitrarily increased by increasing D while holding d constant, up to the limit of the thin grating condition $\lambda D \ll d^2$. As $\lambda = 1.97$ pm for 300 keV electrons, if $d = 10$ μm, the device would still act as a thin grating up to $D \sim 100$ m.

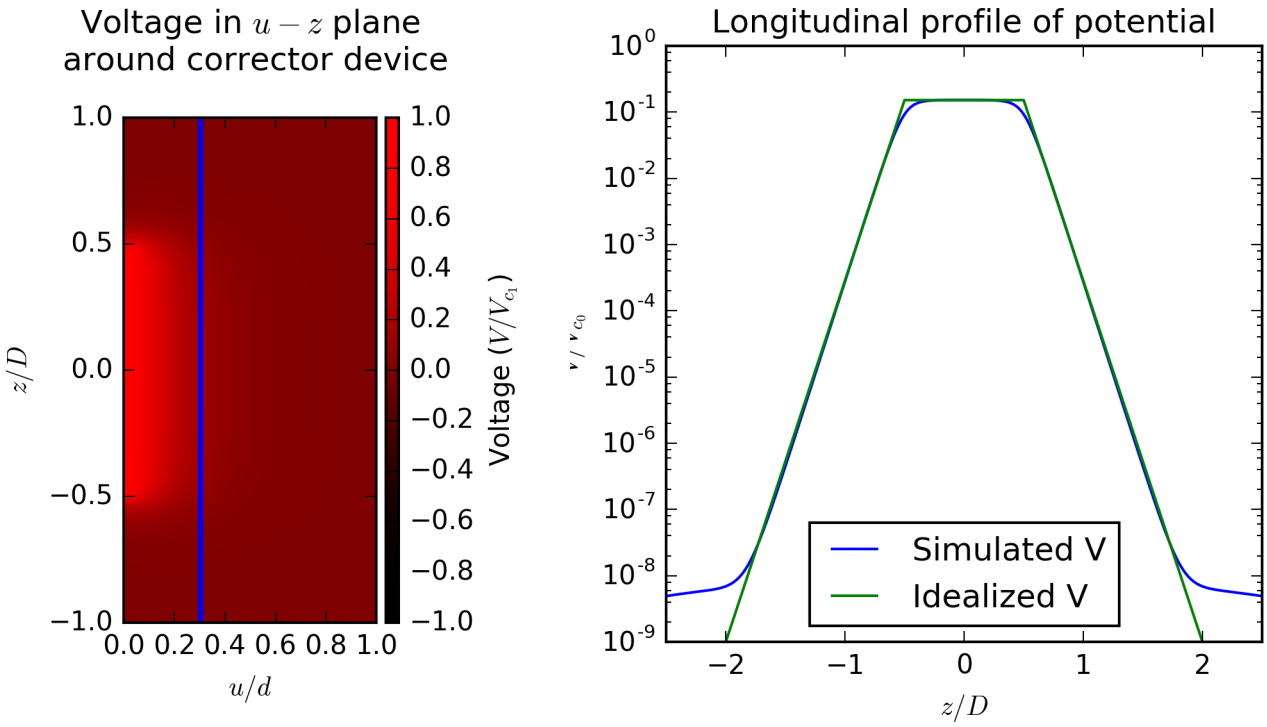

(a) (b)

FIGURE 28. Simulations showing ideal behavior of electrostatic corrector
(a) Cross-section of simulated potential in the u-z plane at $v = 0$ showing rapid decay of potential outside the device.
(b) Line plot of a simulated potential at $u = 0.3d$ in the u-z plane showing exponential decay of the potential outside the device. (blue) Simulated potential $V(u = 0.3d, v = 0, z)$, also shown as blue line in (a); (green) Model of the potential that is constant inside the device and exponentially decays as $V \propto \exp\left(\pm\frac{2\pi(z\pm D/2)}{d}\right)$ outside the device.
This simulation used a period $d = 1.0$, a depth $D = 2.0$ (resulting in boundaries at $z = \pm 1.0$), arbitary V_{C_0}, and boundaries at $u = 0$, $u = 1.0$, $v = 0$, $v = 1.0$, $z = -50.0$ and $z = 50.0$ with a voxel size of 0.01 by 2^{-5} by 0.01.

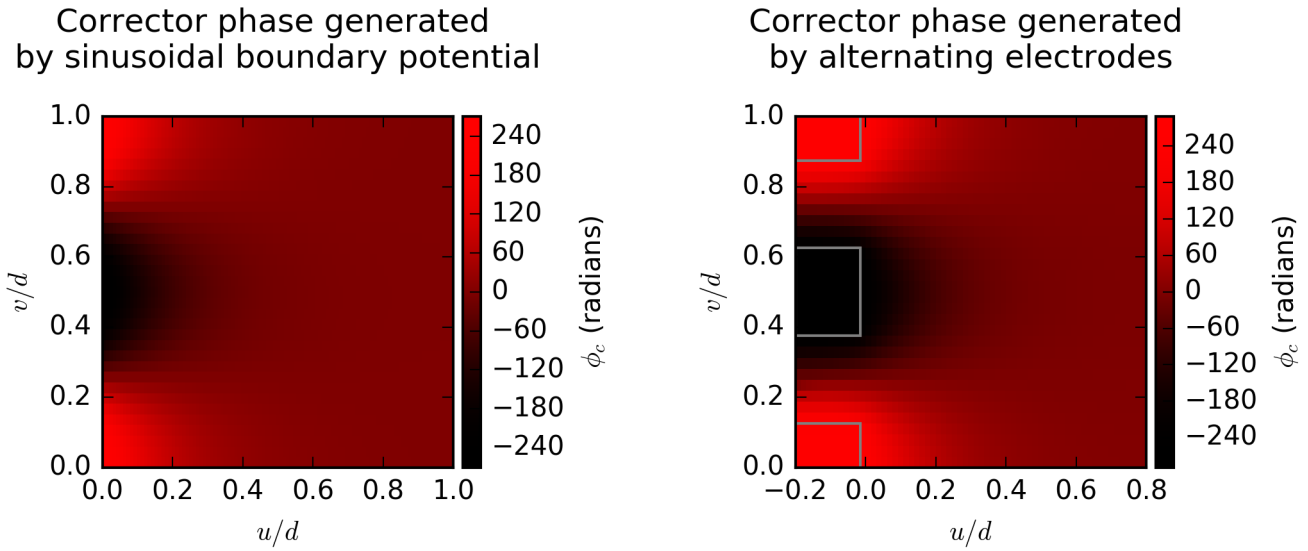

(a) (b)

FIGURE 29. Simulated corrector phases under ideal and realistic conditions Corrector phase calculated by simulating the potential with two different sets of boundary conditions. (a) Phase calculated with potential set by a sinusoidally-varying potential along $u = 0$ and along $u = d$. (b) Phase calculated with flat, constant-voltage electrodes (grey outlines) at $u = 0$ and von Neumann boundary conditions at $u = 0.8d$. Both produce sufficiently accurate corrector phases.

Chapter Conclusion

In this chapter, we proposed two techniques for postselection of electron orbital angular momentum states: with electrostatic transformations in two conjugate planes, and with small orbital aberrations in magnetic lenses. Both methods are in principle effective measurements even for the entangled electron-specimen states that result from inelastic interaction. Development of one or both of these techniques will allow a far wider range of application of electron orbital angular momentum.

CHAPTER V

CONCLUSION AND FUTURE POSSIBILITIES

We demonstrated a set of tools associated with the control of electron orbital angular momentum: efficient preparation of orbital angular momentum states with diffraction gratings, interaction of electron states with specimen states to probe structural chirality and magnetic fields, and measurement of final electron states with either electrostatic elements in conjugate planes or orbital aberrations of magnetic lenses.

The prospects are good for application of electron orbital angular momentum to the study of materials. In particular, if we can develop measurement tools that match in quality our tools to prepare electron OAM, a wide range of applications will become much easier to realize. We may be able to routinely visualize the orbitals of an atom or crystal [145], identify the handedness and structure of a biomolecule with a small electron dose [27, 34, 146], or quickly characterize the symmetry of a crystal or plasmon mode [31, 146].

In addition to future applications, some more basic questions remain. Is it possible to use light to efficiently and controllably prepare electrons into orbital angular momentum states? Is there a unified description of the interaction of electron spin and angular momentum with the longitudinal and transverse components of a magnetic field? Can measurement of the orbital angular momentum of photoemitted or field-emitted electrons reveal more about a material? Does the field or photoemission from a chiral-structured material show any 'orbital polarization'? The future for study of questions related to electron orbital angular momentum is promising.

REFERENCES CITED

[1] L. Allen, M. W. Beijersbergen, R. J. C. Spreeuw, and J. P. Woerdman. Orbital angular momentum of light and the transformation of laguerre-gaussian laser modes. *Physical Review A*, 45(11):8185, June 1992.

[2] S. Fürhapter, A. Jesacher, S. Bernet, and M. Ritsch-Marte. Spiral interferometry. *Optics Letters*, 30(15):1953, 2005.

[3] S. Fürhapter, Alexander Jesacher, Stefan Bernet, and Monika Ritsch-Marte. Spiral phase contrast imaging in microscopy. *Optics Express*, 13(3):689–694, February 2005.

[4] Monika Ritsch-Marte. Orbital angular momentum light in microscopy. *Phil. Trans. R. Soc. A*, 375(2087), February 2017.

[5] Gregory Foo, David M. Palacios, and Jr. Swartzlander. Optical vortex coronagraph. *Optics Letters*, 30(24):3308, December 2005.

[6] Jian Wang, Jeng-Yuan Yang, Irfan M. Fazal, Nisar Ahmed, Yan Yan, Hao Huang, Yongxiong Ren, Yang Yue, Samuel Dolinar, Moshe Tur, and Alan E. Willner. Terabit free-space data transmission employing orbital angular momentum multiplexing. *Nature Photonics*, 6(7):488–496, July 2012.

[7] Nenad Bozinovic, Yang Yue, Yongxiong Ren, Moshe Tur, Poul Kristensen, Hao Huang, Alan E. Willner, and Siddharth Ramachandran. Terabit-Scale Orbital Angular Momentum Mode Division Multiplexing in Fibers. *Science*, 340(6140), June 2013.

[8] H. He, M. E. J. Friese, N. R. Heckenberg, and H. Rubinsztein-Dunlop. Direct Observation of Transfer of Angular Momentum to Absorptive Particles from a Laser Beam with a Phase Singularity. *Physical Review Letters*, 75(5):826, July 1995.

[9] K. T. Gahagan and Jr. Swartzlander. Optical vortex trapping of particles. *Optics Letters*, 21(11):827–829, June 1996.

[10] David G. Grier. A revolution in optical manipulation. *Nature*, 424(6950):810, 2003.

[11] Masaya Uchida and Akira Tonomura. Generation of electron beams carrying orbital angular momentum. *Nature*, 464(7289):737, April 2010.

[12] J. Verbeeck, H. Tian, and P. Schattschneider. Production and application of electron vortex beams. *Nature*, 467(7313):301, 2010.

[13] Benjamin J. McMorran, Amit Agrawal, Ian M. Anderson, Andrew A. Herzing, Henri J. Lezec, Jabez J. McClelland, and John Unguris. Electron Vortex Beams with High Quanta of Orbital Angular Momentum. *Science*, 331(6014):192 –195, January 2011.

[14] Tyler R. Harvey, Jordan S. Pierce, Amit K. Agrawal, Peter Ercius, Martin Linck, and Benjamin J. McMorran. Efficient diffractive phase optics for electrons. *New Journal of Physics*, 16(9):093039, September 2014.

[15] Vincenzo Grillo, Gian Carlo Gazzadi, Ebrahim Karimi, Erfan Mafakheri, Robert W. Boyd, and Stefano Frabboni. Highly efficient electron vortex beams generated by nanofabricated phase holograms. *Applied Physics Letters*, 104(4):043109, January 2014.

[16] Roy Shiloh, Yossi Lereah, Yigal Lilach, and Ady Arie. Sculpturing the electron wave function using nanoscale phase masks. *Ultramicroscopy*, 144:26–31, September 2014.

[17] A. Béché, R. Winkler, H. Plank, F. Hofer, and J. Verbeeck. Focused electron beam induced deposition as a tool to create electron vortices. *Micron*, 80:34–38, January 2016.

[18] Armand Béché, Ruben Van Boxem, Gustaaf Van Tendeloo, and Jo Verbeeck. Magnetic monopole field exposed by electrons. *Nature Physics*, 10(1):26–29, January 2014.

[19] A. M. Blackburn and J. C. Loudon. Vortex beam production and contrast enhancement from a magnetic spiral phase plate. *Ultramicroscopy*, 136:127–143, January 2014.

[20] Arthur M. Blackburn. Observation of an Electron Vortex Beam Created from a Self-Charging Rod. *Microscopy and Microanalysis*, 22(S3):1710–1711, July 2016.

[21] Giulio Pozzi, Peng-Han Lu, Amir H. Tavabi, Martial Duchamp, and Rafal E. Dunin-Borkowski. Generation of electron vortex beams using line charges via the electrostatic Aharonov-Bohm effect. *Ultramicroscopy*, 2017.

[22] Vincenzo Grillo, Ebrahim Karimi, Gian Carlo Gazzadi, Stefano Frabboni, Mark R. Dennis, and Robert W. Boyd. Generation of Nondiffracting Electron Bessel Beams. *Physical Review X*, 4(1):011013, January 2014.

[23] Igor P. Ivanov. Measuring the phase of the scattering amplitude with vortex beams. *Physical Review D*, 85(7):076001, April 2012.

[24] Sophia Lloyd, Mohamed Babiker, and Jun Yuan. Quantized Orbital Angular Momentum Transfer and Magnetic Dichroism in the Interaction of Electron Vortices with Matter. *Physical Review Letters*, 108(7):074802, February 2012.

[25] P. Schattschneider, B. Schaffer, I. Ennen, and J. Verbeeck. Mapping spin-polarized transitions with atomic resolution. *Physical Review B*, 85(13):134422, April 2012.

[26] Ján Rusz and Somnath Bhowmick. Boundaries for Efficient Use of Electron Vortex Beams to Measure Magnetic Properties. *Physical Review Letters*, 111(10):105504, September 2013.

[27] A. Asenjo-Garcia and F. J. García de Abajo. Dichroism in the Interaction between Vortex Electron Beams, Plasmons, and Molecules. *Physical Review Letters*, 113(6):066102, August 2014.

[28] Ján Rusz, Somnath Bhowmick, Mattias Eriksson, and Nikolaj Karlsson. Scattering of electron vortex beams on a magnetic crystal: Towards atomic-resolution magnetic measurements. *Physical Review B*, 89(13):134428, April 2014.

[29] D. Seipt, A. Surzhykov, and S. Fritzsche. Structured x-ray beams from twisted electrons by inverse Compton scattering of laser light. *Physical Review A*, 90(1):012118, July 2014.

[30] S. J. Ward and J. H. Macek. Effect of a vortex in the triply differential cross section for electron-impact K-shell ionization of carbon. *Physical Review A*, 90(6):062709, December 2014.

[31] M. Schüler, J. Berakdar, and Y. Pavlyukh. Disentangling multipole contributions to collective excitations in fullerenes. *Physical Review A*, 92(2):021403, August 2015.

[32] Jo Verbeeck, He Tian, and Gustaaf Van Tendeloo. How to Manipulate Nanoparticles with an Electron Beam? *Advanced Materials*, 25(8):1114–1117, 2013.

[33] Roeland Juchtmans, Armand Béché, Artem Abakumov, Maria Batuk, and Jo Verbeeck. Using electron vortex beams to determine chirality of crystals in transmission electron microscopy. *Physical Review B*, 91(9):094112, March 2015.

[34] Tyler R. Harvey, Jordan S. Pierce, Jordan J. Chess, and Benjamin J. McMorran. Demonstration of electron helical dichroism as a local probe of chirality. *arXiv:1507.01810*, July 2015.

[35] Konstantin Y. Bliokh, Peter Schattschneider, Jo Verbeeck, and Franco Nori. Electron vortex beams in a magnetic field: A new twist on Landau levels and Aharonov-Bohm states. *arXiv:1204.2780*, April 2012.

[36] Giulio Guzzinati, Peter Schattschneider, Konstantin Y. Bliokh, Franco Nori, and Jo Verbeeck. Observation of the Larmor and Gouy Rotations with Electron Vortex Beams. *Physical Review Letters*, 110(9):093601, February 2013.

[37] P. Schattschneider, Th Schachinger, M. Stöger-Pollach, S. Löffler, A. Steiger-Thirsfeld, K. Y. Bliokh, and Franco Nori. Imaging the dynamics of free-electron Landau states. *Nature Communications*, 5, August 2014.

[38] Vincenzo Grillo, Tyler Harvey, Jordan Pierce, Federico Venturi, Roberto Balboni, Gian Carlo Gazzadi, Stefano Frabboni, Benjamin McMorran, Robert Boyd, and Ebrahim Karimi. The measurement of off-plane magnetic field through electron vortex beams. In European Microscopy Society, editor, *European Microscopy Congress 2016: Proceedings*. Wiley-VCH Verlag GmbH & Co. KGaA, Weinheim, Germany, December 2016.

[39] L. Clark, A. Béché, G. Guzzinati, and J. Verbeeck. Quantitative measurement of orbital angular momentum in electron microscopy. *Physical Review A*, 89(5):053818, May 2014.

[40] Giulio Guzzinati, Laura Clark, Armand Béché, and Jo Verbeeck. Measuring the orbital angular momentum of electron beams. *Physical Review A*, 89(2):025803, February 2014.

[41] Roy Shiloh, Yuval Tsur, Roei Remez, Yossi Lereah, Boris A. Malomed, Vladlen Shvedov, Cyril Hnatovsky, Wieslaw Krolikowski, and Ady Arie. Unveiling the Orbital Angular Momentum and Acceleration of Electron Beams. *Physical Review Letters*, 114(9):096102, March 2015.

[42] T. Yahn, J.S. Pierce, T.R. Harvey, and B.J. McMorran. Addition, Subtraction, and Analysis of Orbital Angular Momentum in Electron Vortex Beams. *Microscopy and Microanalysis*, 19(Supplement S2):1166–1167, 2013.

[43] Koh Saitoh, Yuya Hasegawa, Kazuma Hirakawa, Nobuo Tanaka, and Masaya Uchida. Measuring the Orbital Angular Momentum of Electron Vortex Beams Using a Forked Grating. *Physical Review Letters*, 111(7):074801, August 2013.

[44] Mariia Shutova, Alexandra A. Zhdanova, and Alexei V. Sokolov. Detection of mixed OAM states via vortex breakup. *Physics Letters A*, 381(4):408–412, January 2017.

[45] Nobuo Tanaka. Present status and future prospects of spherical aberration corrected TEM/STEM for study of nanomaterials. *Science and Technology of Advanced Materials*, 9(1):014111, 2008.

[46] Knut W. Urban. Studying atomic structures by aberration-corrected transmission electron microscopy. *Science*, 321(5888):506–510, 2008.

[47] S. J. Pennycook, M. F. Chisholm, A. R. Lupini, M. Varela, A. Y. Borisevich, M. P. Oxley, W. D. Luo, K. van Benthem, S.-H. Oh, D. L. Sales, S. I. Molina, J. Garca-Barriocanal, C. Leon, J. Santamara, S. N. Rashkeev, and S. T. Pantelides. Aberration-corrected scanning transmission electron microscopy: from atomic imaging and analysis to solving energy problems. *Philosophical Transactions of the Royal Society A: Mathematical, Physical and Engineering Sciences*, 367(1903):3709–3733, 2009.

[48] O.L. Krivanek, N. Dellby, and A.R. Lupini. Towards sub-a electron beams. *Ultramicroscopy*, 78:1–11, 1999.

[49] Heiko Müller, Stephan Uhlemann, Peter Hartel, and Maximilian Haider. Advancing the hexapole cs-corrector for the scanning transmission electron microscope. *Microscopy and Microanalysis*, 12(06):442–455, 2006.

[50] Benjamin McMorran. United states patent: 8680488 - system and method for producing and using multiple electron beams with quantized orbital angular momentum in an electron microscope, 2014.

[51] Jo Verbeeck, Giulio Guzzinati, Laura Clark, Roeland Juchtmans, Ruben Van Boxem, He Tian, Armand Bch, Axel Lubk, and Gustaaf Van Tendeloo. Shaping electron beams for the generation of innovative measurements in the (S)TEM. *Comptes Rendus Physique*, 15(23):190–199, February 2014.

[52] Masaya Uchida and Akira Tonomura. Generation of electron beams carrying orbital angular momentum. *Nature*, 464:737–739, 2010.

[53] J. Verbeeck, H. Tian, and P. Schattschneider. Production and application of electron vortex beams. *Nature*, 467:301–304, 2010.

[54] Benjamin J. Mcmorran, Amit Argawal, Ian M. Anderson, Andrew A. Herzing, Henri J. Lezec, Jabez J. McClelland, and John Unguris. Electron vortex beams with high quanta of orbital angular momentum. *Science*, 331:192–195, 2012.

[55] Juan C. Idrobo and Stephen J. Pennycook. Vortex beams for atomic resolution dichroism. *Journal of Electron Microscopy*, 60(5):295–300, 2011.

[56] Koh Saitoh, Yuya Hasegawa, Nobu Tanaka, and Masaya Uchida. Production of electron vortex beams carrying large orbital angular momentum using spiral zone plates. *Journal of Electron Microscopy*, 61(3):171–177, 2012.

[57] J. Verbeeck, H. Tian, and A. Béché. A new way of producing electron vortex probes for stem. *Ultramicroscopy*, 113:83–87, 2012.

[58] A. M. Blackburn and J. C. Loudon. Vortex beam production and contrast enhancement from a magnetic spiral phase plate. *Ultramicroscopy*, 136:127–143, 2013.

[59] A. Béché, R van Boxem, G. van Tendeloo, and J. Verbeeck. Magnetic monopole field exposed by electrons. *Nature Physics*, 10:26–29, 2013.

[60] Robert Collier. *Optical Holography*. Elsevier, June 2013.

[61] P. Schattschneider, S. Rubino, C. Hebert, J. Rusz, J. Kunes, P. Novak, E. Carlino, M. Fabrizioli, G. Panaccione, and G. Rossi. Detection of magnetic circular dichroism using a transmission electron microscope. *Nature*, 441:486–488, 2006.

[62] Benjamin J. McMorran. *Electron Diffraction and Interferometry Using Nanostructures*. Ph. d. dissertation, University of Arizona, University of Arizona, Tucson, AZ, January 2009.

[63] J.S. Pierce, T.R. Harvey, T.S. Yahn, and B.J. McMorran. High efficiency electron diffractive optics. *Microscopy and Microanalysis*, 19(Supplement S2):1188–1189, 2013.

[64] Vincenzo Grillo, Gian Carlo Gazzadi, Ebrahim Karimi, Erfan Mafakheri, Robert W. Boyd, and Stefano Frabboni. Highly efficient electron vortex beams generated by nanofabricated phase holograms. *Applied Physics Letters*, 104(4):043109, 2014.

[65] R. Magnusson and T. K. Gaylord. Diffraction efficiencies of thin phase gratings with arbitrary grating shape. *Journal of the Optical Society of America*, 68(6):806–809, 1978.

[66] Tyler R. Harvey, Gii Brougher, Kurt Langworthy, and Benjamin J. McMorran. Small-pitch electron diffraction holograms patterned on inorganic resist with electron beam lithography. Poster presented at EIPBN 2013, May 2013.

[67] Edgar Völkl, Lawrence F. Allard, and David C. Joy. *Introduction to Electron Holography*. Springer, 1999.

[68] Ampere A. Tseng. Recent developments in micromilling using focused ion beam technology. *Journal of Micromechanics and Microengineering*, 14(4):R15, 2004.

[69] S. Cruz-Arreola and O. Mata-Mendez. Diffraction of beams by infinite or finite amplitude-phase gratings. *Revista mexicana de fsica*, 57(1):6–16, February 2011.

[70] P. W. Hawkes and E. Kasper. *Principles of Electron Optics: Wave Optics*, volume 3. Academic Press, London, 1994.

[71] NIST digital library of mathematical functions. http://dlmf.nist.gov/20. Release 1.0.8 of 2014-04-24.

[72] Claude Cohen-Tannoudji, Jacques Dupont-Roc, and Gilbert Grynberg. *Atom-Photon Interactions: Basic Processes and Applications*. Wiley, March 1998.

[73] Iwo Bialynicki-Birula and Zofia Bialynicka-Birula. Beams of electromagnetic radiation carrying angular momentum: The RiemannSilberstein vector and the classicalquantum correspondence. *Optics Communications*, 264(2):342–351, August 2006.

[74] Jonathan Handali, Pratistha Shakya, and Brett Barwick. Creating electron vortex beams with light. *Optics Express*, 23(4):5236, February 2015.

[75] Brett Barwick, David J. Flannigan, and Ahmed H. Zewail. Photon-induced near-field electron microscopy. *Nature*, 462(7275):902–906, December 2009.

[76] Armin Feist, Katharina E. Echternkamp, Jakob Schauss, Sergey V. Yalunin, Sascha Schäfer, and Claus Ropers. Quantum coherent optical phase modulation in an ultrafast transmission electron microscope. *Nature*, 521(7551):200–203, May 2015.

[77] Koh Saitoh, Yuya Hasegawa, Nobuo Tanaka, and Masaya Uchida. Production of electron vortex beams carrying large orbital angular momentum using spiral zone plates. *Journal of Electron Microscopy*, 61(3):171–177, June 2012.

[78] J. Verbeeck, H. Tian, and A. Béché. A new way of producing electron vortex probes for STEM. *Ultramicroscopy*, 113(0):83–87, February 2012.

[79] Roger J. McNichols and Gerard L. Cote. Optical glucose sensing in biological fluids: an overview. *Journal of Biomedical Optics*, 5(1):5–16, 2000.

[80] G. D. Fasman. *Circular Dichroism and the Conformational Analysis of Biomolecules*. Springer US, April 1996.

[81] S. L. Prosvirnin and N. I. Zheludev. Polarization effects in the diffraction of light by a planar chiral structure. *Physical Review E*, 71(3):037603, March 2005.

[82] A. Papakostas, A. Potts, D. M. Bagnall, S. L. Prosvirnin, H. J. Coles, and N. I. Zheludev. Optical Manifestations of Planar Chirality. *Physical Review Letters*, 90(10):107404, March 2003.

[83] Makoto Kuwata-Gonokami, Nobuyoshi Saito, Yusuke Ino, Martti Kauranen, Konstantins Jefimovs, Tuomas Vallius, Jari Turunen, and Yuri Svirko. Giant Optical Activity in Quasi-Two-Dimensional Planar Nanostructures. *Physical Review Letters*, 95(22):227401, November 2005.

[84] Tomoki Ohno and Shintaro Miyanishi. Study of surface plasmon chirality induced by archimedes' spiral grooves. *Optics Express*, 14(13):6285–6290, June 2006.

[85] K. Konishi, T. Sugimoto, B. Bai, Y. Svirko, and M. Kuwata-Gonokami. Effect of surface plasmon resonance on the optical activity of chiral metal nanogratings. *Optics Express*, 15(15):9575–9583, July 2007.

[86] G. Schütz, W. Wagner, W. Wilhelm, P. Kienle, R. Zeller, R. Frahm, and G. Materlik. Absorption of circularly polarized x rays in iron. *Physical Review Letters*, 58(7):737–740, February 1987.

[87] Uwe J. Meierhenrich, Jean-Jacques Filippi, Cornelia Meinert, Jan Hendrik Bredehöft, Jun-ichi Takahashi, Laurent Nahon, Nykola C. Jones, and Søren V. Hoffmann. Circular Dichroism of Amino Acids in the Vacuum-Ultraviolet Region. *Angewandte Chemie International Edition*, 49(42):7799–7802, October 2010.

[88] W. Curtis Johnson. Protein secondary structure and circular dichroism: A practical guide. *Proteins: Structure, Function, and Bioinformatics*, 7(3):205–214, January 1990.

[89] B. A. Wallace, Kunihiko Gekko, Søren Vrønning Hoffmann, Yi-Hung Lin, John C. Sutherland, Ye Tao, Frank Wien, and Robert W. Janes. Synchrotron radiation circular dichroism (SRCD) spectroscopy: An emerging method in structural biology for examining protein conformations and protein interactions. *Nuclear Instruments and Methods in Physics Research Section A: Accelerators, Spectrometers, Detectors and Associated Equipment*, 649(1):177–178, September 2011.

[90] Ondrej L. Krivanek, Tracy C. Lovejoy, Niklas Dellby, Toshihiro Aoki, R. W. Carpenter, Peter Rez, Emmanuel Soignard, Jiangtao Zhu, Philip E. Batson, Maureen J. Lagos, Ray F. Egerton, and Peter A. Crozier. Vibrational spectroscopy in the electron microscope. *Nature*, 514(7521):209–212, October 2014.

[91] Z Hong Zhou. Towards atomic resolution structural determination by single-particle cryo-electron microscopy. *Current Opinion in Structural Biology*, 18(2):218–228, April 2008.

[92] R.F. Egerton. *Electron Energy-Loss Spectroscopy in the Electron Microscope*. Springer US, Boston, MA, 2011.

[93] Christoph Langhammer, Markus Schwind, Bengt Kasemo, and Igor Zorić. Localized Surface Plasmon Resonances in Aluminum Nanodisks. *Nano Letters*, 8(5):1461–1471, May 2008.

[94] T.r. Harvey, J.s. Pierce, T.s. Yahn, P.a. Ercius, and B.j. McMorran. Electron Orbital Angular Momentum Transfer to Nanoparticle Plasmon Modes. *Microscopy and Microanalysis*, 19(Supplement S2):1186–1187, 2013.

[95] Tyler R. Harvey, Jordan Chess, Jordan S. Pierce, Peter Ercius, and Benjamin J. McMorran. Characterization of Electron Orbital Angular Momentum Transfer to Nanoparticle Plasmon Modes. *Microscopy and Microanalysis*, 20(Supplement S3):68–69, August 2014.

[96] See Supplemental Material at (url) for details on post-selection procedure, electron helical dichroism measurement process and further observations of dichroism.

[97] Y. Gorodetski, A. Niv, V. Kleiner, and E. Hasman. Observation of the Spin-Based Plasmonic Effect in Nanoscale Structures. *Physical Review Letters*, 101(4):043903, July 2008.

[98] Ondrej L. Krivanek, Jan Rusz, Juan-Carlos Idrobo, Tracy J. Lovejoy, and Niklas Dellby. Toward Single Mode, Atomic Size Electron Vortex Beams. *Microscopy and Microanalysis*, FirstView:1–5, 2014.

[99] Xiao-chen Bai, Israel S. Fernandez, Greg McMullan, and Sjors HW Scheres. Ribosome structures to near-atomic resolution from thirty thousand cryo-EM particles. *eLife*, 2:e00461, February 2013.

[100] Konstantin Bliokh, Yury Bliokh, Sergey Savel'ev, and Franco Nori. Semiclassical Dynamics of Electron Wave Packet States with Phase Vortices. *Physical Review Letters*, 99(19):190404, November 2007.

[101] S. J. Pennycook and D. E. Jesson. High-resolution incoherent imaging of crystals. *Physical Review Letters*, 64(8):938–941, February 1990.

[102] Hao Yang, Peter Ercius, Peter D. Nellist, and Colin Ophus. Enhanced phase contrast transfer using ptychography combined with a pre-specimen phase plate in a scanning transmission electron microscope. *Ultramicroscopy*, 171:117–125, December 2016.

[103] H. Yang, R. N. Rutte, L. Jones, M. Simson, R. Sagawa, H. Ryll, M. Huth, T. J. Pennycook, M. L. H. Green, H. Soltau, Y. Kondo, B. G. Davis, and P. D. Nellist. Simultaneous atomic-resolution electron ptychography and Z-contrast imaging of light and heavy elements in complex nanostructures. *Nature Communications*, 7:12532, August 2016.

[104] Colin Ophus, Jim Ciston, Jordan Pierce, Tyler R. Harvey, Jordan Chess, Benjamin J. McMorran, Cory Czarnik, Harald H. Rose, and Peter Ercius. Efficient linear phase contrast in scanning transmission electron microscopy with matched illumination and detector interferometry. *Nature Communications*, 7:10719, February 2016.

[105] Roeland Juchtmans, Laura Clark, Axel Lubk, and Jo Verbeeck. Spiral phase plate contrast in optical and electron microscopy. *Physical Review A*, 94(2):023838, August 2016.

[106] David Shook and Benjamin J. McMorran. Propagation of Free Electrons Carrying Orbital Angular Momentum Through Magnetic Lenses. *Microscopy and Microanalysis*, 20(S3):292–293, August 2014.

[107] Gregorius C. G. Berkhout, Martin P. J. Lavery, Johannes Courtial, Marco W. Beijersbergen, and Miles J. Padgett. Efficient Sorting of Orbital Angular Momentum States of Light. *Physical Review Letters*, 105(15):153601, October 2010.

[108] P. Schattschneider, M. Stöger-Pollach, and J. Verbeeck. Novel Vortex Generator and Mode Converter for Electron Beams. *Physical Review Letters*, 109(8):084801, August 2012.

[109] A. Béché, R. Juchtmans, and J. Verbeeck. Efficient creation of electron vortex beams for high resolution STEM imaging. *Ultramicroscopy*, 2016.

[110] Ján Rusz, Juan-Carlos Idrobo, and Somnath Bhowmick. Achieving Atomic Resolution Magnetic Dichroism by Controlling the Phase Symmetry of an Electron Probe. *Physical Review Letters*, 113(14):145501, September 2014.

[111] J. H. Macek, J. B. Sternberg, S. Y. Ovchinnikov, and J. S. Briggs. Theory of Deep Minima in $(e,2e)$ Measurements of Triply Differential Cross Sections. *Physical Review Letters*, 104(3):033201, January 2010.

[112] J. M. Ngoko Djiokap, S. X. Hu, L. B. Madsen, N. L. Manakov, A. V. Meremianin, and Anthony F. Starace. Electron Vortices in Photoionization by Circularly Polarized Attosecond Pulses. *Physical Review Letters*, 115(11):113004, September 2015.

[113] R. Géneaux, A. Camper, T. Auguste, O. Gobert, J. Caillat, R. Taïeb, and T. Ruchon. Synthesis and characterization of attosecond light vortices in the extreme ultraviolet. *Nature Communications*, 7:12583, August 2016.

[114] V. Serbo, I. P. Ivanov, S. Fritzsche, D. Seipt, and A. Surzhykov. Scattering of twisted relativistic electrons by atoms. *Physical Review A*, 92(1):012705, July 2015.

[115] Ryuji Takahashi and Naoto Nagaosa. Berry curvature and orbital angular momentum of electrons in angle-resolved photoemission spectroscopy. *Physical Review B*, 91(24):245133, June 2015.

[116] Ebrahim Karimi, Lorenzo Marrucci, Vincenzo Grillo, and Enrico Santamato. Spin-to-Orbital Angular Momentum Conversion and Spin-Polarization Filtering in Electron Beams. *Physical Review Letters*, 108(4):044801, January 2012.

[117] J. Yuan, S. M. Lloyd, and M. Babiker. Chiral-specific electron-vortex-beam spectroscopy. *Physical Review A*, 88(3):031801, September 2013.

[118] Walther Gerlach and Otto Stern. Der experimentelle Nachweis der Richtungsquantelung im Magnetfeld. *Zeitschrift für Physik*, 9(1):349–352, December 1922.

[119] Emmy Noether. Invariant variation problems. *Transport Theory and Statistical Physics*, 1(3):186–207, January 1971.

[120] H. Batelaan, T. J. Gay, and J. J. Schwendiman. Stern-Gerlach Effect for Electron Beams. *Physical Review Letters*, 79(23):4517–4521, December 1997.

[121] Harald Rose. *Geometrical Charged-Particle Optics*. Springer, February 2013.

[122] Ludwig Reimer and Helmut Kohl. *Transmission Electron Microscopy: Physics If Image Formation*. Springer, 2008.

[123] John Von Neumann. *Mathematical Foundations of Quantum Mechanics*. Princeton University Press, 1955.

[124] Vincenzo Grillo, Lorenzo Marrucci, Ebrahim Karimi, Riccardo Zanella, and Enrico Santamato. Quantum simulation of a spin polarization device in an electron microscope. *New Journal of Physics*, 15(9):093026, 2013.

[125] P. Schattschneider, V. Grillo, and D. Aubry. Spin polarisation with electron Bessel beams. *Ultramicroscopy*, 174:8–13, March 2017.

[126] Giulio Pozzi. A multislice approach to magnetic electron lens theory. *Ultramicroscopy*, 30(3):417–424, July 1989.

[127] H. Alfven. *Cosmical Electrodynamics*. Oxford, Clarendon Press, 1963.

[128] Daniel Malacara-Hernández and Zacarías Malacara-Hernández. *Handbook of Optical Design, Second Edition*. CRC Press, October 2014.

[129] F. Z. Marai and T. Mulvey. Scherzer's formula and the correction of spiral distortion in the electron microscope. *Ultramicroscopy*, 2:187–192, January 1976.

[130] Earl J. Kirkland. On the optimum probe in aberration corrected ADF-STEM. *Ultramicroscopy*, 111(11):1523–1530, November 2011.

[131] Juan C. Idrobo and Stephen J. Pennycook. Vortex beams for atomic resolution dichroism. *Journal of Electron Microscopy*, 60(5):295 –300, October 2011.

[132] Martin P. J. Lavery, David J. Robertson, Gregorius C. G. Berkhout, Gordon D. Love, Miles J. Padgett, and Johannes Courtial. Refractive elements for the measurement of the orbital angular momentum of a single photon. *Optics Express*, 20(3):2110, January 2012.

[133] Mehul Malik, Mohammad Mirhosseini, Martin P. J. Lavery, Jonathan Leach, Miles J. Padgett, and Robert W. Boyd. Direct measurement of a 27-dimensional orbital-angular-momentum state vector. *Nature Communications*, 5:3115, January 2014.

[134] Mohammad Mirhosseini, Omar S. Magaña-Loaiza, Malcolm N. O'Sullivan, Brandon Rodenburg, Mehul Malik, Martin P. J. Lavery, Miles J. Padgett, Daniel J. Gauthier, and Robert W. Boyd. High-dimensional quantum cryptography with twisted light. *New Journal of Physics*, 17(3):033033, 2015.

[135] Yan Yan, Guodong Xie, Martin P. J. Lavery, Hao Huang, Nisar Ahmed, Changjing Bao, Yongxiong Ren, Yinwen Cao, Long Li, Zhe Zhao, Andreas F. Molisch, Moshe Tur, Miles J. Padgett, and Alan E. Willner. High-capacity millimetre-wave communications with orbital angular momentum multiplexing. *Nature Communications*, 5:4876, September 2014.

[136] Hao Huang, Giovanni Milione, Martin P. J. Lavery, Guodong Xie, Yongxiong Ren, Yinwen Cao, Nisar Ahmed, Thien An Nguyen, Daniel A. Nolan, Ming-Jun Li, Moshe Tur, Robert R. Alfano, and Alan E. Willner. Mode division multiplexing using an orbital angular momentum mode sorter and MIMO-DSP over a graded-index few-mode optical fibre. *Scientific Reports*, 5:14931, October 2015.

[137] W. J. Hossack, A. M. Darling, and A. Dahdouh. Coordinate Transformations with Multiple Computer-generated Optical Elements. *Journal of Modern Optics*, 34(9):1235–1250, September 1987.

[138] G. Matteucci, G. F. Missiroli, M. Muccini, and G. Pozzi. Electron holography in the study of the electrostatic fields: the case of charged microtips. *Ultramicroscopy*, 45(1):77–83, August 1992.

[139] John Cumings, A. Zettl, M. R. McCartney, and J. C. H. Spence. Electron Holography of Field-Emitting Carbon Nanotubes. *Physical Review Letters*, 88(5):056804, January 2002.

[140] M. Beleggia, T. Kasama, D. J. Larson, T. F. Kelly, R. E. Dunin-Borkowski, and G. Pozzi. Towards quantitative off-axis electron holographic mapping of the electric field around the tip of a sharp biased metallic needle. *Journal of Applied Physics*, 116(2):024305, July 2014.

[141] Martha R. McCartney and David J. Smith. Electron Holography: Phase Imaging with Nanometer Resolution. *Annual Review of Materials Research*, 37(1):729–767, 2007.

[142] Richard Phillips Feynman. Chapter 7: The Electric Field in Various Circumstances (Continued). In *The Feynman Lectures on Physics*, volume 2. Addison-Wesley, Reading, MA, June 1964.

[143] Giulio Pozzi, Marco Beleggia, Takeshi Kasama, and Rafal E. Dunin-Borkowski. Interferometric methods for mapping static electric and magnetic fields. *Comptes Rendus Physique*, 15(2–3):126–139, February 2014.

[144] M. Beleggia, T. Kasama, R. E. Dunin-Borkowski, S. Hofmann, and G. Pozzi. Direct measurement of the charge distribution along a biased carbon nanotube bundle using electron holography. *Applied Physics Letters*, 98(24):243101, June 2011.

[145] Lorenzo Pardini, Stefan Löffler, Giulio Biddau, Ralf Hambach, Ute Kaiser, Claudia Draxl, and Peter Schattschneider. Mapping Atomic Orbitals with the Transmission Electron Microscope: Images of Defective Graphene Predicted from First-Principles Theory. *Physical Review Letters*, 117(3):036801, 2016.

[146] Giulio Guzzinati, Armand Béché, Hugo Lourenço-Martins, Jérôme Martin, Mathieu Kociak, and Jo Verbeeck. Probing the symmetry of the potential of localized surface plasmon resonances with phase-shaped electron beams. *Nature Communications*, 8:14999, April 2017.